University of Milano - Bicocca

Department of Materials Science

Living radical polymerization for the preparation of innovative macromolecular architectures

Alberto Bianchi

Ph.D. School in Material Science - XXV cycle

Thesis presented for the degree of Doctor Europaeus

Supervisor: Dr. Roberto Simonutti

Tutor: Dr. Raffaella Donetti

Dean of the Doctorate: Prof. Gian Paolo Brivio

January 2013

Dedicated to the memory
of my father, Michele

Contents

Abstract

In this thesis I have dealt with the synthesis of different macromolecular structures in order to create innovative devices. The heart of the process of synthesis has been the RAFT polymerization, a recent polymerization technique which allows the compatibilization of various chemical systems.

The aim of this work is the improvement of innovative devices already on the market with good performance, but that possess limitations both as what regards specific technical properties and commercial exploitation. The aspect which has to be improved isn't related to the device's functional materials, rather to the compatibilization between them. Often, materials with remarkable absolute performances are used in a device, but these state-of-the-art components suffer from a partial quenching of their properties when incorporated in the final device. For this reason, in recent years, many studies have focused on materials that compatibilize different chemicals structures. For example polymeric composite materials combine the various functional properties of inorganic materials (metals and metal oxides) with mechanical properties of structural polymers. The different chemical nature of these two classes of materials leads to incompatibility, un-mixing and then to the worsening of the final performance in the operating conditions of the device. So it is essential to find materials that allow the different structures to chemically recognize each other through their surfaces.

The materials used in this context are the surfactants, namely compounds that possess both polar and non-polar moieties. The same mechanism is at the base of the natural world in which, for example, liposomes form cell membranes which are fundamental for life itself.

With this in mind, I focused to the synthesis of amphiphilic materials that possess hydrophilic and hydrophobic parts, therefore affinity with inorganic materials, or water based, and organic materials. This type of structure can be found in macromolecular materials. Access to such complex polymer structures - and concomitantly access to carefully tunable polymer properties - has been greatly enhanced with the advent of living free radical polymerization (LFRP) protocols that allow for the synthesis of multifunctional "chain transfer" agents that can serve as molecular machinery for obtaining polymers with complex architecture. The most prominent among LFRP techniques are Reversible Addition–Fragmentation chain Transfer (RAFT),[1] Atom Transfer Radical Polymerization (ATRP)[2,3] and Nitroxide-Mediated Polymerization (NMP).[4,5] In particular, the strength of RAFT chemistry lies in its high tolerance to functional monomers and the non-demanding reaction conditions (e.g. tolerance to oxygen and low temperatures) under which the polymerizations can be carried out. In addition, a wide range of monomers with varying reactivity can be used. RAFT polymerization offers substantial versatility when it comes to the synthesis of block copolymers, star polymers, polymer brushes, and other complex polymer systems.[6] The critical key to their synthesis is the presence of chain transfer agent (RAFT agent or CTA) with a thiocarbonylthio end group.

Undesired bimolecular termination reactions, high initiator concentrations, or chain transfer to monomer or solvent can reduce the amount of RAFT end capped polymer chains. If carefully designed, RAFT polymerization opens the door to a range of polymer architectures by variable approaches.

Similar to other living radical polymerization techniques, block copolymers, star and comb polymers, as well as graft polymers are accessible by attaching the controlling moiety to a (multi)functional core linking moiety. In addition, block structures are obtained by chain extension of the RAFT moiety capped block. Unique to the RAFT process are the possible modes of attaching the RAFT group covalently to the (multi)functional moiety.

The first aspect analyzed was the self-assembly of amphiphilic block copolymers into complex architectures. As known block copolymers in the solid state have a separation of phases in the order of nanometers[7]. In addition, by varying the chemical composition of the blocks and their relationship, it is possible to generate a variety of morphologies (spherical, cylindrical, lamellar or gyroidal). This behavior is described by the diagram of Matsen and Schick (see Figure 1) and relates to polymers in their thermodynamic minimum. The introduction of a solvent in the system can be interpreted as a third dimension in the diagram. Thus, in addition to the variation of χN (Flory-Huggins interaction parameter times total number of monomer units) and f_x (fraction of the monomeric units x), we can introduce the quantity of solvent. The interaction between the solvent and the chemistry of the block copolymer is a key parameter to determine in what way the self assembly occurs. In the case of complete solubility the polymer will be completely dissolved while selective (or partial) solubility occurs if a single block is dissolved. The latter leads to the formation of particular structures that depend on all previous parameters in addition to temperature and the environmental conditions. Therefore, amphiphilic block copolymers can self-assemble into structures such as micelles, spheres, worm-like assemblies, toroids and polymer gels, depending on the ratio of the selective solvent.

With RAFT technique, I have synthesized diblock copolymers constituted by polystyrene and polydimethylacrylamide with different total block length and studied their self-assembly in different solvents and concentrations, with the aim of introducing functional molecules in incompatible matrices (Chapter 4). Also, I produced the triblock copolymer polystyrene-polyethylene oxide and used as a polymer gel for electrolyte in dye-sensitized solar cells (Chapter 5). The advantage of this technique is that the polymer is free from the contamination of metal catalyst.

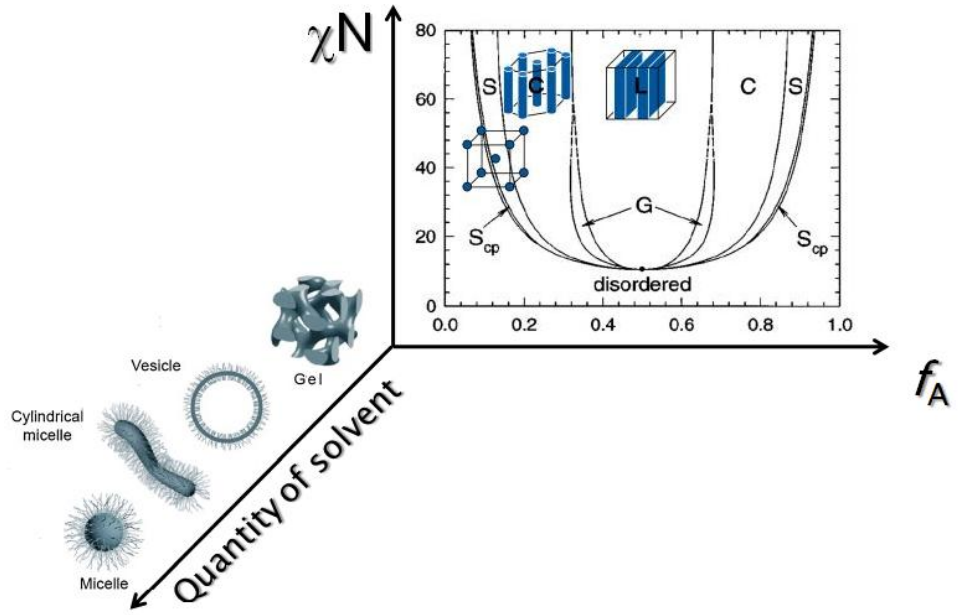

Figure 1. Schematic representation of the phase diagram of the 3D self assembly of block copolymers AB in the presence of a selective solvent. Between the axles χN (interaction parameter of Flory-Huggins per total number of monomer units) and fx (fraction of the monomeric units x to N) is represented the phase diagram of Matsen and Schick.

The second topic has been the functionalization of nanoparticles of metal oxides with different polymers. The surface chemistry has been modified by making it more similar to the host matrix, in this way a polymer nanocomposite is created with high performance limiting the de-mixing of the different components.

Polymer grafting techniques provide a very versatile tool to tailor the surface of nanoparticles and thus the interfaces between nanoparticles and the matrix polymers. The RAFT technique provides control over the type of polymer to be grafted onto the particle surface, surface densities, and chain lengths at the nanometer scale.[8] The technique of covalently grafting polymer chains onto particles can be categorized into "grafting from" and "grafting to". The grafting to technique involves reacting the polymer, bearing an appropriate functional

group, with the particles to chemically attach the polymer chains.[9] Because of the steric hindrance imposed by the already grafted chains, it becomes increasingly difficult for the incoming polymer chains to diffuse to the surface against the concentration gradient of the existing grafted polymers, which intrinsically results in low graft densities. In contrast, the grafting from technique uses initiators that have been initially anchored to the particle surface, followed by the polymerization from the surface. Since the existing grafted polymers will not hinder the diffusion of the small-sized monomers, significantly higher graft densities can be achieved with this technique. In this study, I was involved in the growth of the polymer to the surface (grafting from) to ensure a high coating density.

I have synthesized a polymer shell of polystyrene on nanoparticles of titania to create a nanocomposite TiO_2/PS (Chapter 6), which has been tested as a material with high dielectric properties. I also polymerized isoprene on commercial SiO_2 in order to introduce it in the production of compounds for tyres and thereby increase the dispersion and improve the dispersion of filler in the rubber matrix (Chapter 7).

Chapter 1. RAFT polymerization

In this chapter I will describe the Radical Addition-Frammentation chain Trasfer (RAFT) polymarization, in particular the birth and evolution of the technique until to our days, the mechanism that governs the polymerization and its potentialities. Finally, I will spend a large part on RAFT agents and their roles.

1.1. Description

RAFT polymerization processes are a recent discovery and arise from the need to combine the advantages of the radical polymerizations with those of anionic living polymerizations, minimizing the problems related to them[10].

The radical polymerizations, although having the advantage of being very simple to perform, are not suitable for processes for which it is necessary to have a high selectivity and uniformity of the products obtained, as they are poorly controllable and provide polymers of with broad molecular weight distributions. In addition, as mentioned, the anionic polymerizations have the disadvantage of being able to be used only with a limited number of monomers and require expensive catalysts and harsh reaction conditions.

This type of synthesis is distinguished by its versatility: in fact, it can be used with a wide range of monomers and in different reaction conditions, providing polymers with a good control of average molecular weight and molecular weight distribution. In addition, polymerizations can be carried out in solution, emulsion and bulk by using the common peroxide or nitrogen initiators. Typically, a RAFT polymerization system consists of a radical source (e.g.

thermochemical initiator or the interaction of gamma radiation with some reagent), monomer, RAFT agent and a solvent (not strictly required if the monomer is a liquid). A temperature is chosen such that chain growth occurs at an appropriate rate, the chemical initiator (radical source) delivers radicals at an appropriate rate and the central RAFT equilibrium (see paragraph 1.3) favors the active rather than dormant state to an acceptable extent.

1.2. History of RAFT polymerization

The first reports of radical addition-fragmentation processes appeared in the synthetic organic chemistry literature in the early 1970s[11]. Now well-known examples of processes that involve a reaction step with an S_H2 mechanism include allyl transfer reactions with allyl sulfides[12] and Stannanes (the Keck reaction) and the Bartone McCombie deoxygenation process with xanthates[13]. A survey of these reactions is included in the review by Colombani and Chaumont. The first reports of the direct use of addition-fragmentation transfer agents to control radical polymerization appeared in the 1980s[14,15]. Polymerizations with reversible addition–fragmentation chain transfer which showed some of the characteristics of living polymerization were first reported in 1995.

The term RAFT polymerization was coined in 1998 when the use of thiocarbonylthio RAFT agents was first reported in the open literature[16]. This article is the real founder of the technique, and has been cited 1405 times, so far.

RAFT polymerization is also reviewed within works which deal more generically with radical polymerization. The literature through 2005 is comprehensively reviewed within the chapter "Living radical polymerization in the chemistry of radical polymerization"[17] and is given substantial coverage in many recent works that relate more generically to polymer synthesis, living polymerization or novel architectures. Other relevant reviews include those focusing on the synthesis and organic chemistry of dithioesters and other

thiocarbonylthio compounds in a non-polymerization context[18] and the use of RAFT in organic synthesis[19]. The literature is expanding very rapidly; an update review[20] covering the period mid 2005 to mid 2006 revealed more than 200 papers dealing directly with the use and application of RAFT polymerization. First communication on RAFT with trithiocarbonyl compounds[16] now has more than1000 citations and is one of the most highly cited papers in Macromolecules and the first RAFT patent[21] was seventh on the list of most cited patents in the field of chemistry and related science in 2005.

In contrast to the quick increase of the publications, the commercial market has had a slow start: the first transfer agent has been commercialized in 2004, was produced for 2-3 years only and has been the only one for sale. Around the 2008/2009 the number of agents increased and now about seventeen are available on the market. Now, a range of RAFT agents including the carboxylic acid functional RAFT agents are commercially available as fine chemical for research purposes. The industrial scale-up has been announced of the xanthate Rhodixan-A1 (by Rhodia) and trithiocarbonates Blocbuilder DB and CTA-1 (by Arkema and Lubrizol, respectively).

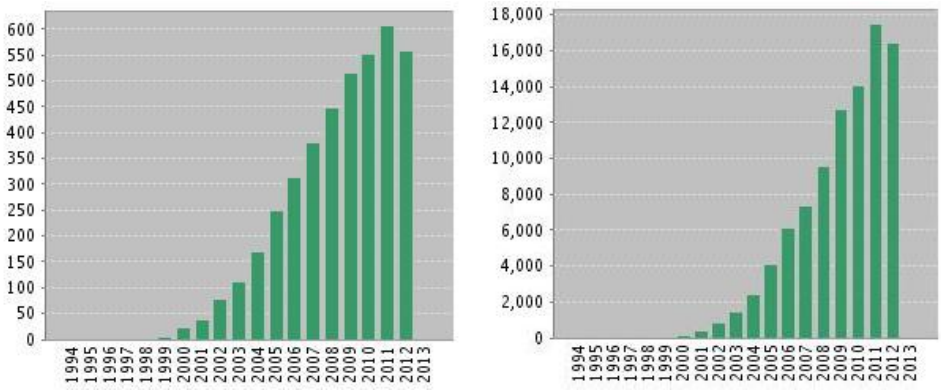

Figure 2. On the left: Published Items in Each Year, on the right: Citations in Each Year[22] (December 2012).

The popularity of the RAFT process has steadily increased since the first report in 1998 (2245 times cited). Figure 2 gives the number of RAFT-related papers as function of the year (up to November 2012). It is clear that the research interest in the RAFT process continues to be very strong.

1.3. Mechanisms of the RAFT polymerization

In literature there are many papers and reviews concerning the mechanism of polymerization RAFT, which not always have a comprehensive explanation of the phenomenon. This section describes the process starting from simple Addition-Fragmentation in order to explain the reversible and termination phenomena.

Addition-Fragmentation transfer agents and mechanisms through which these reagents provide addition-fragmentation chain transfer during polymerization are shown in Figure 3. Unsaturated compounds of general structure 1 or 4 can act as transfer agents by a two-step addition-fragmentation mechanism. In these compounds C=X should be a double bond that is reactive towards radical addition. X is most often CH_2 or S. Z is a group chosen to give the transfer agent an appropriate reactivity towards propagating radicals and convey appropriate stability to the intermediate radicals (2 or 5, respectively). Examples of A are CH_2, CH_2=$CHCH_2$, O or S. R is a homolytic leaving group and R• should be capable of efficiently reinitiating polymerization. In all known examples of transfer agents 4, B is O. Since functionality can be introduced to the products 3 or 6 in either or both the transfer agents (typically from Z) and reinitiation (from R) steps, these reagents offer a route to a variety of end-functional polymers including telechelics.

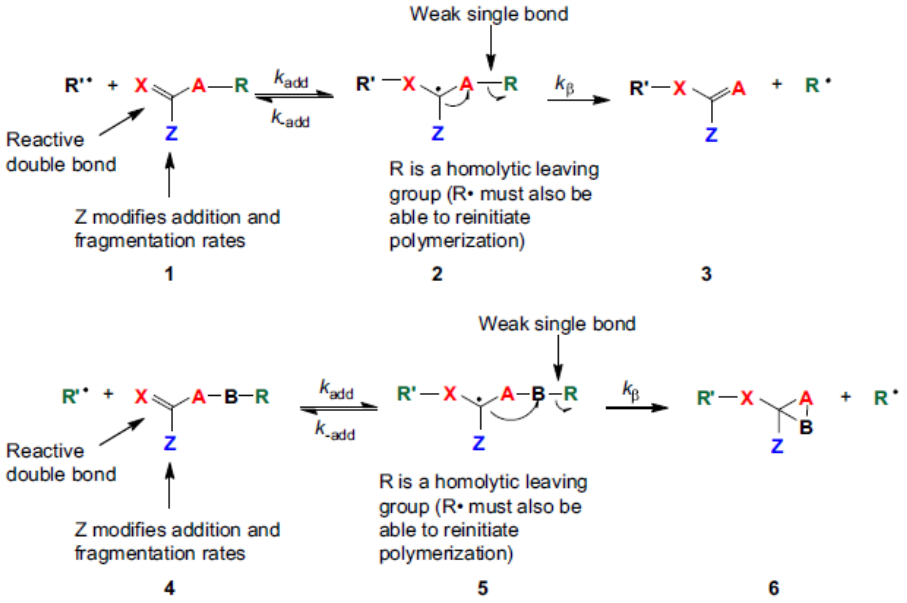

Figure 3. Scheme of mechanisms for addition-fragmentation chain transfer

Rates of addition to transfer agents 1 and 4 with X=CH_2 are determined by the same factors that determine rates of addition to monomer. Thus, substituents at A (i.e. R, B-R) have only a minor influence on reactivity, consequently the double bonds of the transfer agents 1 and 4 with X=CH_2 have a reactivity towards radical addition that is similar to that of the common monomers they resemble. Thus, with efficient fragmentation, transfer constants (C_{tr}) can be close to unity. A C_{tr} of unity has been called 'ideal' since the transfer agent and monomer are consumed at the same rate and, as a consequence, the molecular weight should remain essentially constant with monomer conversion. In addition-fragmentation chain transfer, the rate constant for chain transfer (k_{tr}) is defined in terms of the rate constant for addition (k_{add}) and a partition coefficient (ϕ) which defines how the adduct is partitioned between products and starting materials (Eqs. (1) and (2)). Thus, referring to figure 1 for notations:

$$k_{tr} = k_{add}\frac{k_{tr}}{k_{-add}+k_{\beta}} = k_{add}\phi \quad (1)$$

$$\phi = \frac{k_{\beta}}{k_{-add}-k_{\beta}} \quad (2)$$

The transfer constant is defined in terms of k_{tr} and the propagation rate constant (k_p) in the usual way ($C_{tr} = k_{tr}/k_p$). Efficient transfer requires that the radical intermediates formed by addition undergo facile β-scission (for 1) or rearrangement (for 4) to form a new radical that can reinitiate polymerization. The radical intermediates 2 and 5 typically have low reactivity towards further propagation and other intermolecular reactions because of steric crowding about the radical center. The driving force for fragmentation of the intermediate radical is provided by cleavage of a weak A-R or B-R bond and or formation of a strong C=A bond (for 1). If both addition and fragmentation are rapid and irreversible with respect to propagation the polymerization kinetics differ little from those seen in polymerization with conventional chain transfer. If the overall rate of β-scission is slow relative to propagation then retardation is a likely result. If fragmentation is slow, the adducts (2 or 5) also have a greater potential to undergo side reactions by addition to monomer (copolymerization of the transfer agent) or radical-radical termination. Retardation is often an issue with high k_p monomers such as VAc and MA. In designing transfer agents and choosing an R group, a balance must also be achieved between the leaving group ability of R and reinitiation efficiency of R• since, as with conventional chain transfer, the rate constant for reinitiation by R• should be $\geq k_p$. The methods used for evaluating transfer constants are the same as for conventional chain transfer and involve evaluating the molecular weight in low conversion polymerizations or relative rate of consumption of transfer agent and monomer.

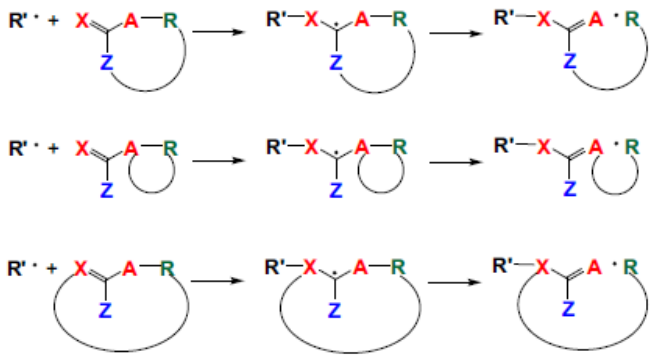

Figure 4. Potential propagation mechanisms in ring-opening polymerization.

When the product of the reaction is itself a potential transfer agent or a macromonomer, further reaction to form a block, graft or hyperbranched copolymer formation may occur particularly at high conversions[23]. The reverse pathway can also be blocked by choice of A. For example, when A is oxygen or bears a substituent (e.g., A =CH-CH_3), the product is rendered essentially unreactive to radical addition. If R and Z, R and A or, in principle, R and X in structure 1 are connected to form a ring structure the result is a potential ring-opening monomer as shown in figure 2. For many of the transfer agents described, there are analogous ring-opening monomers.

Reversible chain transfer may, in principle, involve homolytic substitution (Figure 4) or addition-fragmentation (RAFT) or some other transfer mechanism. An essential feature is that the product of chain transfer is also a chain transfer agent with similar activity to the precursor transfer agent. The overall process has also been termed degenerate or degenerative chain transfer since the polymeric starting materials and products have equivalent properties and differ only in molecular weight (Figure 5 and Figure 6, where R• and R'• are both propagating chains).

Polymerization of styrene and certain fluoro-monomers in the presence of alkyl iodides provided the first example of the reversible homolytic substitution

process. This process is also known as iodine transfer polymerization[24]. Other more recent examples of control by reversible homolytic substitution chain transfer are polymerizations conducted in the presence of derivatives of organotellurides (TERP) or organostibines[25] and tin, germanium or phosphorus iodides (RCTPs).

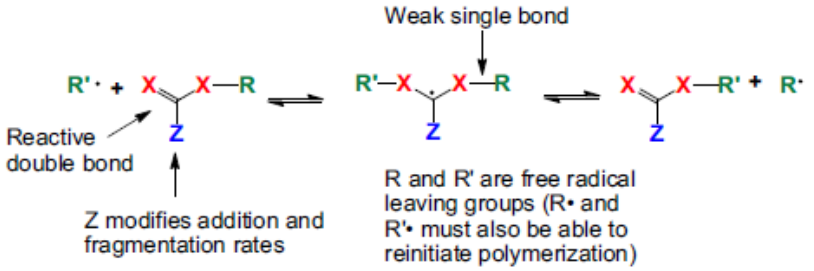

Figure 5. Reversible additionefragmentation chain transfer.

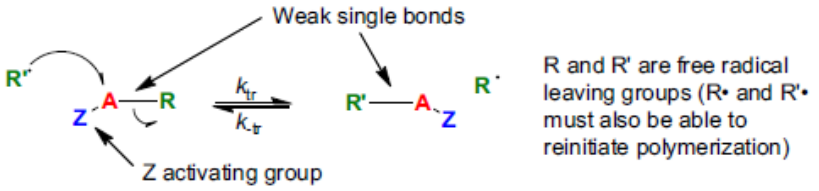

Figure 6. Reversible homolytic substitution chain transfer.

In 1995 it was reported that polymerizations of methacrylic monomers in the presence of methacrylic macromonomers (X = CH_2, Z = CO_2R) under monomer-starved conditions display many of the characteristics of living polymerization[26]. These systems involve the RAFT mechanism (Figure 7).

In 1982, Otsu et al.[27] proposed that living characteristics observed for polymerization in the presence of dithiocarbamate photoiniferters might be attributable to both reversible chain transfer and reversible radical-radical coupling steps as part of the mechanism. However, it is now known that degenerate chain transfer is a minor pathway for the reagents and reaction conditions used in those pioneering experiments. RAFT with thiocarbonylthio

compounds (X = S) was first reported in 1998 and is the most versatile and well known process of this class. It is compatible with most monomer types and with a very wide range of reaction conditions.

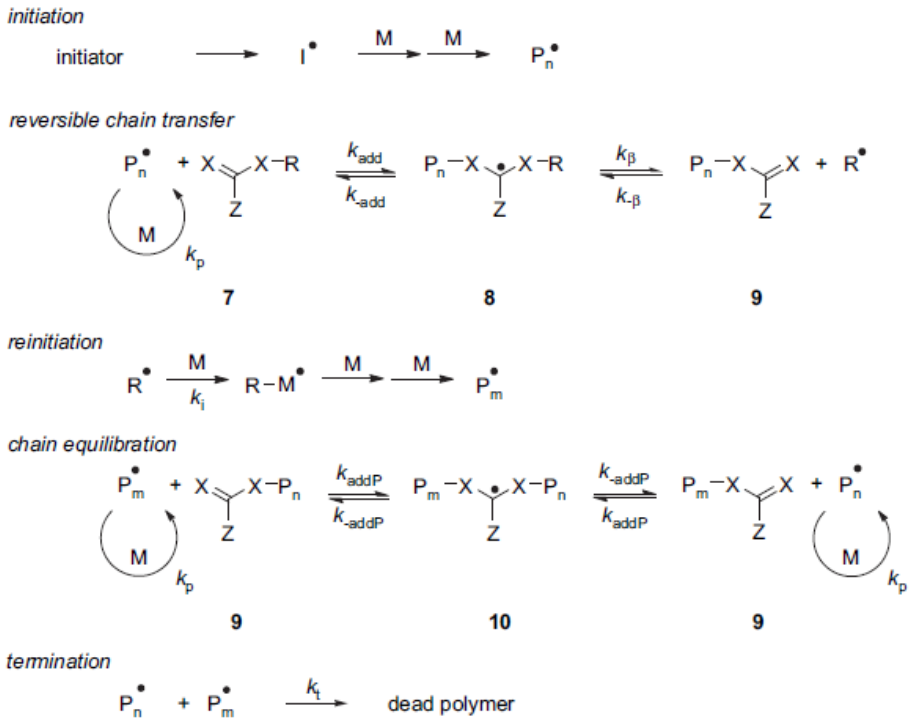

Figure 7. Mechanism of RAFT polymerization.

Recent reviews which relate specifically to RAFT polymerization with thiocarbonylthio compounds include general reviews by Moad, Rizzardo and Thang[28], Mayadunne and Rizzardo, Chiefari and Rizzardo, Perrier and Takolpuckde[29], Favier and Charreyre[30] and Barner-Kowollik, Davis, Stenzel and coworkers[31]. Many other reviews deal with specific applications of RAFT polymerization such as computational studies related to RAFT agents and RAFT polymerization, the kinetics and mechanism of RAFT polymerization, the control of molecular weight distributions produced by RAFT polymerization[32], RAFT

polymerization in aqueous media[33], the use of RAFT polymerization in heterogeneous media, the synthesis of end-functional polymers by RAFT polymerization[34], star polymer synthesis[35], the synthesis and properties of stimuli responsive block and other polymers and the preparation of honeycomb structures[36].

The key feature of the mechanism of RAFT polymerization with thiocarbonylthio compounds is the sequence of addition-fragmentation equilibrium shown in Figure 7[37]. Initiation and radical-radical termination occur as in conventional radical polymerization. In the early stages of the polymerization, addition of a propagating radical ($P^{\bullet}_{n}$) to the thiocarbonylthio compound [RSC(Z)=S (7)] followed by fragmentation of the intermediate radical provides a polymeric thiocarbonylthio compound [PnSC(Z)=S (9)] and a new radical (R•). Reaction of this radical (R•) with monomer forms a new propagating radical ($P^{\bullet}_{m}$). Rapid equilibrium between the active propagating radicals ($P^{\bullet}_{n}$ and $P^{\bullet}_{m}$) and the dormant polymeric thiocarbonylthio compounds (9) provides equal probability for all chains to grow and allows for the production of narrow polydispersity polymers. When the polymerization is complete (or stopped), the vast majority of chains retains the thiocarbonylthio end group and can be isolated as stable materials.

The reactions associated with RAFT equilibria shown in Figure 7 are in addition to those (i.e. initiation, propagation and termination) that occur during conventional radical polymerization. In an ideal RAFT process, the RAFT agent should behave as an ideal transfer agent. Thus, as with radical polymerization with conventional chain transfer, the kinetics of polymerization should not be directly affected beyond those effects attributable to the differing molecular weights of the reacting species. Radical-radical termination is not directly suppressed by the RAFT process. Living characteristics are imparted only when the molecular weight of the polymer formed is substantially lower than that which might be formed in the absence of a RAFT agent and the number of

polymer molecules with RAFT agent-derived ends far exceeds the number formed as a consequence of termination. For less active RAFT agents ($C_{tr} \leq 1$), transfer constants may be determined using the usual methods with little loss of accuracy. For more active transfer agents, where the transfer agent-derived radical ($R^{\bullet}$) may partition between adding to monomer and reacting with the polymeric RAFT agent (P_n^T) even at low conversions, the transfer constant measured according to the Mayo or related methods will appear to be dependent on the transfer agent concentration (and on the monomer conversion)[38]. This value should be called an apparent transfer constant C_{tr}^{app} and be regarded as a minimum value of the transfer constant. The actual transfer constant may be higher by several orders of magnitude[39]. The reverse transfer constant (C_{-tr}) is defined as follows (Eq. (3)):

$$C_{-tr} = \frac{k_{-tr}}{k_{iT}} \tag{3}$$

where k_{iT} is the rate of reinitiation by the RAFT agent-derived radical, $R^{\bullet}$, and the rate of transfer agent consumption is then given by Eq. (4):

$$\frac{d[T]}{d[M]} \approx C_{tr} \frac{[T]}{[M]+C_{tr}[T]+C_{-tr}[P_n^T]} = C_{tr} \frac{[T]}{[M]+C_{tr}[T]+C_{-tr}([T_0]-[T])} \tag{4}$$

This equation can be solved numerically to give estimates of C_{tr} and C_{-tr}. The rate constant for the reverse transfer is defined analogously to that for the forward reaction (Eq. (1)) as shown in Eq. (5):

$$k_{-tr} = k_{-\beta} \frac{k_{-add}}{k_{-add}+k_{\beta}} \tag{5}$$

If the reverse reaction can be neglected Eq. (4) simplifies as follows:

$$\frac{d[T]}{d[M]} \approx C_{tr}\frac{[T]}{[M]} + 1 \qquad (6)$$

which suggests that a plot of log(M) vs log(T) should be a straight line with the slope proving the transfer constant. This equation has been used to evaluate C_{tr} for a range of RAFT agents. For the more active RAFT agents, the values so obtained should be regarded as apparent transfer constants (C_{tr}^{app}) and as a minimum value for C_{tr}. Systems that give reversible chain transfer can display the characteristics of living polymerization. Narrowed polydispersities will generally only be observed when $C_{tr} > 2$ and $C_{tr} > 10$ are required to achieve the characteristics often associated with living polymerization (i.e. significantly narrowed molecular weight distributions, molecular weights predictable from reagent concentrations that increase linearly with conversion).

The more effective RAFT agents have $C_{tr} \gg 100$. The dependence of molecular weight and polydispersity on monomer conversion for various values of C_{tr} for a hypothetical polymerization without termination is shown in Figure 8. Various factors will cause deviations from this ideal behavior. The properties of RAFT agents are often discussed in terms of the value of the equilibrium constants associated with radical addition to the thiocarbonylthio compound. Rates of addition are typically high (k_{add}, $k_{-\beta}$, k_{addP} $\sim 10^6$-10^8 M^{-1} s^{-1}).

Thus a high equilibrium constant generally implies a low fragmentation rate constant (k_{-add}, k_{β}, k_{-addP}) and consequently an increased likelihood for retardation and/or side reaction involving the adduct species. However, values of the equilibrium constants do not, by themselves, provide sufficient information to predict the ability of a RAFT agent to control polymerization.

In a given RAFT polymerization, there are at least four equilibrium constants that need to be considered. $K_P (=k_{addP}/k_{-addP})$ is associated with the chain equilibration process (Figure 7). This step is sometimes called the main

equilibrium. $K(=k_{add}/k_{-add})$ and $K_\beta(=k_{-\beta}/k_\beta)$ are associated with the initial reversible chain transfer step sometimes known as the pre-equilibrium. $K_R(=k_{addR}/k_{-addR})$is associated with the reaction of the expelled radical with the initial RAFT agent (Figure 5, where X=S). This process only becomes significant if the intermediate formed has a significant lifetime. There may be other equilibrium constants to consider if penultimate group effects are significant (there is theoretical data[40] and some experimental evidence[41] to indicate that this is the case). There are also a further series of reactions that need to be considered that involve initiator radical-derived RAFT agents. In principle, RAFT agents of differing reactivity might be derived from each radical species present.

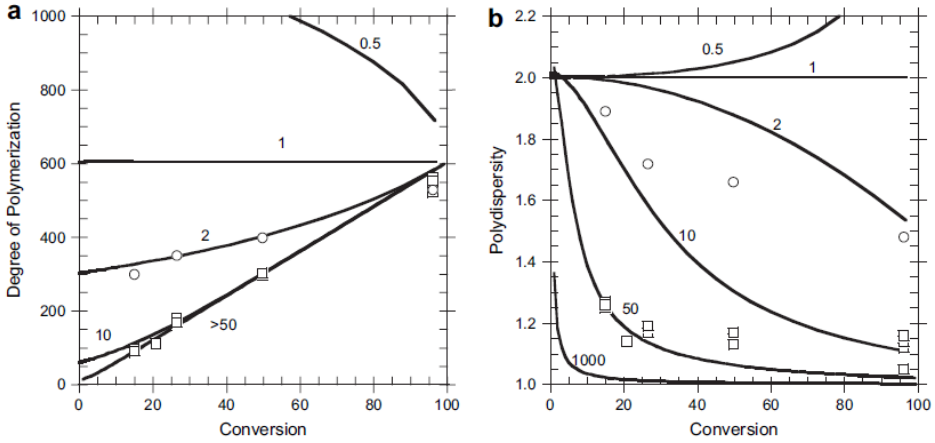

Figure 8. Predicted dependence of (a) degree of polymerization and (b) polydispersity on conversion in polymerizations involving reversible chain transfer as a function of the chain transfer constant (C_{tr}). Predictions are based on equations proposed by Müller et al.

It should be possible to estimate values of K by determining the concentrations of the radical intermediates in RAFT polymerization by EPR (or ESR) spectrometry and some effort has been directed to this end[42]. Coote and coworkers[43] have devised methods for calculating absolute values of K by applying ab initio methods. Values of K have also been estimated on the basis of

simulation of the polymerization kinetics[44]. Values of K estimated on the basis of the measured concentrations of the radical intermediates are substantially lower than those predicted by theoretical calculations.

1.4. RAFT agents

The design of transfer agents, that give reversible addition-fragmentation chain transfer, has provided one of the more successful approaches to living radical polymerization and is described in the next section.

The effectiveness of RAFT agent depends on the monomer being polymerized and depends strongly on the properties of the radical leaving group R and the group Z which can be chosen to activate or deactivate the thiocarbonyl double bond and to modify the stability of the intermediate radicals. For an efficient RAFT polymerization: the RAFT agents must have a reactive C=S double bond (high k_{add}), the intermediate radicals must fragment rapidly (high k_{β}, weak X-R bonds) and give no side reactions, the intermediate must partition in favors of products ($k_{\beta} \geq k_{-add}$) and finally the expelled radicals (R•) must efficiently reinitiate polymerization.

1.4.1. Z group

The Z group modifies both the rate of addition of propagating radicals ($P^{\bullet}_{n}$) to the thiocarbonyl and the rate of fragmentation of the intermediate radicals. The rate constant k_{add} can be "adjusted" over some 5 orders of magnitude through manipulation of Z. The most reactive RAFT agents include the dithioesters and trithiocarbonates which have carbon or sulfur adjacent to the thiocarbonylthio group. RAFT agents with a lone pair on nitrogen or oxygen adjacent to the thiocarbonyl, such as the O-alkyl xanthates, N,N-dialkyldithiocarbamates, and N-alkyl-N-aryldithiocarbamates, have dramatically lower reactivity toward radical

addition. The interaction between the lone pair and the C=S double bond both reduces the double-bond character of the thiocarbonyl group and stabilizes the RAFT agent relative to the RAFT adduct radical. Dithiocarbamates where the nitrogen lone pair is not as available because it is part of an aromatic ring system (such as a pyrrole) or where a carbonyl is α to the nitrogen lone pair have reactivity similar to that of the dithioesters and trithiocarbonates. The effectiveness of xanthates is similarly sensitive to the nature of substituents on oxygen. Monomers can be considered as belonging to one of two broad classes. The "more activated" monomers (MAMs) are those where the double bond is conjugated to an aromatic ring (e.g., styrene (St), vinylpyridine), a carbonyl group (e.g., methyl methacrylate (MMA), methyl acrylate (MA), acrylamide (AM)), or a nitrile (e.g., acrylonitrile (AN)). The "less activated" monomers (LAMs) are those where the double bond is adjacent to saturated carbon (e.g., diallyldimethylammonium chloride), an oxygen, or nitrogen lone pair (e.g., vinyl acetate (VAc) or N-vinylpyrrolidone (NVP)) or the heteroatom of a heteroaromatic ring (e.g., N-vinylcarbazole (NVC)). Propagating radicals with a terminal more active monomer (MAM) unit are less reactive in radical addition (lower k_p, lower k_{add}), and one of the more active RAFT agents is required for good control. The poly(MAM) propagating radicals are relatively good homolytic leaving groups; therefore, retardation solely due to slow fragmentation is unlikely. The more active RAFT agents such as the dithioesters, trithiocarbonates, and aromatic dithiocarbamates allow the preparation of low dispersity polymers from MAMs, whereas the N-alkyl-N-aryldithiocarbamates and the O-alkyl xanthates typically have lower transfer constants and provide poor control. Propagating radicals with a terminal less-activated monomer (LAM) unit are highly reactive in radical addition (higher k_p, higher k_{add}). Accordingly, addition to less active transfer agents such as the N-alkyl-N-aryldithiocarbamates and the O-alkyl xanthates is sufficient that these RAFT agents have high transfer constants in LAM polymerization. However, the

poly(LAM) propagating radicals are relatively poor homolytic leaving groups. Thus, when more active RAFT agents, such as dithioesters, are used in LAM polymerization, fragmentation is slow and inhibition or retardation is likely.

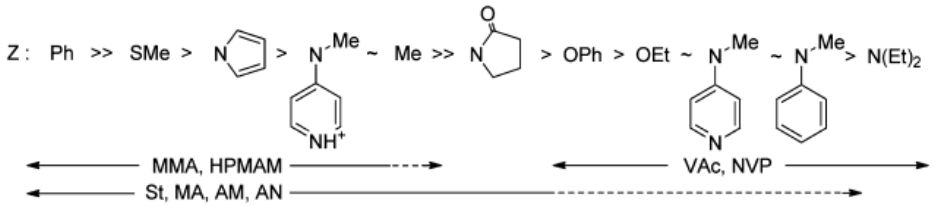

Figure 9. Guidelines for selection of the Z group of RAFT agents (ZC(=S)SR) for various polymerizations. Addition rates decrease and fragmentation rates increase from left to right. A dashed line indicates partial control (i.e., control of molar mass but poor control over dispersity or substantial retardation in the case of LAMs such as VAc or NVP).

General guidelines for selection of Z are shown in Figure 9. Irrespective of the class of RAFT agent, the transfer constant is generally enhanced by the presence of electron-withdrawing groups on Z and by the capacity of Z to stabilize an adjacent radical center. However, these same factors generally can also increase the likelihood of side reactions. The second important role of Z is to determine the stability of the intermediate radicals. When Z is aryl, the intermediate is stabilized, and the rate of intermediate radical fragmentation is slower than when connecting atom of Z is sp^3 carbon, oxygen, or nitrogen or sulfur.

Finally, Z should not cause any side reactions. With xanthates (Z = OR') it is important that R' be a poor homolytic leaving group. Otherwise, fragmentation with loss of R′ (irreversible chain transfer) will compete with the desired RAFT process. This requires that R′ be primary alkyl or aryl. Similar design considerations apply in the case of unsymmetrical trithiocarbonates (Z = SR′). When Z is strongly electron-withdrawing, the thiocarbonyl group may undergo a

direct reaction with monomers. Thus, RAFT agents where Z is alkylsulfonyl or phenylsulfonyl group Z = $PhSO_2$ undergo direct reaction with (meth)acrylate monomers (BA, MA, tBA, and MMA) under polymerization conditions with consumption of the thiocarbonylthio group and ultimately little control over the polymerization. The presence of electron-withdrawing groups on Z, which lead to higher transfer coefficients, increases the likelihood of side reactions such as hydrolysis or aminolysis and participation in cycloaddition reactions such as the hetero-Diels−Alder reaction with diene monomers and 1,3-dipolar cycloaddition. This is an important consideration in some RAFT agent syntheses, can be critical to the choice of RAFT agent for specific polymerization conditions (e.g., in aqueous media or in emulsion polymerization) and determines the ease of end-group transformation processes that may be required post-RAFT polymerization.

1.4.2. R group

The role of R group is determining the partition coefficient ϕ (eq 2). For optimal control of a polymerization, the R group of the RAFT agent (ZC(=S)SR) must be a good homolytic leaving group with respect to $P^{\bullet}_n$, such that the intermediate, formed by addition of $P^{\bullet}_n$ to ZC(=S)SR, both fragments rapidly and partitions in favor of PnSC(=S)Z and $R^{\bullet}$. The expelled radical ($R^{\bullet}$) must also be able to reinitiate polymerization efficiently (i.e., $k_{i,R} > k_p$); otherwise, retardation is likely. Radical stability is important in determining fragmentation rates. Experimental findings that the transfer coefficient and the value of ϕ increase in the series primary < secondary < tertiary and with the introduction of substituents which are capable of delocalizing the radical center are consistent with this view.

It is not sufficient for R to be a monomeric analogue of the propagating radical because penultimate unit effects are substantial, particularly when R is tertiary. RAFT agents with R = 2-ethoxycarbonyl-2-propyl, which can be considered as a monomeric model for a methacrylate chain, provide only poor

control over the polymerization of MMA and other methacrylates because R is a poor homolytic leaving group with respect to the PMMA propagating radical. For similar reasons, RAFT agent with R = t-butyl is poor with respect to RAFT agent with R = t-octyl. These differences in RAFT agent activity are attributed to steric factors. Polar effects are also extremely important in determining the partition coefficient ϕ. Electron-withdrawing groups on R both decrease rates of addition to the thiocarbonyl group and increase rates of fragmentation. The relatively high transfer constants of cyanoalkyl RAFT agents (Figure 10) vs. similar benzylic RAFT agents is attributed to the influence of polar factors.

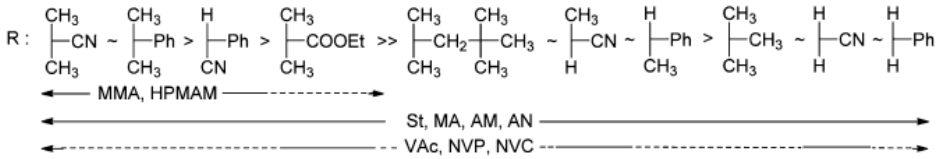

Figure 10. Guidelines for selection of the R group of RAFT agents (ZC(=S)SR) for various polymerizations. Transfer coefficients decrease from left to right. Fragmentation rates also decrease from left to right. A dashed line indicates partial control (i.e., control of molar mass but poor control over dispersity or substantial retardation in the case of VAc, NVC, or NVP).

Thus, control over the polymerization of methacrylates and methacrylamides usually requires that R to be tertiary (e.g., 2-cyano-2-propyl or cumyl) or secondary aralkyl (e.g., α-cyanobenzyl). However, polymerization of monomers with high propagation rate constants (k_p) such as acrylates, acrylamides, vinyl esters (e.g., vinyl acetate), and vinyl amides are best controlled with RAFT agents with primary or secondary R groups. Tertiary radicals, such as 2-cyano-2-propyl radical, are inefficient in reinitiating polymerization since $k_{i,R}$ is often lower than k_p.

The order shown is based on measurements of C_{tr}^{app} for dithiobenzoate RAFT agents in St and MMA polymerization and seems general based on limited data for other classes of RAFT agent. The benzylic radicals and tertiary alkyl

radicals add to most LAMs very slowly (with reference to k_p) and an inhibition period is often observed with these R groups. In the synthesis of a block copolymer comprising segments of a 1,1-disubstuted monomer and a monosubstituted monomer the block comprising the 1,1- disubstuted monomer should be prepared first. Similarly, in synthesizing a poly(MAM)-block-poly-(LAM), using switchable RAFT, the poly(MAM) block should be made first because poly(LAM) propagating radicals are relatively poor homolytic leaving groups, however, poly(MAM) propagating radicals are slow to reinitiate LAM polymerization.

1.5. Design of RAFT agents

The RAFT agents can differentiate mainly into four different classes as dithioesters, trithiocarbonates, xanthates and dithiocarbamates (Figure 11). Moreover there are other compounds (bis- and multi-RAFT agents) that premises to give complex architectures, for example the symmetrical trithiocarbonates can make copolymers as ABBA and star-trithiocarbonates produce dendritic polymers. When a transfer agent is used for the formation of a homopolymer (which then is located at terminals) and when it is chemically bonded to a different macromolecule is called "macrotransfer" or macro-RAFT. A classic example is represented by the transfer members joined to polyetilene oxide (PEO), used for the synthesis of amphiphilic copolymers.

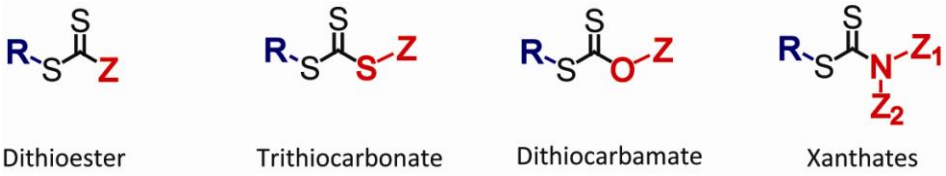

Figure 11. Structure of thiocarbonylthio transfer agents.

The choice of transfer agent must carry the following conditions: that there is polymerization, that the molecular weight should be controlled and that polydispersity obtained should be less than or equal to 1.4. These criteria are dependent on polymerization conditions. It should be pointed out that a broad molecular weight distribution is not by itself an indication that there is a low fraction of living chains and thus it should not be taken as an indication that the RAFT agent is not useful for preparing block copolymers or for preparing end-functional polymers based on the indicated monomer. A more quantitative indication of effectiveness is provided by the transfer constant data. However, such data are, as yet, available for few systems.

A wide range of dithioester RAFT agents have been reported in literature. Examples of unprotected functionality that have been incorporated into the 'R' fragment of dithiobenzoate RAFT agents include hydroxy, carboxylic acid/carboxylate, sulfonic acid/sulfonate, azide, olefin and siloxane. Bis- and multi-dithioester RAFT agents that may be used for triblock or star synthesis. Bis-dithioesters can be used to synthesize triblock copolymers in a two-step process. Dithiobenzoates and similar dithioesters with Z=aryl are amongst the most active RAFT agents, and with appropriate choice of 'R', have general applicability in the polymerization of (meth)acrylic and styrenic monomers. However, their use can give retardation, particularly when used in high concentrations (to provide lower molecular weight polymers) and with high k_p monomers (acrylates, acrylamides). They are also more sensitive to hydrolysis and decomposition by Lewis acids than other RAFT agents.

The utility of trithiocarbonate RAFT agents was disclosed in the first RAFT patent and many papers now describe their application. Trithiocarbonates are less active than dithiobenzoate and similar RAFT agents yet still provide good control over the polymerization of (meth)acrylic and styrenic monomers. More importantly, they give substantially less retardation, are less prone to hydrolytic degradation and, typically, are more readily synthesized. Ideally, to

avoid odour issues with the RAFT agent and polymer the ‘Z’, and preferably the ‘R(S)’groups, should be based on thiols with low volatility. Awide range of trithiocarbonate RAFT agents have now been reported, two classes are distinguished. Non-symmetrical trithiocarbonates have only one good homolytic leaving group. The other S-substituent is typically primary alkyl. Symmetrical trithiocarbonates have two good homolytic leaving groups and the trithiocarbonate group remains in the centre of the structure.

Dithiocarbamate RAFT agents possess two groups "Z", in which Z_2 may be equal to H and also compounds with two dithiocarbamate groups. The relatively low activity of simple N,N-dialkyl dithiocarbamate derivatives in polymerization of styrenic and (meth)acrylic monomers can be qualitatively understood in terms of the importance of the zwitterionic canonical forms (Figure 12) which arise through interaction between the nitrogen lone pairs and the C=S double bond[45]. Electron-withdrawing substituents on Z can enhance the activity of RAFT agents to modify the above order.

Figure 12. Canonical forms of dithiocarbamates and xanthates.

Thus, dithiocarbamate RAFT agents, where the nitrogen lone pair is less available for delocalization with the C=S by virtue of being part of an aromatic ring or by possessing an adjacent electron-withdrawing substituent, can be very effective in controlling polymerization of styrenic and (meth)acrylic monomers.

RAFT polymerization with xanthates is sometimes called MADIX (macromolecular design by interchange of xanthate)[46]. O-Alkyl xanthates have been widely exploited for RAFT polymerization of VAc, NVP and related vinyl monomers where the propagating radical is a relatively poor homolytic leaving

group. They are generally less effective (have low transfer constants) in polymerization of styrenic and acrylic monomers and offer no control for methacrylic polymers. This can be qualitatively understood in terms of the importance of the zwitterionic canonical forms (Figure 12). As is the case with N,N-dialkyl dithiocarbamates, electron-withdrawing substituents on Z can enhance the activity of RAFT agents so that they are more effective in polymerization of styrenic and (meth)acrylic monomers. Thus transfer constants of the O-aryl xanthates are higher than those of simple O-alkyl xanthates. Those of fluorinated xanthates are higher than those of non-fluorinated analogues. O-Alkyl xanthates with appropriate selection of R have transfer constants with acrylates in the range 2-7. This is sufficient to provide end group control at high conversion (it may be possible to make block copolymers) and some trend for increase in molecular weight with conversion. It is not sufficient to provide very narrow molecular weight distributions.

1.6. Polymer architecture

Through the technique of RAFT polymerization very complex polymeric systems can be formed: in this paragraph the synthesis of block copolymers and the growth of polymers from surface of oxides or metal are described. As shown in Figure 13, through suitable RAFT agents and two different monomers (A and B), endless macromolecular architectures can be obtained. From the most simple linear block copolymers to branched polymers of different nature as palm-tree AB_n, H-shaped B_2AB_2, dumb-bell (pom-pom), ring diblock, starblock $(AB)_n$.

In general, polymer grafting techniques provide a versatile tool to covalently modify the surface of materials or oxides[47,48]. These techniques can be categorized into ‘grafting to’ and ‘grafting from’. In the ‘grafting-to’ technique, the polymer, bearing an appropriate functional group, reacts with the material surfaces to form chemically attached chains.

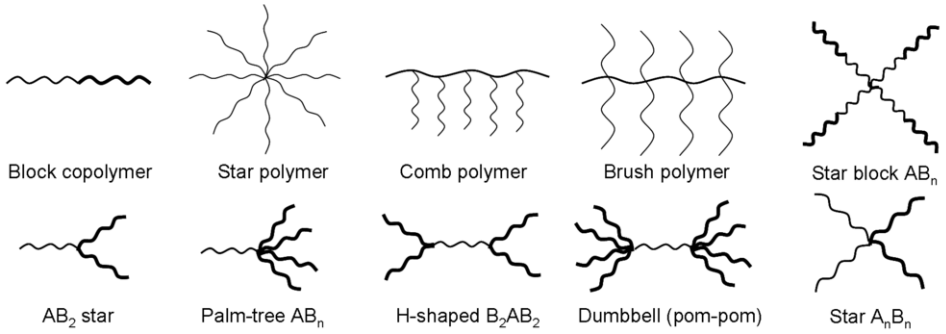

Figure 13. Examples of various complex architectures that can be achieved utilizing two independent blocks (A and B) or segments or a homopolymer structure.

However, due to the steric hindrance imposed by the already-grafted chains, it becomes increasingly difficult for the incoming polymer chains to diffuse to the surface, which intrinsically results in low surface graft densities. In the 'grafting from' technique, the initiators are initially anchored on the surface and then subsequently used to initiate the polymerization of monomer from the surface. Because the diffusion of monomer is not strongly hindered by the existing grafted polymer chains, this technique is more promising to achieve high graft densities. One can also use an intermediate way called "grafting through" that involves a surface on which there are vinyl groups.

1.6.1. Synthesis of Copolymers

RAFT polymerization is recognized as one of the most versatile methods for block copolymer synthesis and numerous examples of block synthesis have now appeared in the literature. RAFT polymerization proceeds with retention of the thiocarbonylthio group. This allows an easy entry to the synthesis of AB diblock copolymers by the simple addition of a second monomer (Figure 14). Higher order (ABA, ABC,etc.) blocks are also possible by sequential addition of further monomers. Of considerable interest has been the ability to make

hydrophilic-hydrophobic or double hydrophilic block copolymers where the hydrophilic block is composed of unprotected polar monomers. As with other living polymerization processes, the order of block construction can be very important. In RAFT polymerization the propagating radical for the first formed block should be chosen such that it is a good homolytic leaving group with respect to that of the second block. For example, in the synthesis of a methacrylate acrylate or methacrylate styrene blocks, the methacrylate block should be prepared first.

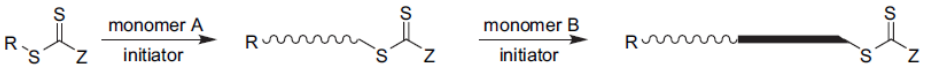

Figure 14. AB diblock synthesis.

The propagating radicals sited on a styrene or acrylate unit are very poor leaving groups with respect to methacrylate propagating radicals and thus the corresponding macro-RAFT agents have extremely low transfer constants in polymerizations of methacrylate monomers.

The use of feed addition protocols, where the monomer concentration is kept low with respect to the RAFT agent concentration, can be used to circumvent this requirement. Such strategies can also allow RAFT agents with lower transfer constants (C_{tr} 0.1-5) to be used in syntheses of polymers with narrow molecular weight distributions. Thus, while a polystyrene macro-RAFT agent appears essentially inert in batch solution polymerization of MMA, PS-b-PMMA has been successfully prepared by feed emulsion polymerization starting with a polystyrene macro-RAFT agent. This strategy is also applied when synthesizing block copolymers from macro-RAFT agents. Another work-around is to maintain a small amount of an appropriate comonomer in the feed. For block copolymers where the leaving group ability of the propagating species is

similar the order of construction is less critical. Thus, in synthesis of block copolymers of styrene with acrylic acid or with acrylate esters either block can be made first.

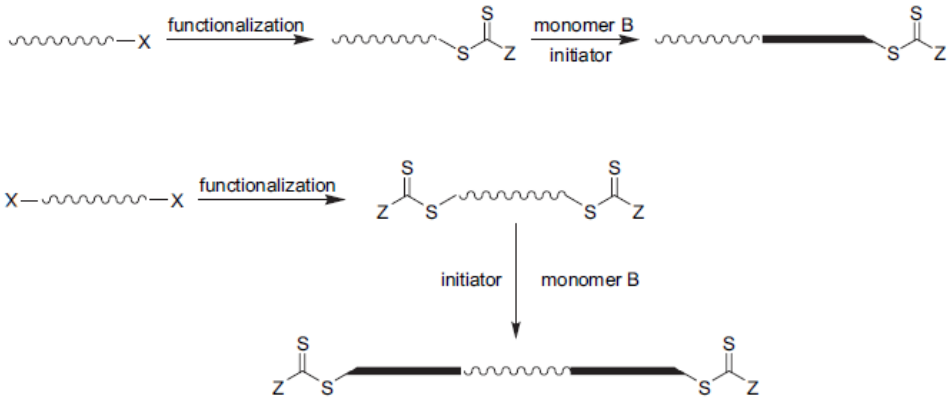

Figure 15. AB diblock and BAB triblock synthesis from end-functional polymers via RAFT process.

Block copolymers based on polymers formed by other mechanisms can be made by first preparing an end-functional pre-polymer which is converted to a polymer with thiocarbonylthio groups by end group transformation. This is then used as a macro-RAFT agent in preparation of the desired block copolymer (Figure 15). This methodology is used to prepare PEO-b-PS from commercially available hydroxy end-functional PEO. Some further examples of this strategy are the synthesis of PEO and PLA block copolymers.

Use of a bis-RAFT agent allows the direct synthesis of triblock copolymers (ABA and BAB) in a 'one-pot' reaction. Symmetrical monotrithiocarbonates can be considered to be in the class of 'Z-connected' bis-RAFT agents.

1.6.2. Grafting

As said above, the RAFT agents have different R and Z groups, which may feature different functionalities that can be used to bind the transfer agent to a surface. The polymerization is greatly influenced in the case in which the group thiocarbonyl is always close to the surface (Z-approach) or on the terminal of the growing polymer (R-approach). It must be considered that since the RAFT technique is relatively new it is difficult to judge which one of the two approaches R- or Z-group approach is better. Decision must be made on a case-by-case basis.

1.6.2.1. R-approach

The R-group approach has the RAFT agent attached on a surface via its leaving group (Scheme 1). Upon chain transfer with a macroradical from solution, the RAFT group is fragmented from the particle surface leaving a radical behind. At the same time, free polymer carrying an RAFT end group is generated in solution. The radical can then react with monomer until a further chain transfer step takes place either with free macro-RAFT agent in solution or with neighboring RAFT groups on the surface. While, termination reactions of radicals located on the surface can theoretically lead to coupling of two nanospheres (in case nanoparticles are used), this event is unlikely due to the remarkable distance. Instead, termination reaction may result in the formation of loops on the surface. These termination reactions are responsible for the limited growth of grafted chains when no additional RAFT agent has been provided. Since, the RAFT agent diffuses away from the surface after the initial chain transfer, the radical on the surface can only react with available adjacent RAFT agents on the surface. However, over time more and more thiocarbonyl thio endgroups depart from the surface into the solution and due to the low

concentrations of RAFT agent in the solution are not very likely to be replaced. Consequently, more and more chains on the surface terminate and therefore stop growing. The termination between two adjacent radicals is dependent on the concentration of immobilized RAFT agents since a high grafting density increases the likelihood of the occurrence of recombinant graft chains. By adding free RAFT agent to the monomer solution the macroradical on the surface can regain the RAFT functionality from the surrounding solution, therefore maintaining the living process. Subsequent cleavage of the grafted chain from the surface for further analysis confirms that the molecular weight of the grafted chain is similar to the molecular weight of free polymer, though the PDI of the grafted chains tend to be higher.

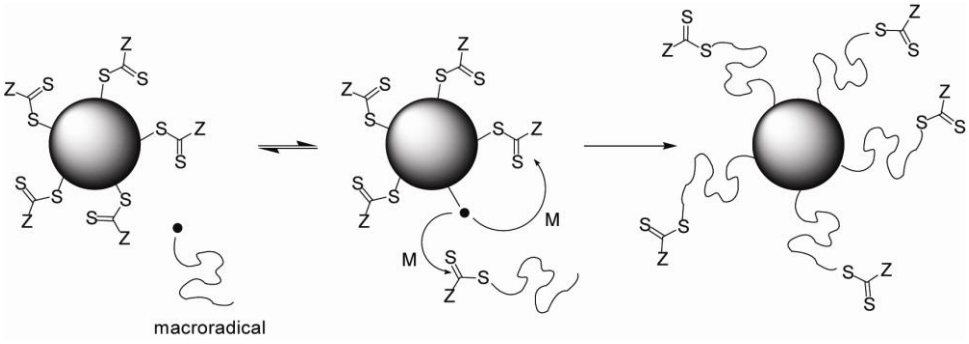

Scheme 1. R- approach scheme.

Studies of T. Fukuda et al.[49] show that the high occurrence of termination events on the surface at a high graft density requires the addition of free RAFT agent to the monomer solution. By reducing the RAFT agent density, and therefore the number of grafted chains, extensive ‘‘surface radical migration’’ can be reduced. As a consequence, the molecular weight and PDIs of the chains on the surface was observed to be similar to the RAFT controlled polymerization in bulk solution.[50]

To maintain a living behavior it is therefore crucial to tailor the amount of immobilized RAFT agents on the surface or to add sacrificial free RAFT agent to the monomer solution. In many cases when grafting via R-group approach, the molecular weight on the surface is measured to be close to the molecular weight in solution. However, the polymer in solution is not always a mirror image of

the grafted one. Effects such as a higher rate of polymerization of surface grafted chains in combination with narrower molecular weight distribution compared to solution polymerization can be explained by the unique structure and steric environment of the surface anchored intermediate macro-RAFT agent radical and also the localized high RAFT agent concentration effect.[51] Many investigations using the R-group approach have been undertaken using silica gel particles.[52] Also other nanoparticles such as gold[53] or CdSe[54] were successfully used to generate core–shell nanoparticles with a well-defined brush layer on the surface. Obviously, termination events on the surface between two macroradicals are the main obstacle in the generation of well-defined surface brushes via R-group approach.

1.6.2.2. Z-approach

The Z-group approach, in contrast, has never radicals located on the surface (Scheme 2). With the initiation of the polymerization, the macroradical needs to diffuse to the surface to undergo chain transfer. After the addition fragmentation step a grafted chain leaves the surface and can diffuse into the solution. Here, the macroradical is subject to termination events if an RAFT agent cannot be reached in time.[55] Investigations by P. Vana ed al.[56] on surface grafted RAFT agents, which were dispersed in a monomer–initiator solution, confirmed indeed the presence of a significant amount of polymeric solution. The macroradical generated in solution was not able to arrive at the surface immobilized thiocarbonyl thio functionality and underwent instead free radical

polymerization. The substantial amount of polymer generated in solution could have two reasons: either the macroradical could not contact the surface since the distance between macroradical and surface was too high or the macroradical was not able to penetrate though the brush layer on the surface and underwent instead termination. In contrast to the R-group approach where thiocarbonyl thio groups migrate into the solution, the dead polymer in solution is colorless indicating the absence of any RAFT group. The distance for a macroradical to travel from solution to surface can be reduced by increasing the concentration of the nanoparticles, thus increasing the surface concentration: this significantly reduces the amount of dead polymer. It is interesting to note that the molecular weight in solution nevertheless increases linearly with conversion.

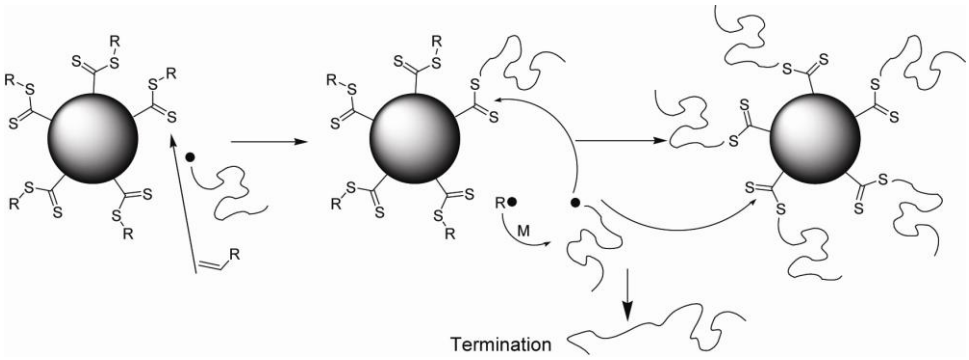

Scheme 2. Z-approach scheme

This behavior is in stark contrast with a free radical process where the molecular weight does not change significantly with conversion. This observation suggests that the terminated polymer was at one stage involved in the controlled process taking place at the particle surface. These dead polymers are probably the result of macroradicals cleaved from the surface after chain transfer but shielded from further chain transfer by the growing brush. Increasing the particle concentrations and thus reducing the distances for the macroradicals to

diffuse can reduce termination events in solution, which will lead to a decrease in molecular weight and a narrowing of the molecular weight distribution of the solution polymer. However, the grafted chain had a lower than expected molecular weight considering the monomer conversion[57] or it was typically smaller than the molecular weight of the free polymer. A more striking feature was that the molecular weight distribution of the grafted polymer was significantly broadened. Better control can be achieved by adding sacrificial free RAFT agent to the monomer solution. The molecular weight distribution of the grafted chain and the polymer in solution was observed to be narrower in size indicating a better control. In addition, the amount of free polymer was significantly reduced. Depending on the system, almost matching molecular weights of the polymer in solution with the grafted polymer close to the expected values were obtained confirming a sufficient control of the surface grafted RAFT agent. But success is not always guaranteed and the molecular weight of the surface grafted chain lags behind the theoretical value. While the molecular weight may be very close to the theoretical value at low conversions, it quickly deviates from the expected linear increase remaining well below the expected molecular weight. At the same time, the free polymer increases, sometimes exponentially, in size. The reduction of the growth of the grafted polymer can be explained by steric hindrance, which prevents the macroradical from re-entering the surface brush. Reducing the loading of surface immobilized RAFT agents does not necessarily improve the grafting process. It was observed that reducing the amount of RAFT agent on the surface -which would lead to brushes of lower density- does result in the opposite effect with the grafted chain increasing even less in molecular weight with conversion. This suggests that the process is indisputably more complicated than expected. It may even be the case that high RAFT agent loading result in a dense brush where the macroradical cannot leave the surface. The entangled macroradical is then in close surrounding of the thiocarbonyl thio group and will feed from monomers diffusing into the brush.

Due to the limited movement of the macroradical in the brush termination reaction may be reduced. Effects caused by chain dynamics should not be underestimated as seen in polymerizations in good and poor solvents. The molecular weight of the grafted chain was found to be increased, when the polymerization was carried out in a bad solvent.

Chapter 2. RAFT agents

The first part of this chapter describes the type of RAFT agent used and the reason for their choice, in particular it is described the difference between the functional groups. Then the synthesis and characterization of the five RAFT agents are reported.

2.1. Why have different agents?

As mentioned in the previous chapter, there are many different types of RAFT agents that differ, beside R and Z groups, also in the "core" of the molecule, which is the part that allows the equilibrium of addition and fragmentation.

In this work RAFT agents of the family of trithiocabonate were investigated because they seemed the most tunable and stable. Moreover, the presence of many studies in literature with similar transfer agents has allowed greater control over the polymerization product. The five synthesized agents were chosen according to Z and R groups functionalities: in particular, functional groups related to the used monomers (styrene, dimethylacrylamide and isoprene) and that would give stable bonds to metal oxides (TiO_2 and SiO_2) and hydroxyl groups, were selected.

In Scheme 3 RAFT agents are shown, with R and Z groups highlighted in blue and red, respectively. In particular, S-1-Dodecyl-S'-(α,α′-dimethyl-α′′-acetic acid) trithiocarbonate (DDAT) is constituted by a functional end with carboxylic acid in the R group in contrast to the 3-benzylsulfanylthiocarbonylsufanyl propionic acid (BSPA) that has acid functionality on Z.

The different positioning of such functionalities, which also allows the dative bond with an oxide, was helpful for the graft polymerization of styrene with both R-approach and Z-approach. Moreover carboxylic acids enable the binding through esterification of the RAFT agents to polymers with terminal hydroxyl, as the PEO. The same transfer agents were tested for the synthesis of block copolymers, in particular BSPA allowed a better control of the polymerization for the PS-PDMA copolymer.

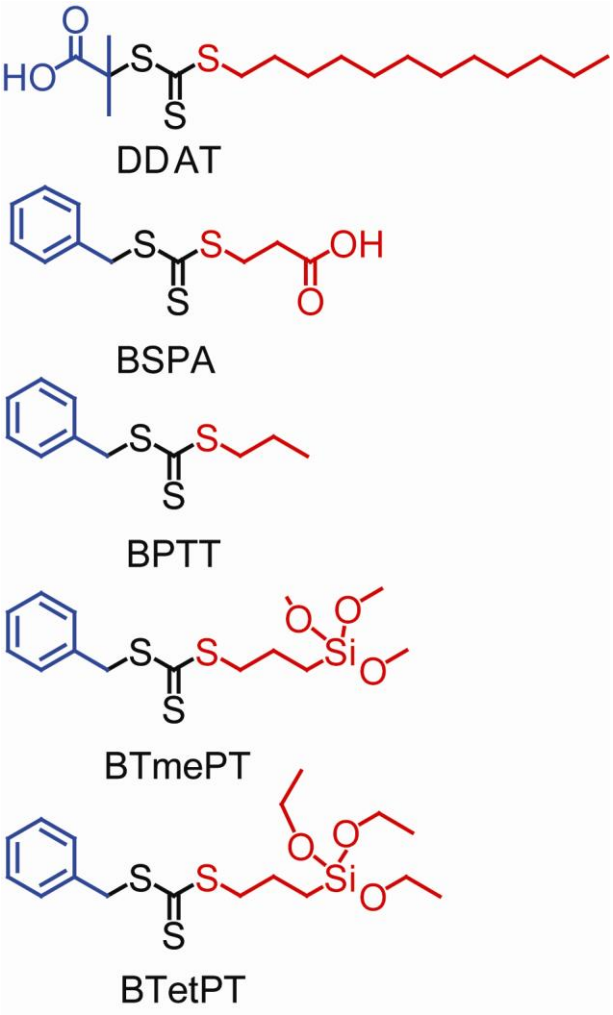

Scheme 3. RAFT agents synthesized R groups (in blue) and Z (in red).

RAFT agents *S*-Benzyl *S'*-trimethoxysilylpropyltrithiocarbonate (BTmePT) and *S*-Benzyl S'-triethoxysilylpropyltrithiocarbonate (BTetPT) were synthesized for grafting polymerization of SiO_2 as they exhibit siloxane functionality, which forms a covalent bond on the surface of the oxide and therefore gives a greater stability between the surface and the RAFT agent. Finally, benzyl S-propyltrithiocarbonate (BPTT) has been produced to have a transfer agent similar to the other two but without siloxane functionality. As discussed in the literature, a RAFT agent in solution, in a process of grafting from via RAFT polymerization, should lead to an improvement of the efficiency of polymerization.

2.2. Synthesis and characterizations

The synthesis of the five RAFT agents was performed as follows. S-1-Dodecyl-S'-(α,α′-dimethyl-α''-acetic acid) trithiocarbonate[58] (DDAT) and 3-benzylsulfanylthiocarbonylsufanylpropionic acid[59,60,61] (BSPA) were synthesized in a similar way to the reported procedure. *S*-Benzyl *S*′-trimethoxysilylpropyltrithiocarbonate[62,63] (BTmePT) and *S*-benzyl *S*′-propyltrithiocarbonate (BPTT) were prepared in accordance with Perrier et al.[64],[65],[66] The last RAFT agent, *S*-Benzyl *S*′-triethoxysilylpropyltrithiocarbonate (BTetPT), is a newly synthesized compound obtained modifying BTmePT synthetic protocol. The characterization was carried out with ^{1}H NMR, ^{13}C NMR, DSC and FT-IR ATR.

2.2.1. DDAT

In a jacketed reactor with mechanical stirring, 48.07 ml of 1-Dodecanethiol (0.20 mol), 120 ml of acetone and 3.24 g of Aliquot (tricaprylylmethylammonium chloride, 8.0 mmol) were added and cooled to 10

°C under a argon atmosphere. Sodium hydroxide solution 50%, (8.38 ml, 0.21 mol) was added dropwise in 20 min. The color changed to white while the reaction was stirred for 15 min. Then, a solution of 24.54 ml of acetone (0.33 mol) and 12.07 ml of carbon disulfide (0.20 mol) were added dropwise in 20 min, and during this time the color turned red. Twenty minutes later, 24.36 ml of chloroform (0.30 mol) was added, followed by dropwise addition of 50% sodium hydroxide solution (40 ml, 1.53 mol) over 30 min. The reaction was stirred overnight. 600 mL of distilled water was added at room temperature, followed by 50 mL of concentrated HCl (37%) to acidify the aqueous solution. The reactor was purged with a nitrogen flow during vigorous stirring to help evaporate off acetone. The solid was collected with a Buchner funnel and then dissolved in 600 ml of 2-propanol. The undissolved solid (recognized as *S*,*S*'-bis(1-dodecyl) trithiocarbonate, dimer of DDAT) was filtered off three times. The 2-propanol solution was dried with mechanical vacuum, and the resulting solid was recrystallized from hexane two times.

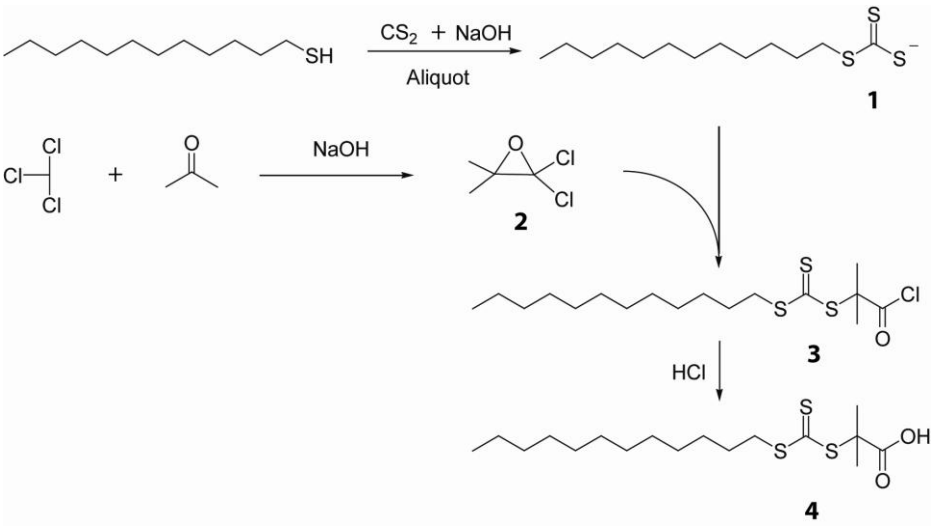

Scheme 4. Reaction Scheme of S-1-Dodecyl-S'-(α,α'-dimethyl-α''-acetic acid) trithiocarbonate.

Yield 47.12 % of yellow crystalline solid; Tm = 61.15 °C was determined by DSC. FT-IR ATR: 1060 cm^{-1} C=S groups, 1703 cm^{-1} C=O groups. ^{1}H NMR ($CDCl_3$): 0.90 (t, 3H, -C**H$_3$**), 1.28 (m, 16H, -(C**H$_2$**)$_8$-), 1.40 (m, 2H, CH_3-C**H$_2$**-), 1.70 (m, 2H, -S-CH_2-C**H$_2$**-), 1.74 (s, 6H, -C**H$_3$**), 3.37 (t, 2H, -S-C**H$_2$**-), 11.90 (s, 1H, -O**H**). ^{13}C NMR ($CDCl_3$): 14.14 (-CH_3), 22.70-31.93 (-(CH_2)$_8$-), 37.07 (-S-CH_2-), 55.61 (-**C**(CH_3)$_2$), 179.18 (C=O), 220.77 (-**C**=S).

To obtain DDAT was introduced into the reactor sodium hydroxide and 1-Dodecanethiol, with a surfactant, to create the thiol anion. The reaction proceeds at 10 ° C under argon atmosphere to avoid the presence of oxygen and the evaporation of the solvent. CS_2 was dropped forming the anion trithiocarbonate (product 1 in Scheme 4), demonstrated by the red color of the solution. After twenty minutes chloroform and sodium hydroxide were added dropwise to acetone and together, already present in solution, producing the epoxide (2) that reacts with ion tritiocarbonato forming the acyl chloride of the desired compound (3). The reaction proceeds to for the night at room temperature. A solution of concentrated acid was added forming S-1-Dodecyl-S'-(α,α'-dimethyl-α''-acetic acid) trithiocarbonate (4). The product was dissolved in 2-propanol and filtered removing the insoluble dimer (S, S'-bis (1-dodecyl) trithiocarbonate).

DDAT RAFT agent was purified by recrystallization from methanol 3 times, the purity of the product was followed by DSC analysis (Figure 16). From the measurements of nuclear magnetic resonance (Figure 17) it was possible to check the purity of the product. The assignment of the peaks in the ^{13}C NMR were performed by comparing similar studies in the literature (Figure 18).

Figure 19 shows the absorption spectrum of the sample the peaks representative of the molecule: 1060 cm^{-1} there is the group C = S and 1703 cm^{-1} the group C = O.

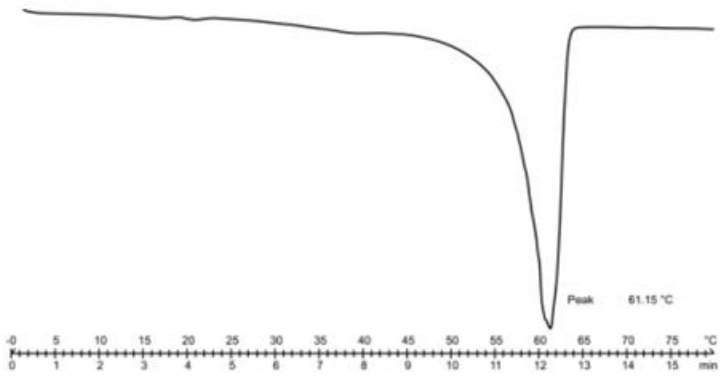

Figure 16. DSC analysis of S-1-Dodecyl-S'-(α,α'-dimethyl-α''-acetic acid) trithiocarbonate.

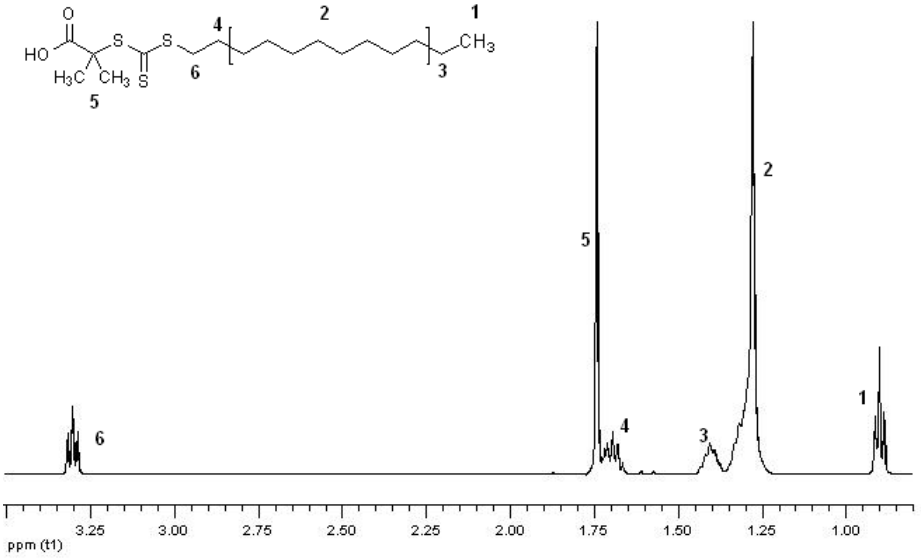

Figure 17. ^{1}H NMR ($CDCl_3$) spectrum of S-1-Dodecyl-S'-(α,α'-dimethyl-α''-acetic acid) trithiocarbonate.

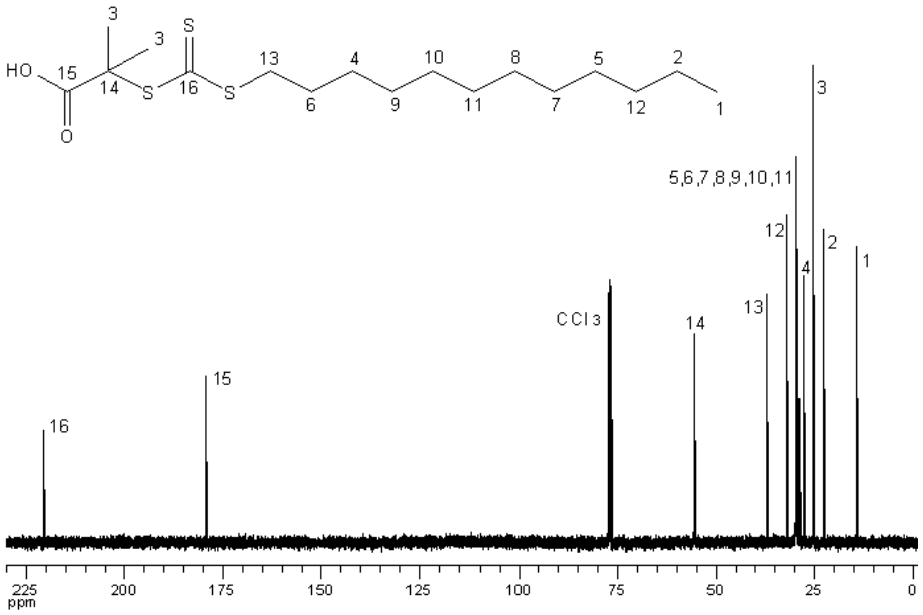

Figure 18. ^{13}C NMR ($CDCl_3$) spectrum of S-1-Dodecyl-S'-(α,α'-dimethyl-α''-acetic acid) trithiocarbonate.

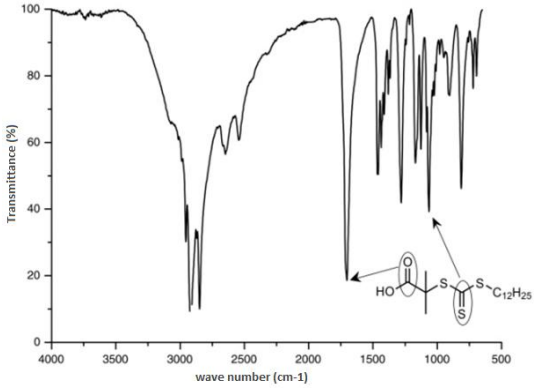

Figure 19. Spectrum FT-IR-ATR of S-1-Dodecyl-S'-(α,α'-dimethyl-α''-acetic acid) trithiocarbonate.

2.2.2. BSPA

Compound 3-(benzylthiocarbonothioylthio)propanoic acid was prepared by adding 10 g of 1-mercapto propionic acid (0.073 mol) to a stirred suspension

of 10.7 g Na_2CO_3 (0.08 mol) in 400 ml acetone and stirring for ten minutes, finally suspension turns orange. 10.68 g of CS_2 (0.022 mol) was added and the solution turned bright yellow. After stirring for ten minutes 10.26 g of benzyl bromide (0.073 mol) was added. Ten minutes later the product was filtered and the solvent was removed under reduced pressure and the residue was added to a saturated solution of brine (700 ml) and extracted with CH_2Cl_2 (2 x 200 ml) and washed with saturated brine solution (3 x 200 ml). After drying the organic extracts over $MgSO_4$ the solvent was removed under reduced pressure to yield a canary yellow crystalline solid. Yield 98 % of yellow crystalline solid; Tm = 83.6 °C was determined by DSC. FT-IR ATR (cm^{-1}): 669, 838, 1068, 1204, 1500, 1690, 2915. ^{1}H NMR ($CDCl_3$): 2.85 (2H, t, S-CH_2-C**H$_2$**), 3.62 (2H, t, S-C**H$_2$**-CH_2), 4.62 (2H, s, C**H$_2$**-Ph), 7.27-7.37 (5H, m, Ph), 9.50-10.05 (1H, COO**H**). ^{13}C NMR ($CDCl_3$): 31.1 (CH_2-S), 33.0 (S-CH_2-**C**H_2), 41.7 (S-CH_2), 127.9-129.3 (4C, Ph), 134.9 (1C, Ph), 177.8 (C=O), 222.8 (-**C**=S).

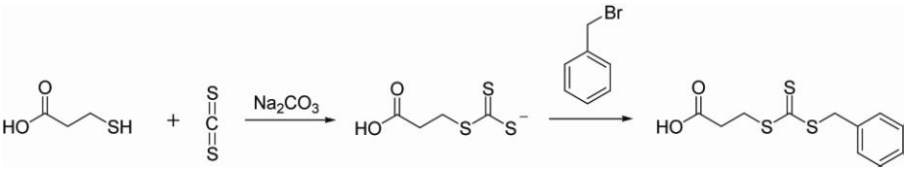

Scheme 5. Reaction Scheme of 3-(benzylthiocarbonothioylthio)propanoic acid.

The synthesis of BSPA was tested both in an aqueous environment, according to the protocols of Davis et al. and in organic environment according to O'Reilly et al. with a yield of 52% and 98% respectively. 1-mercapto propionic acid was deprotonated with sodium carbossido for forming, with CS_2, the anion trithiocarbonates (Scheme 5). After ten minutes was added phenyl bromide, which gave an instantaneous color change. The RAFT agent obtained was filtered and purified by extraction with saturated brine solution and washings. As

seen by ^{1}H NMR analysis (Figure 20) and ^{13}C NMR (Figure 21), the product was pure.

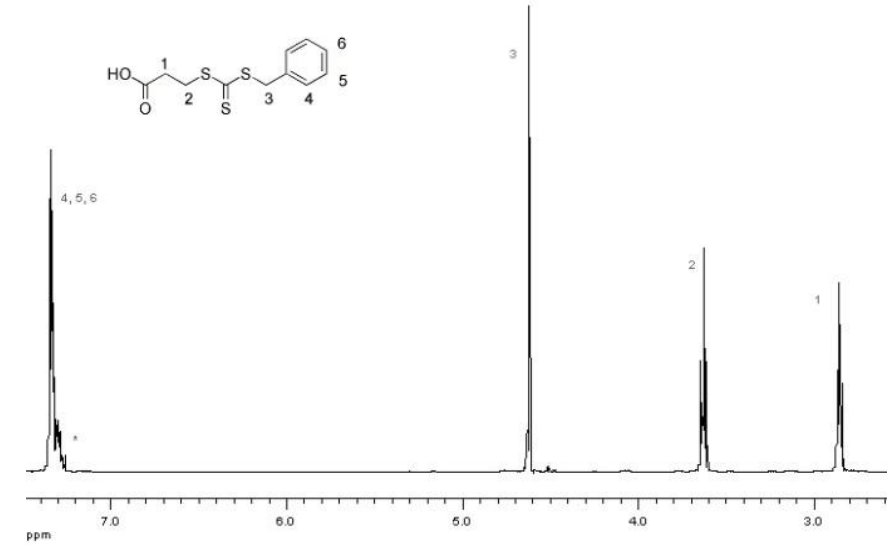

Figure 20. ^{1}H NMR ($CDCl_3$) spectrum of S-1-Dodecyl-S'-(α,α'-dimethyl-α''-acetic acid) trithiocarbonate.

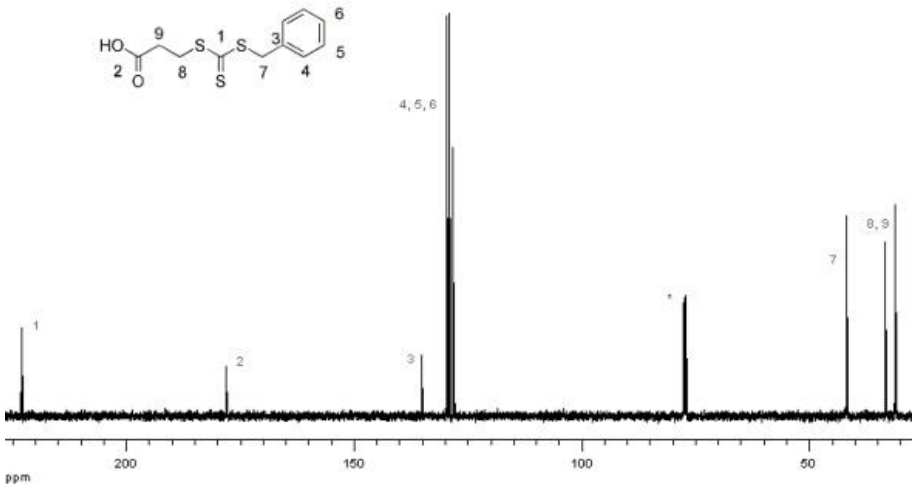

Figure 21. ^{13}C NMR ($CDCl_3$) spectrum of S-1-Dodecyl-S'-(α,α'-dimethyl-α''-acetic acid) trithiocarbonate.

The ATR-IR analysis shown the typical signs of RAFT agent synthesized (Figure 22), 669 cm^{-1} bending of C-H (Ph), 838 cm^{-1} bending of C=S, 1068 cm^{-1} stretching of, 1204 cm^{-1} bending of C-O, cm^{-1} stretching of CH_2, 1500 cm^{-1} stretching of C=C, 1690 cm^{-1} stretching of C=O, 2915 cm^{-1} stretching of C-H and 2500-3100 stretching of OH group.

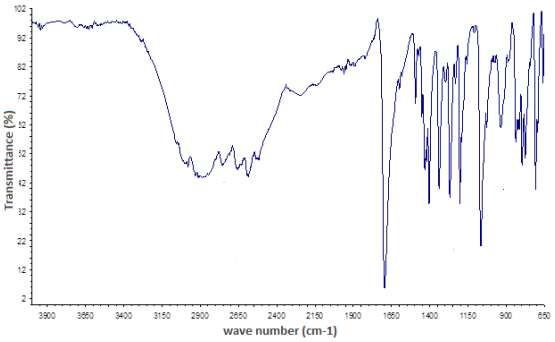

Figure 22. Specto IR-ATR of 3-(benzylthiocarbonothioylthio)propanoic acid.

2.2.3. BTmePT

To a stirred solution of 6.20 g of 3-(mercaptopropyl) trimethoxysilane (95%, 30 mmol) in 50 mL of anhydrous methanol was added dropwise in 6.12 ml of sodium methoxide in methanol (25 wt %, 30 mmol) under argon. After stirring for 30 min, 3.05 g of CS_2 (40 mmol) was added dropwise to the solution, and the mixture was then stirred at ambient temperature for 5 h. To the yellow solution was added 5.24 g of benzyl bromide (98%, 30 mmol), and the mixture was stirred overnight under argon. The mixture was concentrated, diluted with dichloromethane, filtered off, and concentrated under reduced pressure until constant weight. BTmePT (10.8 g, 30 mmol) was obtained as orange oil and stored at 4 °C. Yield 47.12 %. ^{1}H NMR ($CDCl_3$): 0.78 (t, 2H, C**H**$_2$Si), 1.84 (m, 2H, C**H**$_2$), 3.41 (t, 2H, C**H**$_2$S), 3.57 (s, 9H, C**H**$_3$O), 4.61 (s, 2H, C**H**$_2$), 7.33 (m,

5H, Ph). ^{13}C NMR ($CDCl_3$): 223.3 (C=S), 135.4, 129.7, 128.8, 128.4 (PhC), 50.5, 41.3, 39.8, 22.0, 8.8.

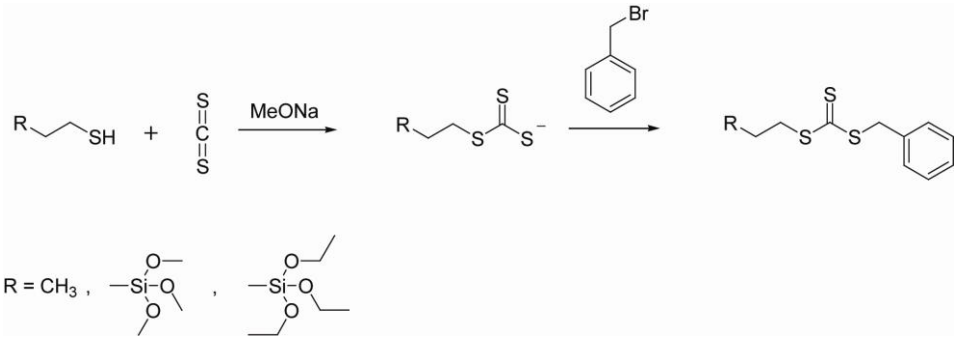

Scheme 6. Reaction Scheme of RAFT agents: benzyl S'-propyltrithiocarbonate 3-(mercaptopropyl) trimethoxysilane and 3-(mercaptopropyl)triethoxysilane.

The BTmePT RAFT agent was synthesized by a multistep process as shown in

Scheme 6. First, 3-(mercaptopropyl) trimethoxysilane was reacted with sodium methoxide in dry methanol, followed by the addition in excess carbon disulfide at ambient temperature. After stirring for 5 h, benzyl bromide was then added to the solution to form the target CTA. The reaction was almost quantitatively conducted in methanol at room temperature, and the purity of the crude products obtained was higher than 95%, as is evident from TLC and ^1H NMR analysis (Figure 23). Because of the potential instability of the trimethoxysilyl group and the severe absorption onto the silica gel column during purification, the resultant RAFT-silane agents were used without further purification. The dense oil has a strong smell and tends to dimerize through the MeOSi groups, so it has been kept in the dark at 4 °C.

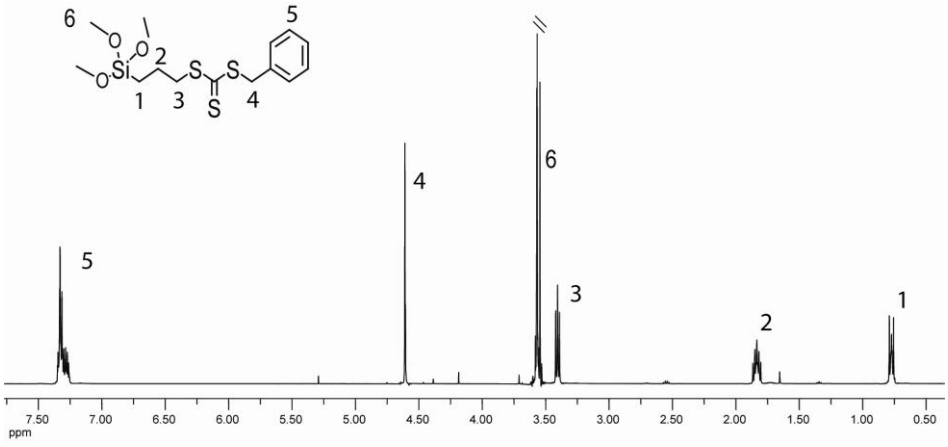

Figure 23. ^{1}H NMR ($CDCl_3$) spectra of S-Benzyl S'-trimethoxysilylpropyltrithiocarbonate.

2.2.4. BTetPT

Compound S-Benzyl S'-triethoxysilylpropyltrithiocarbonate, was prepared similarly to compound with trimethoxysilyl using 1.00 g of 3-(mercaptopropyl) trimethoxysilane (9.43 mmol), 2.15 g of CS_2 (28.30 mmol) and 1.61 g of benzyl bromide (9.43 mmol). The mixture was concentrated, diluted with dichloromethane, filtered off, and concentrated under reduced pressure until constant weight. All procedure of purification were carried over argon and stored at 4 °C, because the product was instable. 10.8 g of S-Benzyl S'-triethoxysilylpropyltrithiocarbonate (30 mmol) was obtained as orange oil and in almost quantitative yield. ^{1}H NMR ($CDCl_3$): 0.78 (t, 2H, C**H**$_2$Si), 1.84 (m, 2H, C**H**$_2$), 3.41 (t, 2H, C**H**$_2$S), 3.57 (s, 9H, C**H**$_3$O), 4.61 (s, 2H, C**H**$_2$), 7.33 (m, 5H, Ph).

As can be seen from Figure 24, the same synthesis procedure was used to synthesize BTetPT RAFT agent. After formation of the anion trithiocarbonate, by means of 3 - (mercaptopropyl) triethoxysilane, sodium methoxide and carbon disulfide, the reaction was progressed with the addition of benzyl bromide. The

purity of the crude products obtained was higher than 98%, as is evident from TLC and ^{1}H NMR analysis (Figure 24). BTmePT is less stable than S-Benzyl S'-trimethoxysilylpropyltrithiocarbonate, with light and temperature a precipitate, attributed to the formation of silane by condensation, was observed. Therefore the product was stored in a schlenk flask with a silicone septum under argon and kept in the freezer.

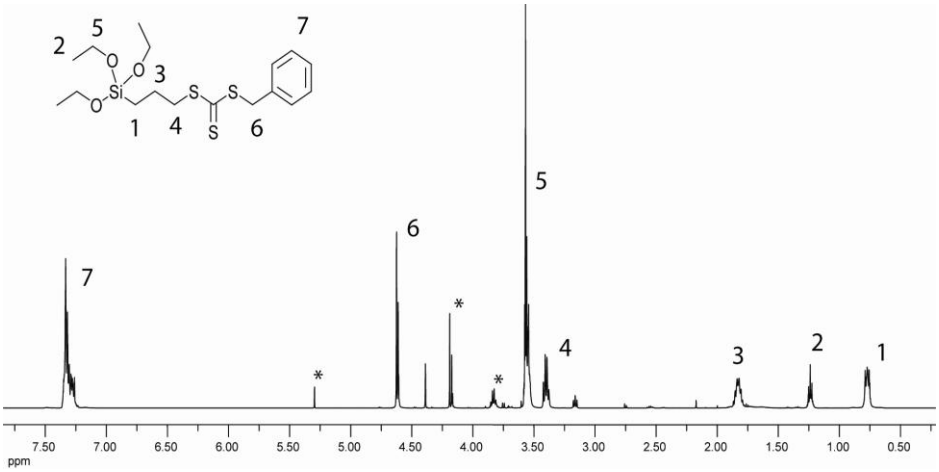

Figure 24. ^{1}H NMR ($CDCl_3$) spectra of S-Benzyl S'-triethoxysilylpropyltrithiocarbonate. *solvent.

2.2.5. BPTT

Compound benzyl S'-propyltrithiocarbonate, was prepared in analogous manner to that of compound with trimethoxysilyl using propyl mercaptan (1.00 g, 9.43 mmol), CS_2 (2.15 g, 28.30 mmol) and benzyl bromide (1.61 g, 9.43 mmol). The mixture was concentrated, diluted with dichloromethane, filtered off, and concentrated under reduced pressure until constant weight. BPTT was purified by silica flash column chloromatography using 5:1 hexane/dichloromethane (v/v) as an eluent and obtained as a yellow liquid

product in 97.1 % isolated yield and it was stored at 4 °C. ^{1}H NMR ($CDCl_3$): 1.03 (t, 3H, C**H**$_3$), 1.74 (m, 2H, CH_3C**H**$_2$), 3.35 (t, 2H, C**H**$_2$S), 4.63 (s, 2H, **CH**$_2$), 7.22-7.38 (m, 5H, Ph). ^{13}C NMR ($CDCl_3$): 223.6 (C=S), 135.0, 129.2, 128.6, 127.7 (Ph), 41.3, 38.8, 21.5, 13.5.

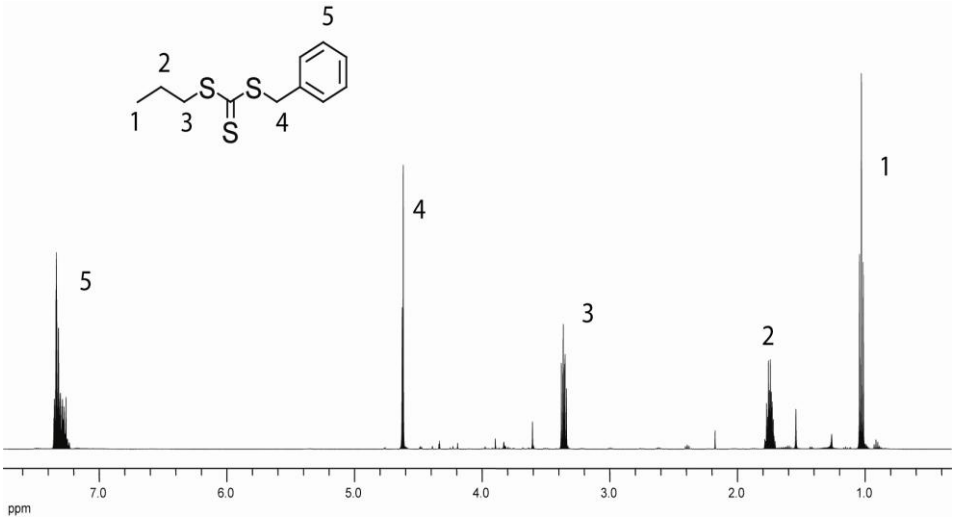

Figure 25. ^{1}H NMR ($CDCl_3$) spectra of benzyl S'-propyltrithiocarbonate.

S-benzyl S'-propyltrithiocarbonate were synthesized according to procedures similar to RAFT-silane agents (Scheme 6). It was possible to purify the product by silica flash column chromatography because siloxane functionality dose not react. The product obtained was stored at 4°C in air. The purity of the crude products obtained was higher than 98%, as it is evident from TLC and ^{1}H NMR analysis as shown in Figure 25.

Chapter 3. Synthesis of block copolymers

In this chapter I will present the synthesis and characterization of amphiphilic block copolymers PS-PDMA and PS-PAA. The process of RAFT polymerization was performed first forming the block of polystyrene using 3-benzylsulfanylthiocarbonylsufanylpropionic acid (BSPA), selected as good transfer agent for this copolymer[67]. Polystyrenes (PS) of different molecular weight were polymerized and then used as macroRAFT agent with N,N-dimethyl acrylamide (DMA) to build the copolymer. Subsequent reaction by hydrolysis with hydrochloric acid changed acrylamide block in acrylic acid (AA). The characterizations were performed via ^{1}H NMR, GPC, DSC and UV-visible.

3.1. General RAFT polymerization of Polystyrene

In a 100 ml schlenk tube with septum 1.5 g (5.51 mmol) RAFT agent BSPA was added and dried in high vacuum to 2 hour. Via a cannula 41.57 ml ($4.41 * 10^{-1}$ mol) of styrene ([M]/[T] = 80) was inserted and degassed with three or more freeze pump thaw cycles. The tube was heated in an oil bath at 110 °C, with magnetic stirring, under argon. After 24 h the mixtures were quenched in liquid nitrogen, the solid product obtained was dissolved with CH_2Cl_2 and precipitated in methanol. After filtering, the sample was dried under high vacuum at 50 °C before use. The polymer was a yellow solid and called PS2.

The polystyrene macroRAFT agents with different molecular weights were prepared employing a similar procedure as above described a different ratio between styrene monomer and RAFT agent (see Table 1.). Molecular weight and

molecular polydispersity was calculated with gel permeation chromatography (GPC).

Sample	M/T	n[f]	Mn_{calcd}[a]	Mn_{NMR}[b]	Mn_{GPC}[d]	Mw_{GPC}	D_{GPC}	Conv(%)[c]	Tg[e]
PS1	40	38	4430	4220	2650	2820	1.06	95	88.25
PS2	80	62	8590	6710	9560	10210	1.06	94	93.80
PS3	100	105	10670	11190	11920	12630	1.06	100	84.00
PS4	125	127	13270	13470	7050	10060	1.42	100	100.62
PS5	125	92	13270	9830	5720	8030	1.40	67	98.67
PS6	150	97	15870	10350	6340	8400	1.32	64	93.23
PS7	250	241	26270	25330	13430	19930	1.48	98	103.45
PS8	250	340	26270	35630	14630	21070	1.44	100	104.11
PS9	500	481	52270	50290	36000	41020	1.13	98	104.53
PS10	1000	973	104270	101460	63340	78920	1.24	97	106.92

Table 1. Synthesis of polystyrene via RAFT polymerization with 3-benzylsulfanylthiocarbonylsufanylpropionic acid. Reaction at 110 ° C, in bulk, argon atmosphere, for 48 h. [a] $Mn_{(calcd)}$ = theoretical molecular weight calculated by monomer conversion. [b] calculated as sum of molecular weight of PS and molecular weight of RAFT agent. [c] % monomer conversion was determined by gravimetry. [d] Mn, Mw and polydistribution analysis was done by GPC with comparison to PS standards. [e] determined by DSC measurement. [f] calculated from the analysis of the ratio between the area of NMR peaks of the methyl of RAFT agent and phenyl of the PS as shown in equation 7.

Conversion was determined gravimetrically and number of monomer units (n_{PS}) was calculated from the ratio between the signals of the ^{1}H NMR peaks of the aromatic group (PS) and methylene group (RAFT agent) as equation 7.

$$n_{PS} = \frac{I_{Ph}\,(PS)}{5} \Big/ \frac{I_{Mt}\,(BSPA)}{2} \qquad (7)$$

where I_{Ph}(PS) is the value of the integral of the phenyl protons of polystyrene and I_{Mt}(BSPA) is the value of the integral of the methylene protons of 3-benzylsulfanylthiocarbonylsufanylpropionic acid. As example, in Figure 27 are shown the ^{1}H NMR spectrums of the sample PS2 and PS3 with relative value of integration.

Ten macroRAFT agents of polystyrene were synthesized changing the ratio between styrene and transfer agent in order to obtain polymers of different molecular weight. The reaction was carried out in bulk and without radical initiator at 110 °C following the procedure identified by O'Reilly et al (Scheme 7).[68] The polymers were dusty solids with an attenuated yellow color compared to the amount of RAFT agent contained. UV-visible measurements showed absorption at 306 cm^{-1} which gradually decreases from sample PS1 to PS10.

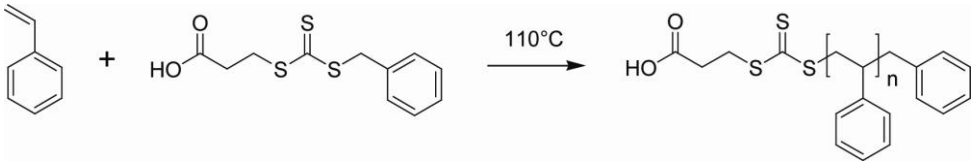

Scheme 7. RAFT polymerization of polystyrene with BSPA.

The samples were analyzed by differential scanning calorimetry by running three thermal cycles. A first heating was performed from 0 °C to 150 °C to remove solvent and traces of water. Then they was subjected to cooling to 0 °C and further heating to 200 °C at 20 °C min^{-1}. Figure 26 shows the trend the glass transition compared to the number of units' monomer. The Tg of the polystyrene grows in relation to molecular weight up to a threshold of about 106 °C.

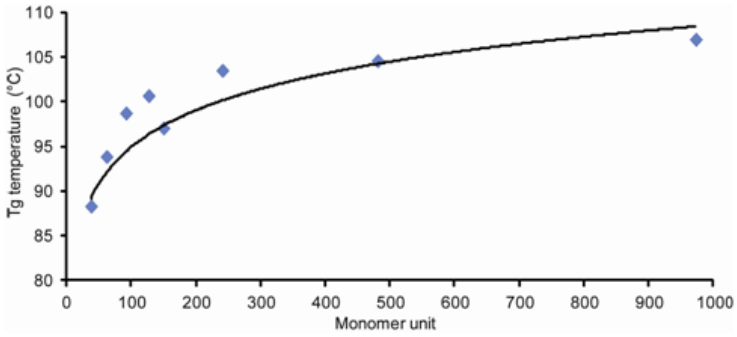

Figure 26. Trend of the glass transition in relation with the molecular weight of the polystyrene macroRAFT.

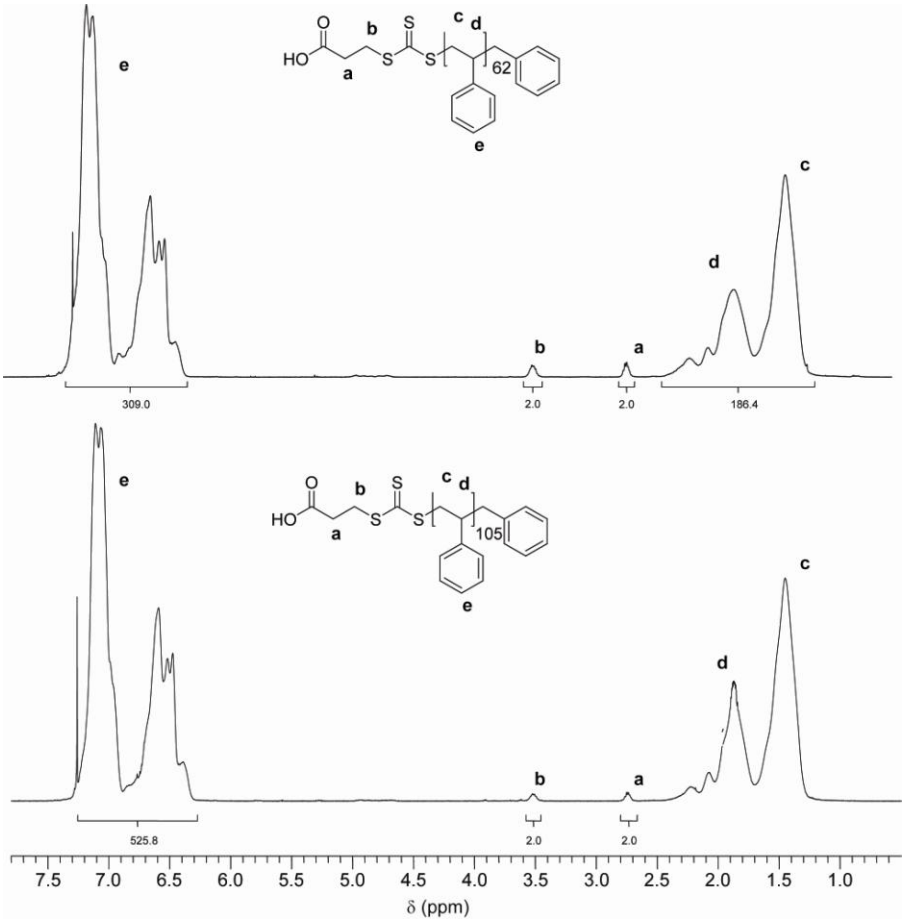

Figure 27. ^{1}H NMR ($CDCl_3$) measurement of PS2 and PS3 with integration values and peaks assignment.

3.2. General RAFT polymerization of block copolymer PS-b-PDMA

RAFT polymerization of block copolymer PS-b-PDMA proceeded as shown in Table 2. 2 g (1.79 * 10^{-4} mol) of PS3 were placed in a Schlenk tube with septum and dried for 2 hours. 9.22 ml (8.96 *10^{-2} mol) of N,N-dimethylacrylamide and a solution of 2.9 mg AIBN (1.80 * 10^{-5} mol) and 2 ml of N,N-dimethylacetamide (DMAc) were added via cannula over argon ([T]/[I] = 10). Solvent was put in to obtain a final volume of 50 mL. The solution was degassed with three or more freeze-pump-thaw cycles. The mixture was heated in an oil bath at 80 °C, with magnetic stirring and argon atmosphere. After 24 h the tube was quenched in liquid nitrogen and the solution was placed in a dialysis tube (MWCO of 3500 Da) and dialyzed against Milli-Q water for 3 days to remove the monomer and DMAc. The water solution was dried in rotavapor and then in mechanical pump for one night at 60°C. The product obtained was a slightly yellow solid.

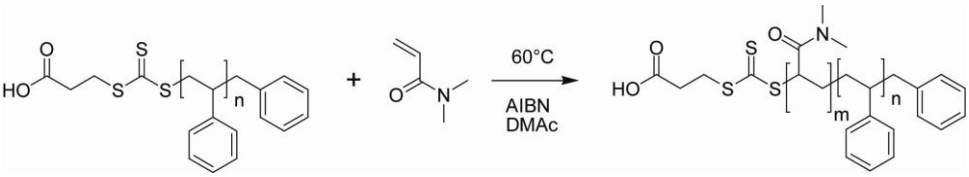

Scheme 8. RAFT polymerization of block copolymer PS-b-PDMA.

Conversion was determined gravimetrically and number of monomer units of the second block (m) was calculated from the ratio between the signals of the ^{1}H NMR peaks of the aromatic group (PS) and Methyl group (PDMA) as equation 8.

$$m_{PS} = \frac{I_{Ph}\,(PS)}{5n} \Big/ \frac{I_{Me}\,(PDMA)}{6} \qquad (8)$$

where I_{Ph}(PS) is the value of the integral of the phenyl protons of polystyrene, I_{Me}(PDMA) is the value of the integral of the methyl protons of N,N- dimethylacrylamide. As example, in Figure 27 are shown the ^{1}H NMR spectrums of the sample PSPDMA_3 and PSPDMA_13 with relative value of integration.

To obtain block copolymers of varied total length (N = n + m) and different polymer fraction of PDMA (f_{PDMA} = m / N) were synthesized in a similar manner as above, varying the type polystyrene block, the reaction time and the solvent.

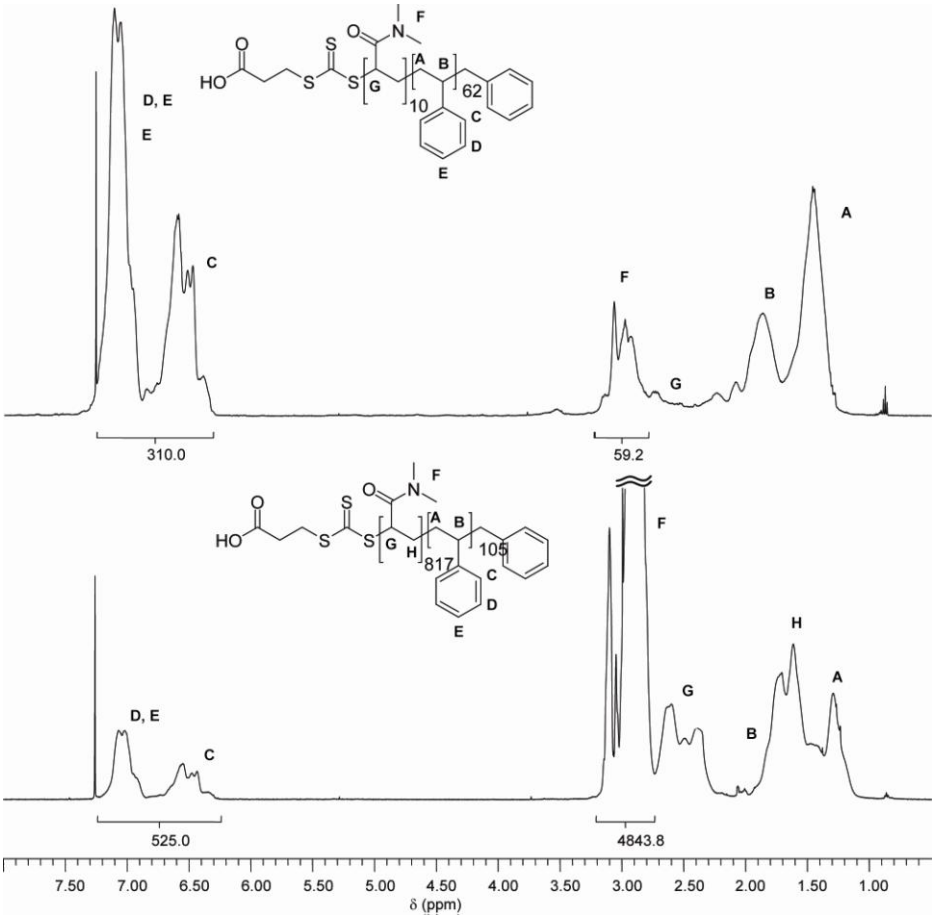

Figure 28. ^{1}H NMR ($CDCl_3$) measurement of PSPDMA_3 and PSPDMA_13 with integration values and peaks assignment.

In Table 2 are listed all the samples synthesized with the corresponding fraction of the monomeric units of the hydrophilic block. The difference between the molecular weights obtained and theoretical molecular weights is attributable to the dialysis process that may lead to a selection of molecular weights. The copolymer PS-b-PDMA is partially soluble in tetrahydrofuran and therefore it was not possible to find a precise correspondence between the molecular weights determined by nuclear magnetic resonance and gel permeation chromatography. Any case the dialysis process ensures the formation of the block copolymer.

To better visualize the ratio between the two block polymers of polystyrene and polydimethylacrylamide, it was built a graph (Figure 29.) in which the proportion between n and m for all the copolymers was respected.

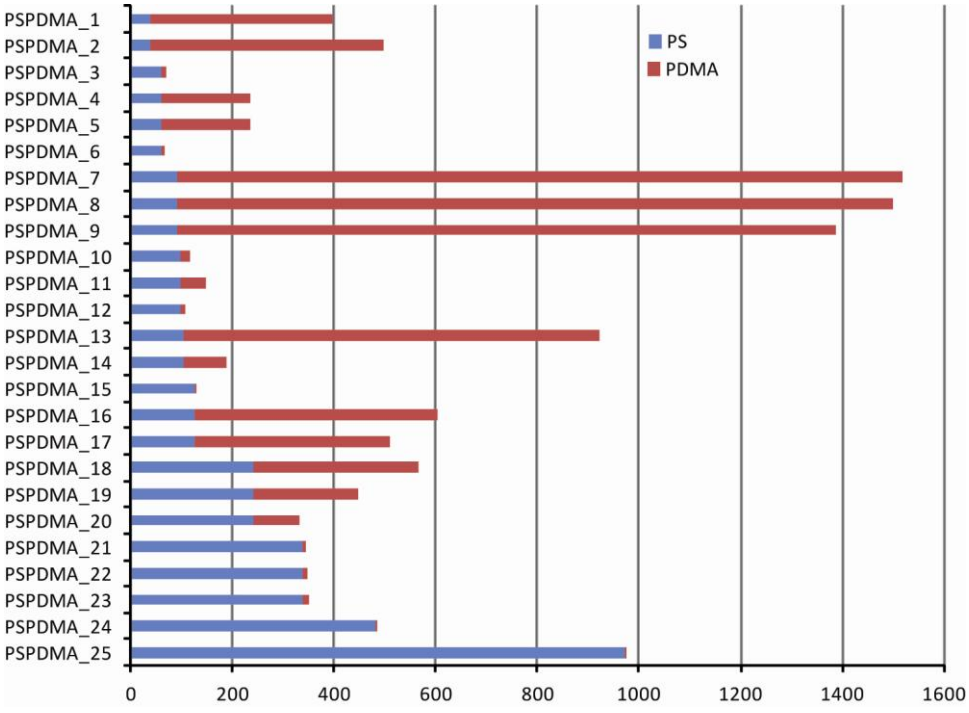

Figure 29. Schematic representation of the copolymers PS-b-PDMA.

PS block	Sample	nPS	$t_{reaction}$ (h)	Mn_{caled} [a]	Mn_{NMR} [b]	m_{PDMA} [c]	f_{PDMA} [d]	Solvent
PS1	PSPDMA_1	38	4	53450	53456	360	0,90	Dioxane
PS1	PSPDMA_2	38	5	53450	42339	460	0,92	Dioxane
PS2	PSPDMA_3	62	2	55940	7438	10	0,14	DMAc
PS2	PSPDMA_4	62	4	55940	23773	175	0,74	DMAc
PS2	PSPDMA_5	62	6	55940	23674	174	0,74	DMAc
PS2	PSPDMA_6	62	2	55940	7116	4	0,06	DMAc
PS5	PSPDMA_7	92	4	59060	150915	1425	0,94	Dioxane
PS5	PSPDMA_8	92	0.5	59060	149034	1406	0,94	Dioxane
PS5	PSPDMA_9	92	0.1	59060	138144	1296	0,93	Dioxane
PS6	PSPDMA_10	97	1	59580	12340	20	0,17	DMAc
PS6	PSPDMA_11	97	0.7	59580	15310	50	0,34	DMAc
PS6	PSPDMA_12	97	0.5	59580	11548	12	0,11	DMAc
PS3	PSPDMA_13	105	24	60660	92045	817	0,89	DMAc
PS3	PSPDMA_14	105	4	60660	19478	84	0,44	DMAc
PS4	PSPDMA_15	127	1.5	62700	13876	4	0,03	DMAc
PS4	PSPDMA_16	127	4	62700	60703	477	0,79	Dioxane
PS4	PSPDMA_17	127	7	62700	51496	384	0,75	Dioxane
PS7	PSPDMA_18	241	20	74560	57709	327	0,58	DMAc
PS7	PSPDMA_19	241	2	74560	45928	208	0,46	DMAc
PS7	PSPDMA_20	241	3	74560	34345	91	0,27	Dioxane
PS8	PSPDMA_21	340	2	84860	36226	6	0,02	DMAc
PS8	PSPDMA_22	340	4	84860	36523	9	0,03	DMAc
PS6	PSPDMA_23	340	6	84860	36622	10	0,03	DMAc
PS9	PSPDMA_24	481	4	99520	50791	5	0,01	DMAc
PS10	PSPDMA_25	973	4	150690	101761	3	0,01	DMAc

Table 2. RAFT polymerization of block copolymer PS-b-PDMA. Reaction at 80 °C in DMAc or 1-4,dioxane, over argon with AIBN as initiator. . [a] $Mn_{(calcd)}$ = theoretical molecular weight calculated by monomer conversion. [b] calculated as sum of molecular weight of PS and molecular weight of PDMA. [c] calculated follow equation 2. [d] calculated as ratio between m and N(=n+m).

3.3. Synthesis of block copolymer PS-b-PAA

130 mg (1.82 * 10^{-4} mol) of PSPDMA_3 ($PS_{62}PDMA_{10}$) and 15 ml of 1-4,dioxane was mixed in the two-necked flask with magnetic bar. A solution of 0.5 ml (3.00 * 10^{-1}mol) of HCl (6 M) was added and the system was placed in bath oil at reflux. After 48 h the solution was transferred to a dialysis tube (MWCO of 3500 Da) dialyzed against Milli-Q water until to a neutral solution. The product was dried in a rotavapor and in vacuum at a temperature of 50 °C. The pale yellow solid obtained was analyzed by ^{1}H NMR and IR-ATR spectroscopy.

To obtain an amphiphilic block copolymer of equal molecular weight and molecular weight distribution the copolymers PS-b-PDMA were hydrolyzed with hydrochloric acid in a similar way to Hillmyer et al.[69] The hydrolysis process allows the replacement of acryl amide groups in the acrylic acids (Scheme 9). Was carried out for samples PSPDMA_3 and PSPDMA_19 obtaining $PS_{62}PAA_{10}$ and $PS_{241}PAA_{208}$.

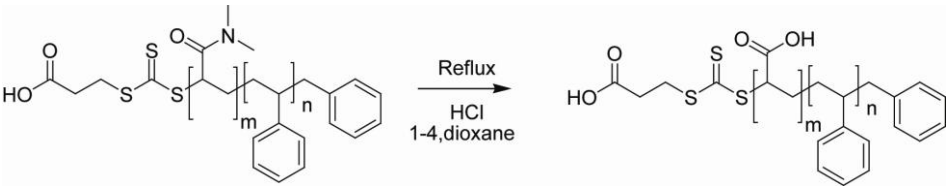

Scheme 9. Hydrolysis of block copolymer PS-b-PDMA.

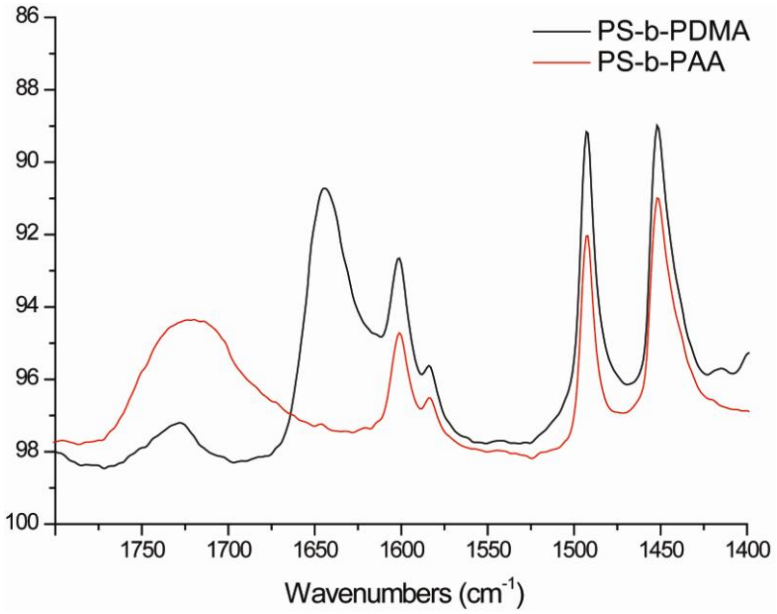

Figure 30. IR spectra of block copolymers: (a) $PS_{62}PDMA_{10}$ (BC), (b) $PS_{62}PAA_{10}$, after hydrolysis.

^{1}H NMR analysis verified the absence of the peaks of polydimethylacrylamide. Figure 30 shows IR spectra of hydrolyzed PS-PDMA copolymer. Peaks at 1655 and 1624 cm^{-1}, corresponding to the carbonyl stretch in PDMA (free and H-bonded, respectively), are replaced by the peaks at 1729 and 1755 cm^{-1}, attributed to the carbonyl groups of PAA (free and H-bonded, respectively).

Chapter 4. Self-assembly of the block copolymers

In this chapter I will present the study of the self assembly in selective solvent of amphiphilic PS-PDMA block copolymers synthesised as described in Chapter 3. Full characterization of nanomaterials can be achieved only with the comparison of several different techniques, especially in the case of nanoparticles. Thus, I compared nuclear magnetic resonance spectroscopy, dynamic light scattering and electron microscopy on the same systems. Furthermore, fluorescence spectroscopy was used as new method to characterize the self assembly. For this technique the mechanism and the class of molecular rotors used will be explained in detail.

In particular, I have studied the samples $PS_{105}PDMA_{816}$ (PSPDMA_13) and $PS_{62}PDMA_{10}$ (PSPDMA_3).

4.1. Introduction

Block copolymers dispersed in a selective solvent can self assemble in a large variety of aggregated structures. Depending on the balance between solvophilic and solvophobic components, polymer chains arrange as spherical micelles, wormlike micelles, polymersomes (see Figure 31). In water, the hydrophobic block forms either the core in micelles or the walls in bilayer structures, while the hydrophilic block forms the corona.

The morphological complexity of copolymer aggregates is due to the non-ergodicity of the self assembly: the organization of block copolymer chains is highly dependent on the kinetic pathway.[70] Once the aggregate is formed a large energy gap prevents the transfer of a single molecule form the micelle to the

solution. Moreover the formation of glassy core traps metastable structures hampering the possibility of fusion or fission of the micelles.

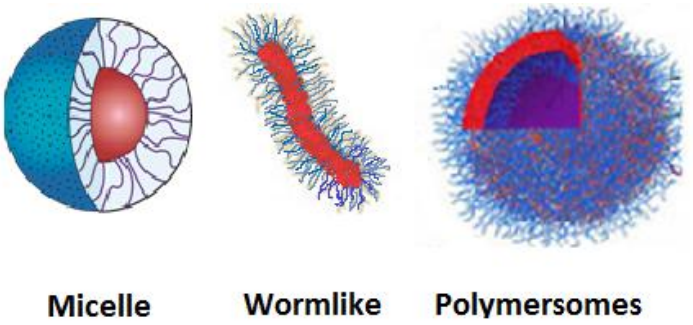

Figure 31. Different morphology of self-assembly of block copolymer.

A precise control of the aggregates' morphology can be obtained only if the pathway of self-assembly is completely dominated. An answer to this point can be found in the detailed recipes reported in literature for the preparation of well-defined morphologies.[71] However the efficacy of the procedure can be verified only ex-post.

In particular, the monitoring of the micelle formation as a consequence of the solvophobic effect, induced by an increasing amount of water in the organic solvent, cannot be easily accessed through common macromolecular characterization tools. Dynamic Light Scattering can provide a precise evaluation of the average dimension of the micelles but provides no insight regarding the intimate structure of the micelle, since it provides an average hydrodynamic radius that comprises both the formation of a glassy core or of a highly flexible corona. On the other hand, TEM and cryo-TEM images of the micelles can be extremely detailed with particulars of the various components the polymeric objects; however in this way micelles are removed from their native environment and uncontrolled phenomena can alter dimension and shape of the nanoobjetcs. An interesting, and probably extreme, example of this alteration is reported by

Eisenberg et al. describing the formation of "kippah" vesicles.[72] Even in absence of alteration, the immobilization of the micelles onto a flat surfaces drastically hampers their dynamics. On the other hand, considering one of the main envisaged applications of block copolymer micelles, drug delivery, dynamical properties of the polymer chain directly determine the uptake/release and diffusion of active molecules in the micelle.[73] In the case of core-shell micelles, if the core-forming block has glass transition temperature (T_g) far above room temperature, the drug is trapped by frozen polymer chains and cannot be released to the target. However confinement effects can alter significantly the T_g at the nanoscale and no simple comparison can be made with the bulk T_g. For this reason several attempts have made for determining the glass transition temperature of polymeric micelles but no technique of choice has been univocally defined.

In fact, calorimetric techniques have been successfully applied mainly in case of micelles prepared in low volatile solvents[74] or ionic liquids.[75] When the selective solvent is water, unless T_g is close to ambient temperature, DSC measurements become problematic due to evaporation, which would lead to extensive denaturation of the core shell structures.

^{1}H Nuclear Magnetic Resonance spectroscopy is quite sensitive to molecular motions especially in terms of resonances line-widths, and it allows to determine the glass transition temperature when the peaks corresponding to the core-forming polymer, as function of decreasing temperature, become so large to disappear into the baseline. [76] As a consequence if in a ^{1}H NMR spectrum all the signals of a block are missing we can reasonably assume that at the measuring temperature that block is below T_g.[77,78,79]

Finally, Fluorescence Spectroscopy is particularly suited to study polymer aggregation in micelles, since it can exploit several fluorescent probes whose fluorescence emission is sensitive to changes of properties, such as polarity, fluidity, order, molecular mobility. For this purpose, the most used probe is

pyrene. Pyrene modifies its spectroscopic properties going from water to the micelles interior as a consequence of the different monomer/excimer ratio.[80,81,82]

Dynamics inside the nanostructures can be studied by analyzing the time resolved fluorescence decay of pyrene. The fluorescence decay is function of the kinetics of pyrene excimer formation, hence when the mobility of pyrene decreases due to an increase of medium viscosity, less excimers are formed and the fluorenscence lifetime increases. The same mechanism holds for naphthalene or phenantrene labeled micelles.[83,84,85,86] More recently Mok and Lodge described a method to determine the T_g in block copolymer micelles based on pyrene fluorescence: the technique consists in monitoring the intensity ratio between the first and third spectral peaks (I_3/I_1) of pyrene emission spectrum as function of temperature.

4.1.1. Molecular rotors

Molecular rotors are fluorescent probes widely used in biology and in polymer science to study dynamical processes (polymerization kinetics, thermal transitions, photodegradation, swelling) in bulk[87] and thin films,[88] nevertheless very few studies of molecular rotor fluorescence in block copolymer micelles are reported in literature[89].

Molecular rotors have the characteristic of changing their emissive properties as a function of the medium viscosity in which they are dispersed. In particular, the luminescence lifetime and quantum yield (QY) of a molecular rotor increase on increasing of system viscosity. This feature is a consequence of the fact that, generally, the molecular rotors possess at least two distinct rigid conjugated sections, connected by a single bond, able to rotate relative to one another. Hence, an increase of local viscosity around the molecular rotor induces a decrease of the intramolecular rotations (decrease of the nonradiative process) thus resulting an increase of the luminescence lifetime and QY. Probably the

most studied molecular rotor is Thioflavine-T (see Figure 32). Its structure contains a benzothiazolium ring and a dimethylaniline moiety connected by a single carbon-carbon bond. Depending on the local viscosity and/or aggregation state, the rotation around the single bond can be partially or completely hindered with strong consequences on the conjugation. The thioflavine-T emission efficiency can be increased by 2 orders of magnitude thanks to this effect.

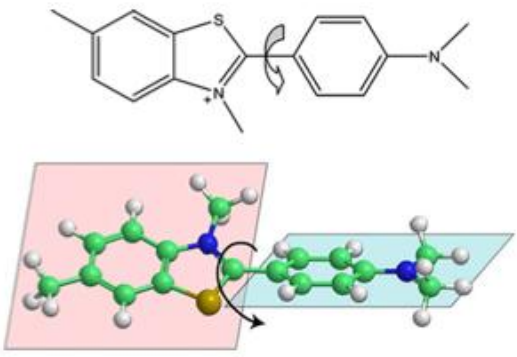

Figure 32. Scheme of molecular rotors (thioflavine-T).

For exploring the PS-PDMA structuration, a specifically designed molecular rotor was used as a fast, very sensitive and non-invasive tool for the direct monitoring of the self assembly of copolymeric micelles in water. The luminescent molecular rotor was used also as a probe for the local viscosity of the rigid polystyrene core of core-shell micelles. Figure 33 shows the structure, UV-Vis absorption and steady state emission of the new, molecular rotor AzeNaph1. Coherently with the structural features of other luminescent rotors, AzeNaph1 is dipolar, possessing an electron rich unit, the dibenzoazepine ring, and an electron poor one, the naphthaleneimide. The two units are in more or less free rotation – depending on local viscosity - around the carbon-nitrogen bond connecting them. The molecule is moderately luminescent in organic solvents

solution (quantum yield around 20%), completely insoluble in water and only slightly soluble in alcohols. The coupling between the two units is particularly strong as the central ring of the dibenzoazepine residue is antiaromatic (having 8 π electrons) thus making its nitrogen atom a very efficient donor. The derivative was straightforwardly prepared by a Buckwald –Hartwig arylation reaction of dibenzoazepine with the suitable 4-bromonaphthalene imide. Finally, AzeNaph1 is characterized by an absorption and emission peak at about 410 and 500 nm, respectively. The relatively large Stokes shift also implies very limited reabsorption, increasing the range of possible applications in materials science and imaging.

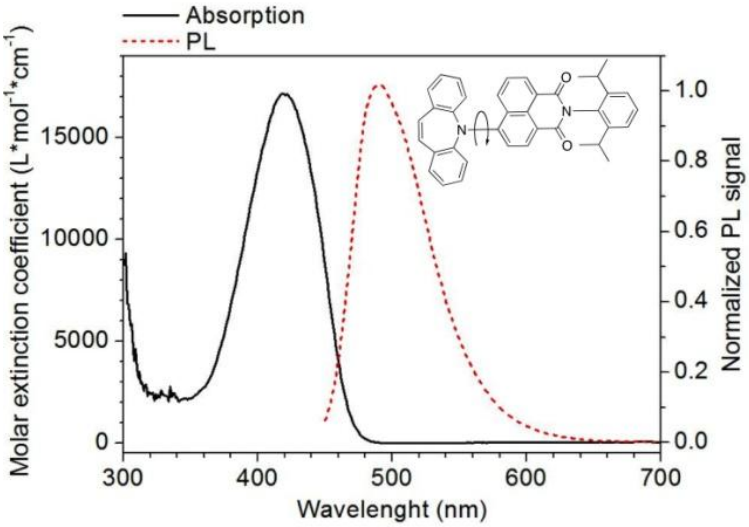

Figure 33. Structure and UV-Vis Absorption/Steady State fluorescence of AzeNaph1 in a 10-5 [M] MMA solution.

In order to validate the role of viscosity probe of AzeNaph1, a preliminary study on its luminescence properties was carried out. In particular, in Figure 34a the time decay profile of the AzeNaph1, acquired before and during the polymerization of T~55°C in a styrene solution containing lauryl peroxide as the

radical polymerization initiator, is reported. The figure shows that lifetime, characterized by a single exponential decay, increases monotonously as the polymerization proceeds. We were able to clearly see an increase even before the macroscopic gelation of the reaction mixture, indicating the technique is extremely sensitive to the local variations of viscosity. After the completion of the polymerization, the fluorescence lifetime (τ_f) was about 5.8 ns (see the blue line in Figure 34a). On the other hand, before the polymerization by heating the sample, was estimated that $\tau_f \leq 1$ ns (see the black line in the same Figure 34a).

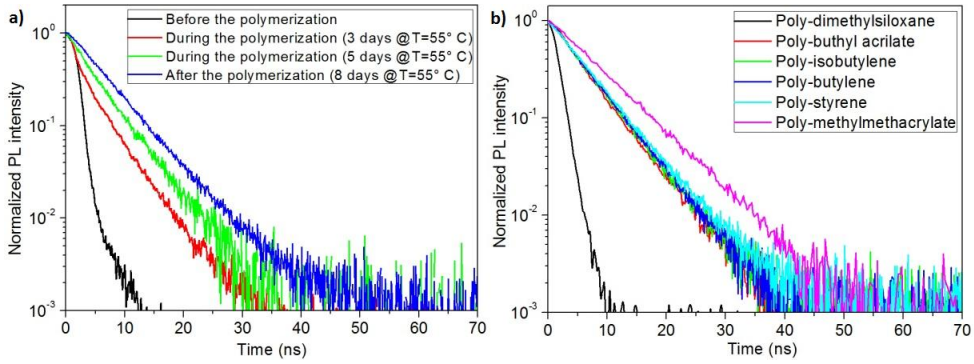

Figure 34. a) Time decay profile of the AzeNaph1 acquired before and during the polymerization. 10 mL ($8.7 * 10^{-2}$ mol) of styrene, 2.2 mg ($5.6 * 10^{-6}$ mol) of lauryl peroxide and AzeNaph1 (4 M) were mixed. After stirring and degassing the solution was placed in a vial at 55°C until completely solidification (8 days). Life time measurements were carried out before, during (3^{rd} and 5^{th} days) and after the polymerization. b) decay profiles of the AzeNaph1dispersed in different polymers at room temperature. 10 g of polymer (PDMS, PnBA, PIB, PB, PS and PMMA), 2 mg of AzeNaph1 and 50 ml CH_2Cl_2 was mixed and casted to Teflon petri. After complete evaporation, the film was dried in a vacuum for 24h. Absence of solvent was verified by DSC analysis. The samples were excited at 405 nm and monitored at 480 nm.

It is worth noting that this value was overestimated as a consequence of the instrument time resolution. For this reason, the time decay profile of this sample (not shown here) was also acquired with a streak camera experimental set up

characterized by a better resolution. With that setup, a $\tau_f \sim 0.36$ ns was obtained. Also, the decay profiles of rotors dispersed in various polymers, with different T_g, were studied (see Figure 34b). All the samples exhibit an exponential decay with τ_f falling in the range 1.3÷7.4 ns. These different τ_f cannot be directly attributed to different microviscosities of the samples when heterogeneous samples were considered, but also to the specific interactions due to the chemical nature of each polymer. Indeed, the relation linking τ_f and η, known as Förster-Hoffmann equation, depends also on the system composition in which the molecular rotor is dispersed.[90]

4.2. Self assembly of $PS_{105}PDMA_{817}$

A solution of 1 ml of DMF and 20 mg of copolymer $PS_{105}PDMA_{817}$ (PSPDMA_13, see Table 2, cap 3) was prepared under stirring with magnetic bar. After 24 hours 5 ml of Mill-Q water were dropped with a rate of 2 ml min^{-1} under continuous stirring. The mixture was then stored at least 1 hour prior the measurement. A similar mixture was prepared using toluene as selective solvent. Both the addition of H_2O and toluene formed dispersions with a cloudy appearance, indicating presence of structures in the tens to hundreds of nm size range.

The measurement with dynamic light scattering performed on the DMF+H_2O dispersion (see Figure 35) shown the presence of particles with a hydrodynamic diameter of 90 nm with a very sharp polydispersity (Pld = 0.098). This suggests the formation of nanostructures given by the self assembly of the copolymer and was a consequence of the high control on the copolymer molecular weight and polydispersity. On the other side, the solution prepared with toluene shows a polymodal distribution, typical of not regular macro or nanostructures.

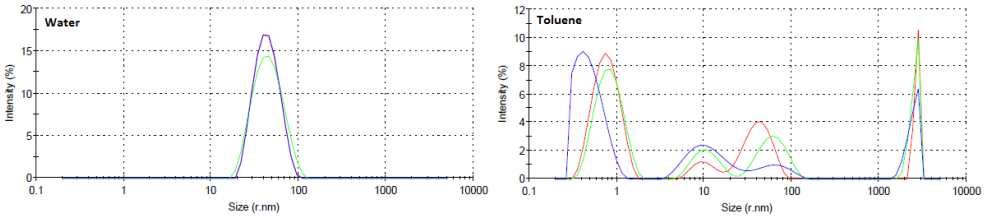

Figure 35. DLS measurement of water (lift) and toluene (right) solution of $PS_{105}PDMA_{817}$.

4.2.1. NMR and TEM measurements in different selective solvent.

To investigate thoroughly the self assembly of this amphiphilic copolymer, measurements of transmission electron microscopy and nuclear magnetic resonance were carried out on the two solutions of water and toluene and on a solution of chloroform. This last sample appears as a clear solution indicating full solvatation of both blocks. For TEM measurement a drop of the polymer solution was placed on a perforated carbon grid and solvent was evaporated under a hood at room temperature. For NMR measurements, the appropriate samples were prepared using deuterated solvent.

^{1}H NMR spectra is shown in Figure 36. Each block has specific signals, namely from 6.5 to 7 ppm for PS while PDMA is around 2.8 ppm. In fact solution NMR is optimized for fast moving molecules, and reduced mobility produces a dipolar line broadening due to H-H interactions. At the limit of slow mobility, solid-like fractions are not detected because of extremely low T_2 relaxation time[91]. The presence or absence of peaks in the spectra can thus be interpreted as a function of mobility.

The electron microscope was able to identify some structures compatible with the typical phases of a block copolymer.

In the solution prepared from organic solvent (d-toluene) the styrenic block is solvated and provides full signal intensity while the PDMA presents a

line broadening of the methyls of dimethylacrilamide corresponding to reduced but not solid like mobility. TEM measurements detected elongated macromolecular structures. The copolymer is organized in wormlike constructing assembled "tripod", which extends for several microns. The PDMA phase is partially wetted by the solvent, which acts as a plastifier.

The peaks of the styrenic block disappear in water, meaning the hydrophobic block is behaving as a rigid solid. This indicates the styrenic blocks are clustering together, excluding solvent and resulting in a very low mobility, as expected for bulk styrene under the T_g. On the other side, a quite regular distribution can be visualized in the TEM image shown in Figure 36, that displays black spots, somewhat regularly arranged in a pseudohexagonal fashion with a center to center distance of 60-70 nm. This is attributed to polystyrene cores whilst the PDMA shells are no longer well organized as a consequence of the water evaporation. It should be noted that no contrast reagents were employed for the acquisition of the image, as such the contrast is connected with the higher density of the closely packed polystyrene cores with respect to the swelled and disorganized PDMA shells.

A core diameter of 15-20 nm and a diameter of whole micelle of about 60-70 nm were estimated by TEM image reported in Figure 36. The different diameter obtained by TEM and DLS techniques is not surprising. Indeed, considering the swelled form of the external PDMA shell of micelles, it is simple to image that the size measured by TEM image is underestimated as a consequence of the water evaporation: the deposited micelles can partially superimpose the external shells. On the other hand, DLS technique probes a hydrodynamic diameter which can be quantitatively different from the actual size.

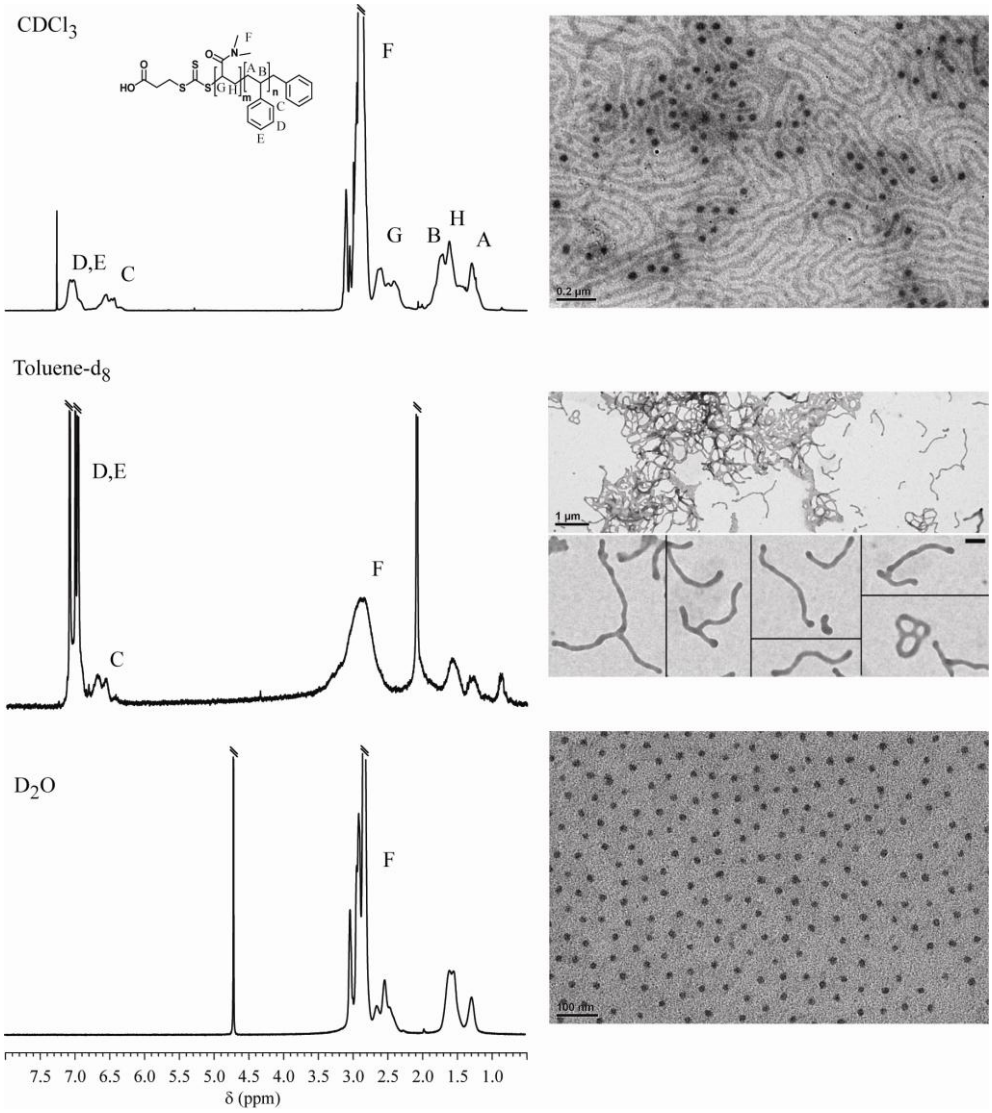

Figure 36. ^{1}H NMR and TEM measurements of $PS_{105}PDMA_{817}$ self assembly in different solvent.

4.2.2. Fluorescence spectroscopy

TEM and NMR give clear indication of the solid-state nature of the PS core of the micelles, yet no quantitative information can be obtained regarding to

the local viscosity and the stiffness of the cores. Also, neither NMR nor TEM or DLS can give any insight about the dynamics of the self assembly process in terms of the minimum amount of water to be added to the DMF solution, nor the time required for the self assembly process to be complete. This information are of crucial importance in practical applications connected with the formulation of drug constructs. In order to clarify these questions, a self-assembly experiment was performed in presence of a small amount of AzeNaph1 in the starting DMF solution containing the copolymer.

The system was prepared as follows. 1 ml of DMF, 20 mg of PS-b-PDMA and 96 μl of solution of AzeNaph1 (3.77 M) were mixed. The photoluminescence lifetime was measured on the initial solution, and after subsequent addition of 100 μl of water until 5 ml. The solution was maintained constantly under magnetic stirring. The self-assembly process, induced by water dropping from 5 to 500 volume percentage (vol %), was investigated by acquiring the AzeNaph1 time decay profile. In detail, after the addition of a certain amount of water, a fixed time (3 min) was kept before carrying out measurements in order to be sure that the self-assembly process was completed. As mentioned, the molecular rotor is completely insoluble in water, as such, during the self-assembly process, it gets embedded in the micelles.

In Figure 37 the AzeNaph1 time decay profile in DMF solution containing the copolymer before starting to add water (black curve) and after water dropping (20% vol and 500% vol, blue and orange curves, respectively) is shown. It is evident that the decay profile of molecular rotor in the starting sample and in the sample with 500% vol water are very different from each other. Indeed, in the latter case, the process is dominated by a decay profile with a slower τ_f (indicated hereafter as τ_{slow}) if compared with the faster τ_f (τ_{fast}) associated with the starting sample. In particular, it was estimated that $\tau_{slow} \sim 5.8 \pm 0.4$ and $\tau_{fast} \leq 1$ ns.

For the reasons discussed above, τ_{fast} can be associated to the low microviscosity probed by AzeNaph1 dispersed in the medium in form of a

disorganized random coil fraction of the polymer chains. On the other hand, considering the findings obtained by TEM and NMR investigations, τ_{slow} can be attributed to the fraction of molecular rotors embedded in the rigid core of micelles. Because the time decay profiles between the sample with 500% vol water and PS bulk (compare Figure 34a and Figure 37) are the same, the PS core of the micelles has the same microviscosity as bulk PS. Moreover , notwithstanding the reduced nano-metric dimension of the core (only 15-20 nm), the PS structural properties in terms of viscosity are comparable to those of bulk system.

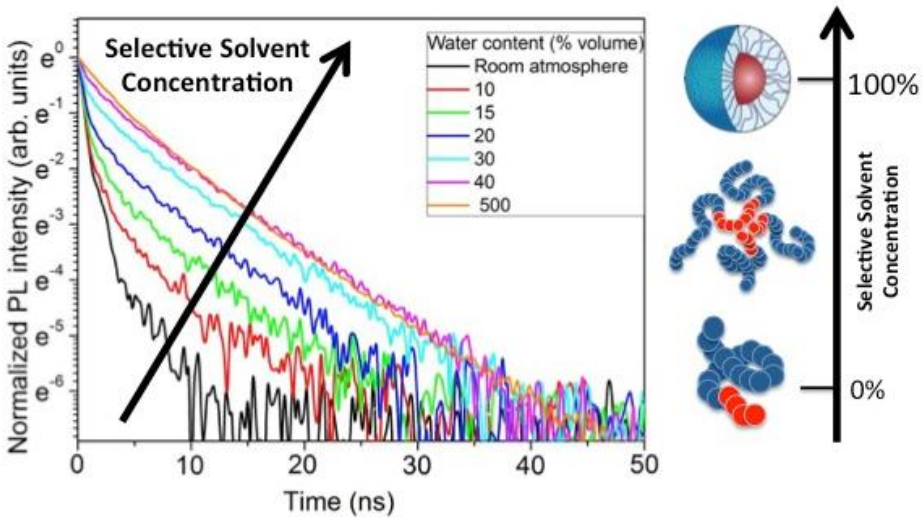

Figure 37. Time decay profile of AzeNaph1 in DMF solution containing the PS-b-PDMA before water dropping (black curve) and after water dropping.

This finding apparently disagrees with the work of Priestley et al., in which they reported that the T_g of PS nanoparticles decreases on decreasing of particles size under 200 nm. However, our results can be explained by the consideration that the swelled PDMA external shell of the micelles induces a "hydrostatic" pressure on the core surface. This pressure can be considered as the

"hard confinement", discussed by Wilhelm et al.[80], which contrasts the nano-metric effects on T_g of PS core. To the best of our knowledge, this is the first non-invasive in situ characterization of micelles core viscosity to date. The emission lifetimes of DMF-dissolved and micelles core-embedded AzeNaph1 is so different that it is possible to measure the molar fraction of polymer chains assuming micelles conformation as function of the amount of water added.

Some of the profiles acquired for different amount of dropped water are shown in Figure 38a, where one can see a gradual change in the relative contribute of two exponentials from the starting DMF solution containing the copolymer without water and the sample with 500% vol water. For a more quantitative investigation, is performed a population analysis based on equation:

$$\frac{PL(t)}{PL(0)} = A_g e^{-\frac{t}{\tau_{slow}}} + \left(1 - A_g\right) e^{-\frac{t}{\tau_{fast}}} \qquad (9)$$

where the prefactors of the exponential terms describe the fraction of population with t_{fast} and t_{slow}. The A_g prefactor as a function of the water addicted is reported in Figure 38. A_g represents the relative population of AzeNaph1 in the core of micelles and hence the plot in figure can be interpreted as growth curve of the micelles formation. The plot is closely similar to sigmoid function of a titration curve. The plot shows that the large amount of excess water commonly employed in the experimental protocols is not necessary as the vast majority of the polymer chains are already self assembled when the water content is around 60% of that of DMF. Further addition of water does not change the sample population.

As shown in Figure 38b the process of self-assembly is surprisingly fast, the decay profile is measured two minutes after the water addition was identical to those measured after 10, 100 or even 1000 minutes and independent of the amount of water added. This finding is relevant, in fact a number of literature

procedure prescribe very long “resting” time for the copolymer/water suspension prior to further characterization/use of the micelles.

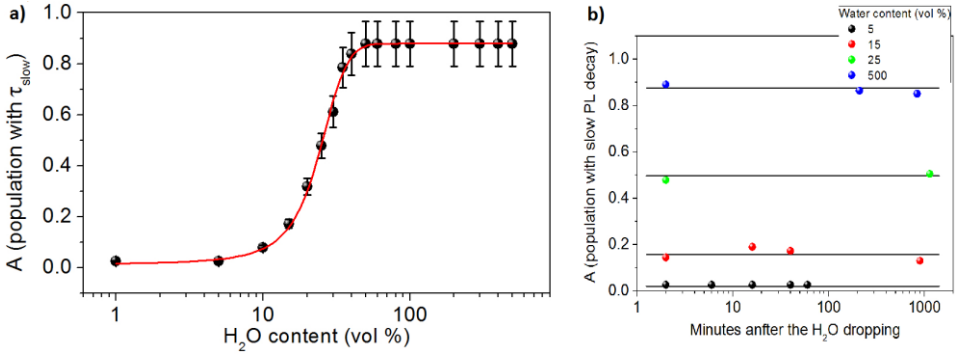

Figure 38. a) Relative population with t_{slow} , obtained by fitting the time decay profiles of AzeNaph1 to Eq. 1, as a function of the amount H_2O addicted. The red line is only a guide for the eye. b) Relative population with t_{slow} , obtained by fitting the time decay profiles of AzeNaph1, as a function of elapsed time after water dropping.

4.2.3. Conclusion of characterization

Analysis DLS, TEM and NMR show that the self-assembly of $PS_{105}PDMA_{817}$ in water produces spherical core-shell nanoparticles. Moreover, the use of a properly designed new luminescent molecular rotor enables the in situ, fast monitoring of core-shell micelles assembly. The analysis is based on the very sensitive response of the molecular rotor emission lifetime to the microviscosity of the medium in which it is dissolved/dispersed. This non invasive, straightforward and fast technique shows that. The core of PS-b-PDMA hairy micelles is as dense and rigid at ambient temperature as bulk polystyrene; it is possible to readily titrate the amount of organized versus random coil copolymer chains as a function of the amount of water by means of a simple

population analysis; the process of self assembly of the micelles by nonsolvent addition is very fast as it is complete after less than 2 minutes.

4.3. Self assembly of $PS_{62}PDMA_{10}$

5 mg of copolymer $PS_{62}PDMA_{10}$ (PSPDMA_3, Table 2, cap 3) was dissolved in 1 ml of dimethylformamide and 5 ml of deionized water were added drop by drop under stirring with a rate of 2 ml h^{-1}, with automatic syringe pump. The solution was stirred for two days and the aspect was turbid. For lifetime measurement the sample was prepared with the same procedure as before but starting from in the DMF with a 10^{-3} molar concentration of AzeNaph1 dye**.** For hydrolysing the nanoparticles, 0.1 ml of HCl solution (0.5 M) was added to 1 ml of the above described solution. This preparation was also stirred for 2 day before measurement.

The measurement of hydrodynamic radius of nanoparticles was carried out with dynamic light scattering. Figure 39 shows the size distribution of a typical nanoparticle dispersion in water. The peak of the hydrodynamic radius is at 146 nm resulting in an average a diameter of 292 nm, with very narrow distribution.

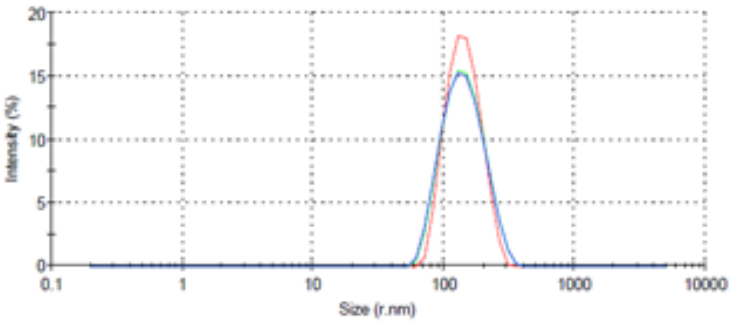

Figure 39. DLS measurement of nanoparticels.

4.3.1. TEM

TEM was used to observe the morphology of the self-assembly. Specimens were prepared by slow (approximately 1 hour) evaporation of a drop of diluted solution deposited onto a collodion-coated carbon mesh grid.

The TEM images of copolymer morphology are shown in in Figure 40. The presence of spherical particles with a diameter of about 100–200 nm is immediately seen. The size is smaller than the hydrodynamic radius Rh measured in DLS, suggesting the particles are well hydrated in water and instead undergo some shrinking in the high vacuum conditions necessary for TEM. A similar, but more pronounced behavior demonstrated by PSPDMA_13 particles (90 nm in water, 60 in TEM conditions) supports this view.

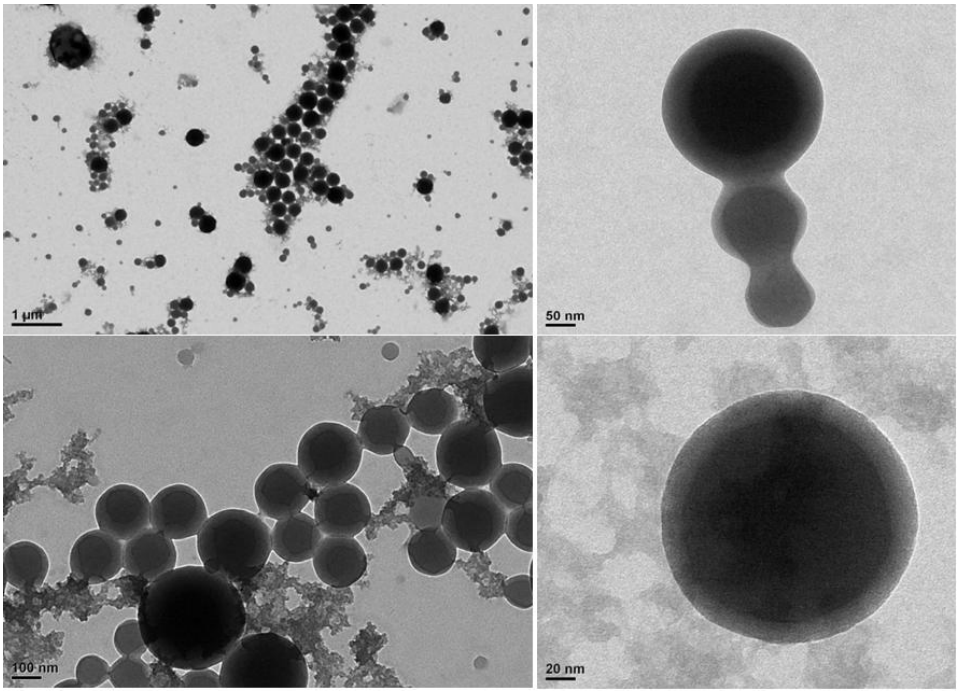

Figure 40. TEM images at different scales, as indicated in the bottom left corner.

4.3.2. SEM

As shown in Figure 41, SEM images confirmed the morphology of the self-assembly of the copolymer in a sphere with diameter similar to TEM images.

SEM has a reduced resolution, and is thus not eligible as a tool for investigating any internal structure of the particles. Compared to the flatness of the TEM images, SEM offers a more three dimensional view. Figure 41 supports the identification of the nanoassembies as spheres with an high degree of shape stability, as compared to the flat TEM images of Figure 40 that could also indicate flattened spheres or disc like structures.

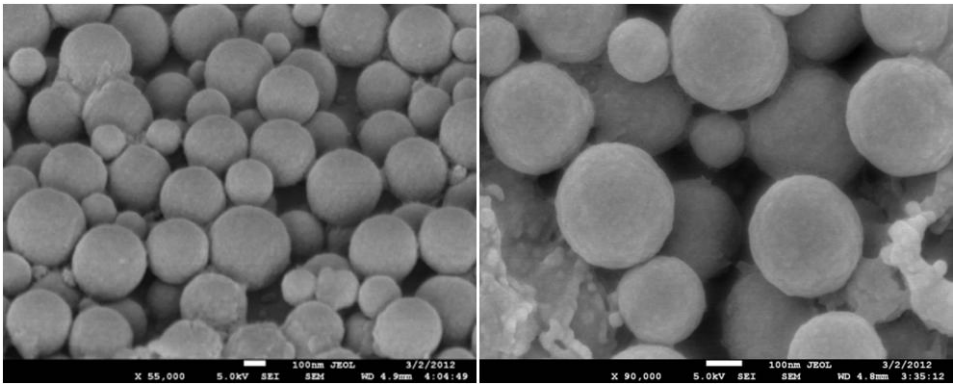

Figure 41. SEM images of nanoparticles of copolymer $PS_{62}PDMA_{10}$.

4.3.3. Lifetime measurements

Photoluminescence spectroscopy was also applied to the study of the equilibrium structures formed by PSPDMA_3 in conditions of high water content. In Figure 42 the lifetime of the molecular rotor inside for copolymer (red line) is shown and compared with the lifetime in solution (black line) and in bulk (blue line). From these measurements it can be deduced that the PS block of spheres is organized in a phase with an increased mobility in respect of the bulk.

This can be due to the thinness of such phases, consequence of the low molecular weight of the PS block, as implied for the case of phase separation of short block copolymers.

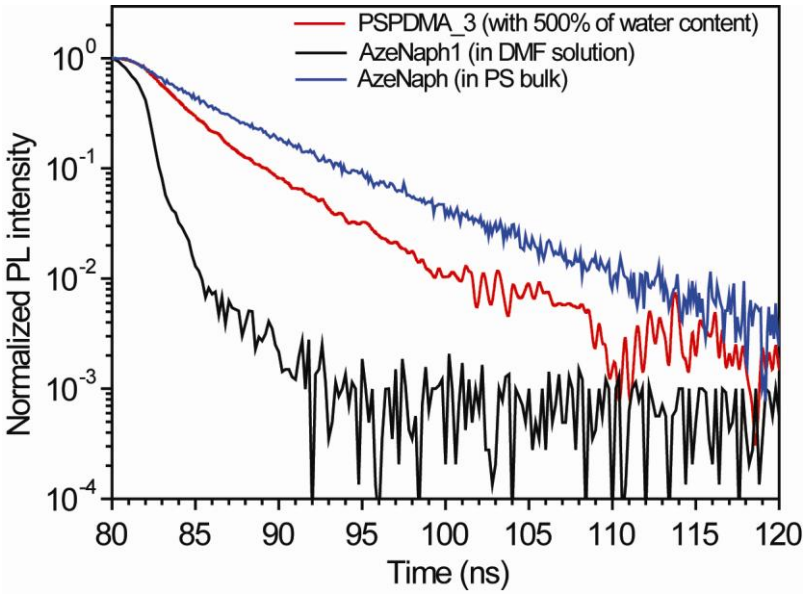

Figure 42. Time decay profile of AzeNaph1 in DMF solution containing the PS-b-PDMA before water dropping (black curve) and after water dropping.

4.3.4. AFM

AFM imaging and force spectroscopy were carried out with a JPK NanoWizard (JPK Instruments, Berlin, Germany, with closed loop scanner) equipped with JPK controller and software, using the silicon cantilevers with a resonance frequency of 70 kHz and a nominal spring constant of 2 N m^{-1} (OMCL-AC240TS, Olympus, Tokyo, Japan). Spring constants of cantilevers were determined using the thermal noise method.[92]

For the initial characterization, particles that were deposited from H_2O solution onto freshly cleaved mica were imaged using AFM in intermittent

contact mode under ambient conditions. Typical AFM height images are shown in Figure 43A, D. From the fitted data of individual particles, it can be seen that the particles are indeed described as a spherical cap. In Figure 43 C the histogram of the observed radii of the spherical caps is shown. The average calculated value was 267 ± 30 nm.

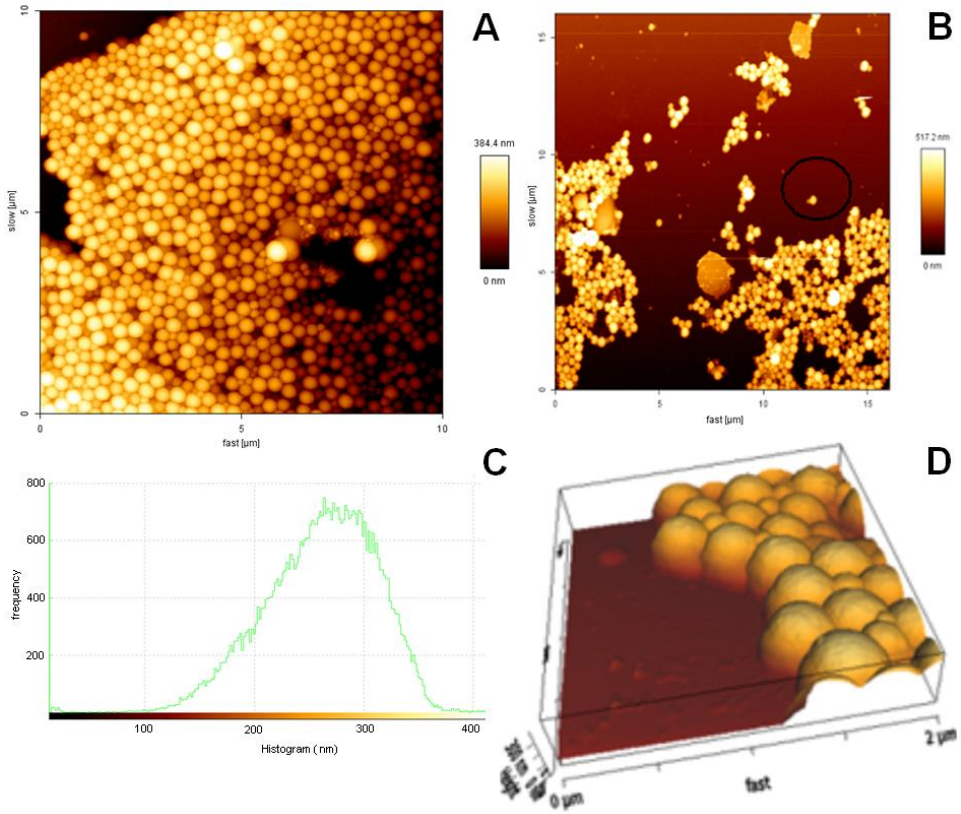

Figure 43. A, TM-AFM image (10 µm x 10 µm) of block copolymer nanoparticles made from PS_{62}-b-$PDMA_{10}$ deposited on mica under ambient conditions. B, AFM image of sample, the black circle shows the particle studied by force spectroscopy. C, Histogram of the observed radii of the spherical caps for PS_{62}-b-$PDMA_{10}$ 267 ± 30 nm. D, 3D-AFM image of the PS_{62}-b-$PDMA_{10}$ nanoparticules.

Force spectroscopy were performed in contact mode by calculating a spring constant = 1.42 N / m. It was possible, by micromanipulation, to insulate a single sphere for detailed study, as shown in Figure 43 B (black circle). The force of the cantilever was increased in a gradual manner as indicated in the following . Relative setpoint (nN): 18.8, 31.3, 62.6, 125.2, 187.8, 250.4, 313.0, 431.9, 494.5.

For each set force a point was measured in the center of the particle and one on the substrate, which was used as a reference. After each force spectroscopy measurement, a shift occurred in the position of the particle. In other words, the nanostructure moved as a single body under the effect of the probing force, Thus, the system was reset to intermittent mode in order to recalibrate the tip over the center of the particle. The particles were not fixed on the surface not to vary the mechanical properties.

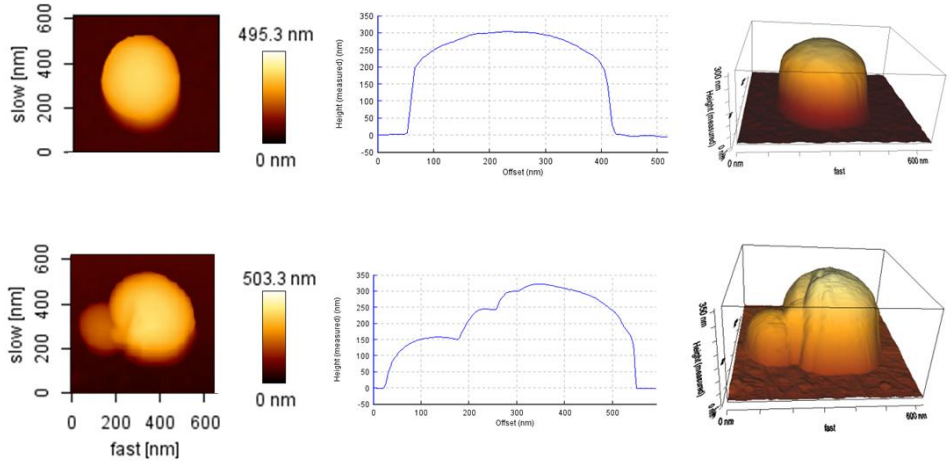

Figure 44. AFM image of sphere studied by force spectroscopy with relative set point = 494 nN . Image of the cross section and 3D image. relative set point = 18.8 nN .

In Figure 44 a typical particle is analyzed by force spectroscopy with a force equal to 18.8 nN. The cross section diameter of the particle and the 3D representation: the particle both indicate a very clearly defined spherical shape.

Similar images were obtained with most of the forces Upon increasing the strength of to 494 nN indentation, we instead produced a breakdown of the particle, as can be seen from the cross-sectional diameter (Figure 44). This image also confirms the view of a solid, structure, and excludes the nanovescivle form.

4.3.5. FIB enhanced SEM experiments

Further investigation of the internal structure was performed by cutting particles with a focused ion beam (FIB). For sample preparation, a drop of this particle suspension was cast on a Si wafer and dried over night. The Si wafer was glued to an aluminium stub using a double-sided adhesive carbon tape.

The sample was mounted on the stage of the FIB and the sample chamber was evacuated to a working pressure of about $7*10^{-5}$ mbar at room temperature. First the SEM of the dual beam instrument was used to obtain overview images of the sample and to locate single spheres for further analysis (Figure 45, A). Along the rim of the dried droplet we observed a ring-like structure which might have resulted from an organic part formed by a coalescence of the nanoparticles (Figure 45, B) and was deposited due to the so called “coffee stain effect”.

The sample stage was then tilted by 52 degrees to cut single particles with the focused ion beam from the top while observing the cross-section from the exposedside Figure 45 C shows the top view of the cut area imaged using the ion beam, while Figure 45 D is an SEM image of the finished cut. There is no indication of visible phase separation. For further cuts with the FIB, a thin layer (~100 nm thickness) of platinum was deposited over the particle using beam-assisted Pt deposition (Figure 46 A). This allows cutting of the sphere without removing the top layers and leads to smoother cross-sections. Again we could not see any difference between the interior and the exterior of the sphere (Figure 46 B).

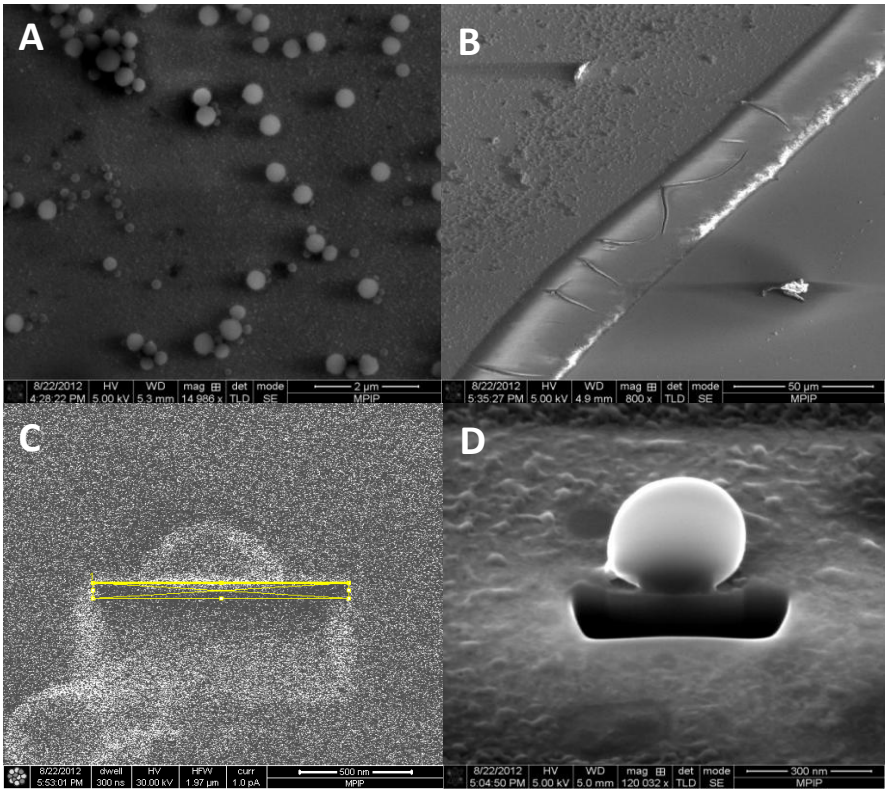

Figure 45. SEM images of PSPDMA_3: A, overview of particles; B detail of the rim of the dried droplet; C, the top view of the cut area imaged using the ion beam; D, freshly exposed side of the cleaved particle.

The same analysis was performed on a third particle (Figure 46 C, D), with the same result. Therefore, it can be noted that the analysis technique using FIB / SEM does not permit us to see any phase difference of the two blocks of PS and PDMA inside the nanoparticles. This does not necessarily indicates a single phase. Actually, considering the length of the polymer blocks and the resolution of SEM, phase separation can simply be at a scale not detectable with this technique.

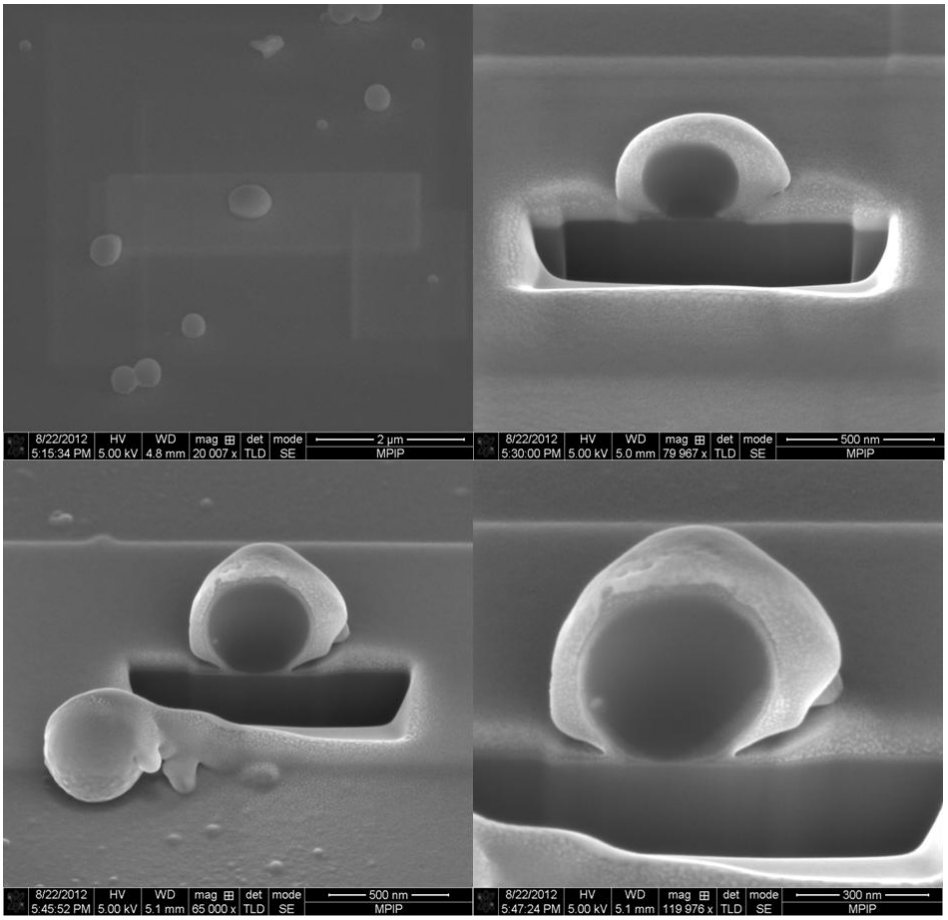

Figure 46. SEM images of PSPDMA nanoparticles covered with a Pt layer, and then cut with FIB.

4.3.6. Hydrolysis

For an indirect investigation of the real morphology of these nanoparticles, and for a preliminary study on possible applications like drug delivery, the hydrolysis of PDMA was performed, ideally converting the PDMA block to polyacrylic acid (PAA). The much higher hydrophilicity of PAA is expected to increase phase segregation favouring forms of organization that maximize the solvation of the water soluble block. The analysis of the new shape can

contribute to the determination of the initial internal structure. The particles of PS-PDMA were hydrolysed by adding a solution of HCl which reacts with acrylamide units, and namely with the side chain, as indicated in Scheme 9 (chapter 3).

Hydrolysis was performed by adding 0.1 ml of HCl solution (0.5 M) to 1 ml of solution prepared as above and stirred for 1 day before measurement. These conditions ensure excess acid relative to the PDMA functional groups. As can be seen in the SEM images around each particle of the polymeric material a halo is produced (see Figure 47). On the surface of the nano particles the formation of small partially protruding spheres is observed. The size of those spheres can't be measured precisely at the SEM resolution, but is 1-2 orders of magnitude smaller than the superstructures formed by the pristine polymer. This is compatible with single AB 55 core-shell particles made up a core of polystyrene (not soluble in the acid solution) and a shell of poly acrylic acid. The halo is then attributed to particles detached from the original superstructure. While particle size is generally reduced, some particles look more distrupted than the others. While the process of hydrolisys and formation of smaller particles is ubiquitous, the actual disintegration of the macrostructure is more random. Figure 48 shows the TEM measurements performed on hydrolyzed nanoparticles. Also in this case it is possible to delineate the presence of small agglomerates forming from the surface that were not detected in previous TEM measurements. The absence of clearly defined halos around the dissolving particles probably depends on less macroscopic mechanical vibrations and thus no crumbling of the now fragile structures.

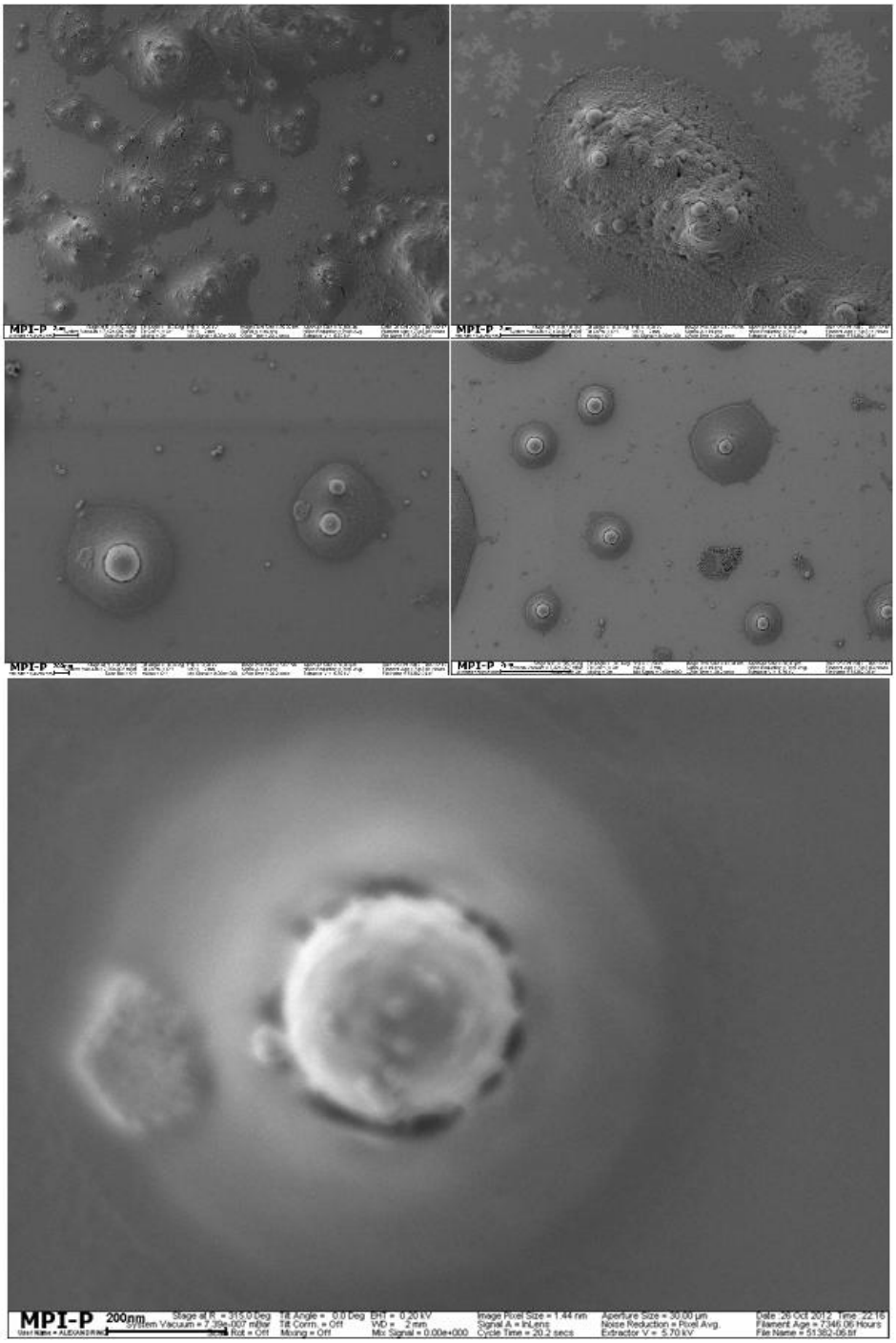

Figure 47. SEM images of nanoparticles after hydrolysis.

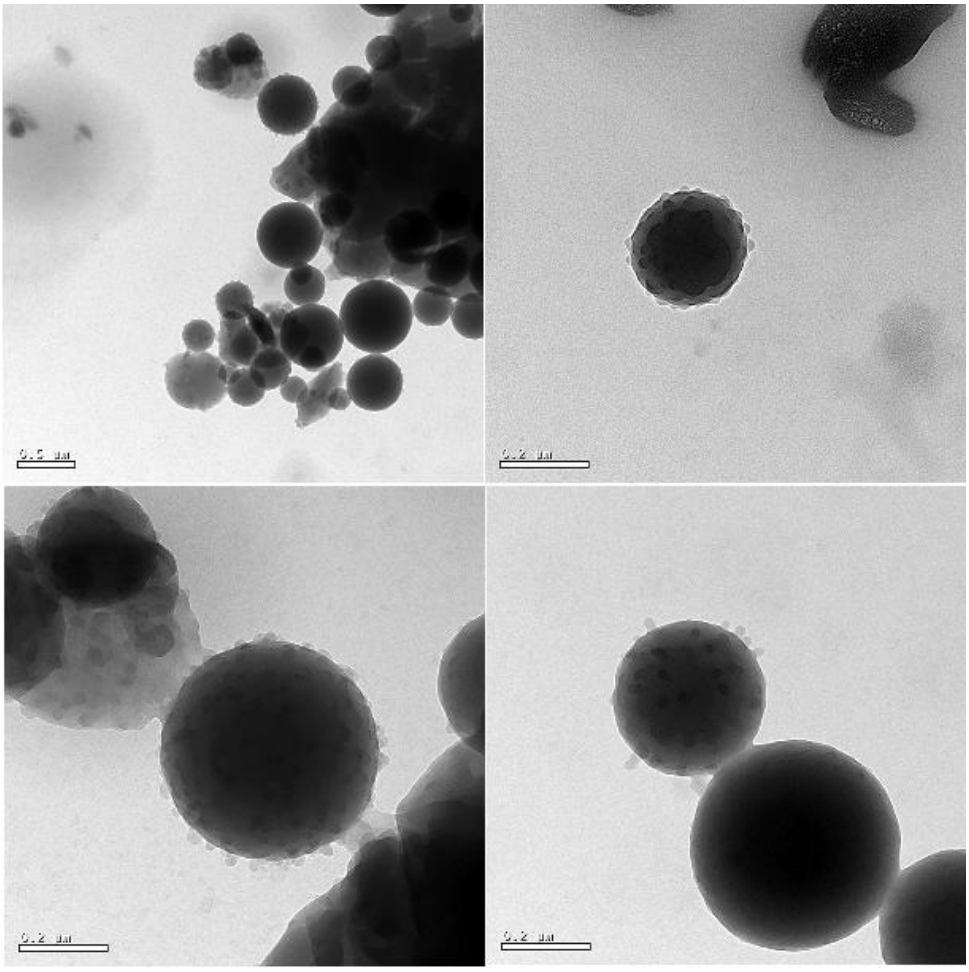

Figure 48. TEM images of nanoparticles after hydrolysis.

4.3.7. Conclusion of characterization

DLS SEM, TEM and AFM analyses, show that the block copolymer $PS_{62}PDMA_{10}$ (PSPDMA_3) self assembles in water (selective solvent for the poly dimethyl acrylamide) creating a spherical structure with a diameter between 200 and 300 nm. SEM and AFM demonstrate hardness and shape stability of those structures, even out of the water environment. While TEM is unable to

detect directly an internal structure, the values of χN for this polymer predict phase separation, suggesting a more usually connected to a hierarchical structure. Measurements of photoluminescence lifetime indicated that phase separation within the particles does not produce a rigid part of similar to bulk polystyrene. This explains the difference between this case and AB48: in that case, there was a very sharp difference in density between the core and shell, resulting in detection of the two phases without staining which is instead not detected here. Moreover, by their whole appearance and cutting the particle through the FIB there is no apparent internal structure due to separation of the phases of the two different polymers (PS and PDMA). Any phase separation is then predicted to be at lower scale than SEM resolution.

One possible interpretation of the data collected from several techniques is that self-assembly of the sample $PS_{62}PDMA_{10}$ produces a complex hierarchical nanostructure spanning hundreds of nanometers, formed in turn by smaller (10-20 nm) micelles with a PS core and a thin shell of PDMA. These micelles form a spherical granular structure to minimize the energy (see Scheme 10). This structuration can't be detected directly, because PL spectroscopy demonstrates the PS block is not in a bulk-like state as in the previously dscribed AB48.

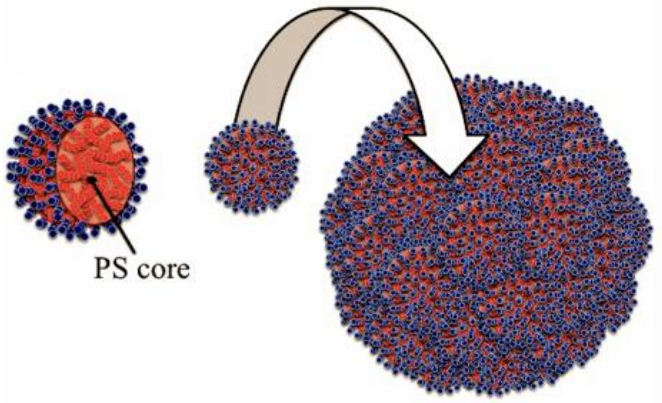

Scheme 10. Schematic reconstruction of the nanoparticle after self-assembly in water of the copolymer $PS_{62}PDMA_{10}$.

Thus, the difference of density between the PDMA and PS phase is not sufficient to provide TEM contrast. But this complex structure is demonstrated by the detailed study of the breakdown of the structure after hydrolysing PDMA in PAA and increasing the hydrophilicity of the shell of the micelles. Since acrylic acid has a higher hydrophilicity than dimethyl acrylamide, the particles have no more an energy advantage to form a sphere granulate. Also by means of force spectroscopy is shown that the particles are an agglomerated structures of smaller objects because, with the increase of the force of indentation, a collapse of a part of the sphere occurred rather than a real breakdown.

Chapter 5. Synthesis of the block copolymers for Quasi Solid-State Dye-Sensitized Solar Cells

In this chapter I will present amphiphilic block copolymer as polymer gel for the electrolyte in the dye-sensitized solar cells (DSSC). The synthesis of the polymer is performed through RAFT polymerization starting from commercial polyethyleneoxide. Then I will report the first applcation of a PS-b-PEO block-copolymer in I^-/I^{3-} electrolyte in combination with N719 as a sensitizer in a DSC device, affording efficiencies up to 6.9%, to be compared with an efficiency of 7.3% obtained in similar conditions with a liquid electrolyte[93].

The final goal of this project is overcome one important drawback of the conventional Dye-Sensitized Solar Cells (DSSC) configuration, consisting in the evaporation or leakage of toxic solvents used as liquid electrolyte, leakages are particularly detrimental since they cause corrosion of the sealing materials and metals constituting the cell.

5.1. Introduction

Dye-sensitized solar cells (DSSCs) represent one of the emerging photovoltaic (PV) technologies showing an optimal trade-off between high-conversion efficiency and low-cost manufacturing.[94,95] Currently inorganic solar cells are more efficient, but the advantages of organic cells are many: low cost and ease of production, performance increases with temperature, bifacial configuration advantage for diffuse light, transparency for power windows and

the color can be varied by selection of dye, visible PV-cells based on near-IR sensitizers are feasible.

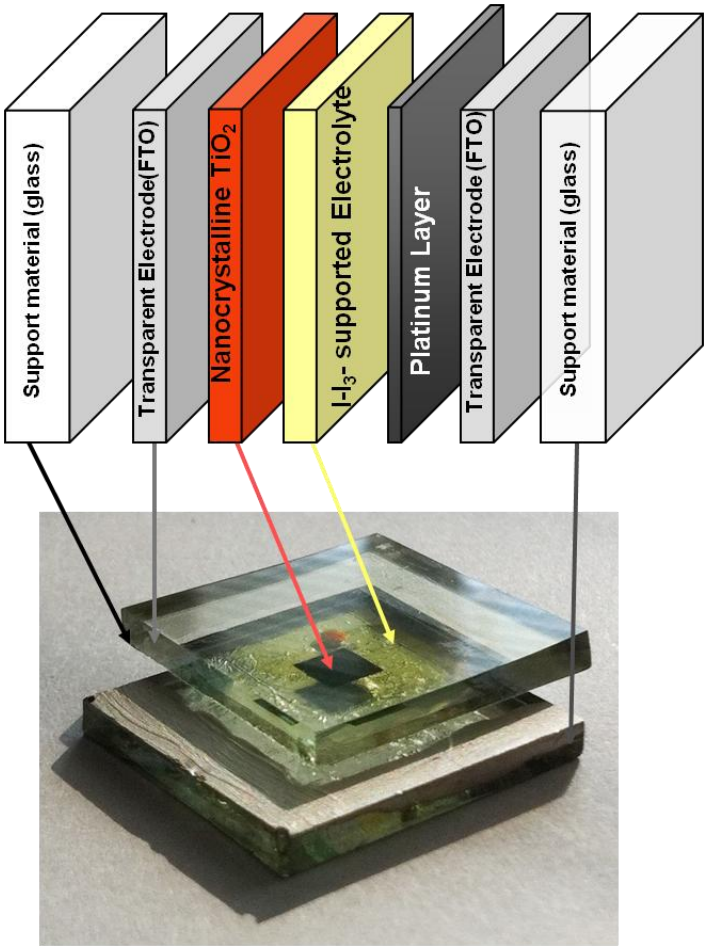

Figure 49. Example of a experimental DSSC.

DSSC have become a credible alternative to solid-state p–n junction devices and they were inspired by the natural photosynthesis. Research and development of efficient, cheap, and stable thin-film PV devices is increasingly important.[96,97] The cells are a combination of more materials and principally composed of five components, as shown in Figure 49. A mechanical support

coated with transparent conductive oxides (ITO or FTO); a semiconductor film, usually TiO_2; a dye sensitizer adsorbed onto the semiconductor surface; an electrolyte containing a redox mediator (usually I^-/I^{3-} redox couple); a counter electrode capable of regenerating the redox mediator.

The operational principle of the cell requires that upon illumination the dye molecule absorbs light photoexciting an electron from the HOMO to the LUMO level, which is then injected into the conduction band of the oxide. The dye is subsequently reduced to its initial state by the donation of an electron from the electrolyte, usually an organic solvent containing redox system, such as the already mentioned iodide/triiodide couple. The regeneration of the sensitizer by the electrolyte is crucial in order to avoid undesired processes such as the back-transfer of the electron from the titanium dioxide to the dye or undesired side reactions. On the other side the electrolyte is regenerated by the reduction at the counter electrode. The circuit being completed via electron migration through the external load. The voltage generated under illumination corresponds to the difference between the Fermi level of the electron in the solid and the redox potential of the electrolyte. Overall the device generates electric power from light without undergoing permanent chemical transformations.

A crucial role is the morphology of the semiconductor which has to be porous and endowed with a high surface area. In fact a dye sensitized nanocrystaline film generates over 1000 times more photocurrent then a single crystal electrode.

The dye is the real motor of the cell, different types of systems can be used, ranging from all organic molecules to metal complexes. In order to optimize the efficiencies of the cell, the sensitizer should satisfy a number of essential requirements. First of all it should strongly absorb solar radiation with absorption bands in the visible or near-IR region, preferably covering a broad range of wavelengths. Furthermore the sensitizers should bind strongly to the TiO_2 by means of an anchoring group, typically a carboxylic or phosphonic acid,

possibly located in the high charge density of the excited state of the dye. This ensures efficient electron injection into the TiO_2 conducting band and prevents gradual leaching by the electrolyte. The electron transfer from the excited state of the dye to the TiO_2 must also be rapid in comparison to the decay to the ground state. Additionally the LUMO of the dye must be sufficiently high in energy for efficient charge injection into the TiO_2, while the HOMO must be sufficiently low in energy for efficient regeneration of the oxidized dye by the hole-transport material.

All these requirements can be successfully satisfied by careful design of the molecules and tailored according to needs via organic synthesis. The most famous example of dyes for DSSCs are metal complexes. The optimization of the dye metal complex component of the cell has been made through systematic variation of the ligand nature, metal, and introducing different types of substituent on the metal ligand. This systematic study has resulted in the development of mononuclear and polynuclear dyes based on metals such as Ru(II), Os(II), Pt(II), Re(I), Cu(I), and Fe(II). By tuning the ligand orbitals, via substitution of the electron acceptor groups on the dye molecule, it is possible to adjust the LUMO level of the system. The prototypical sensitizer is the Ru(II) complex bis(2,2'-bipyridyl-4,4'-dicarboxylate)ruthenium(II) (N719). N719 based DSC have reached power conversion efficiencies exceeding 11%.[98] The best photovoltaic performances up to date in terms of efficiencies and long term stability has so far been achieved with polypyridyl complexes of ruthenium in which have been used two ligands L = 4,40-dicarboxy-2,20-bipyridine and thiocyanate ligands.

One important drawback of the conventional DSSC configuration consists in the use of a liquid electrolyte based on the I^-/I^{3-} redox couple, which causes evaporation or leakage of toxic solvents and corrosiveness of the iodide/triiodide couple toward sealing materials and metals, such as Ag and counterelectrode Pt.[99] This results in a less robust sealing and reduced long-term stability. As a matter

of fact, the use of liquid electrolyte is considered to be the most important restriction for the scale up of DSSC technology. On the other hand the use of the iodide/triiodide couple allows for higher efficiencies thanks to a favorable penetration into the mesoporous TiO_2 film and fast dye regeneration. Therefore, it would be of crucial importance for the market to replace the conventional liquid electrolyte bypassing the issues linked to the presence of solvents but keeping the advantages of the iodide/triiodide redox system. Over the past years a number of approaches have been investigated to replace liquid components by solid-state and quasi solid-state electrolytes,[100,101] such as hole transport materials, ionic liquids,[102] or solid-state composite electrolytes. Although a certified 6.08% record value has been recently reported for a solid-state DSSC (ssDSSC) using the molecular 2,2',7,7'-tetrakis(N,N-dimethoxyphenylamine)-9,9'-spirobifluorene (spiro-MeOTAD) hole-transporting material,[103] the performances of ssDSSC are much lower than those based on the liquid electrolyte, with the best power conversion efficiencies approaching 5%. This is mainly due to poor ion diffusion and conductivity properties.

One simple approach to avoid leakage and evaporation of solvents from the electrolyte consists in using a dispersion in a polymeric matrix.[104,105] In these cases the conventional electrolyte is still present in its original form but is converted in a quasi solid-state material. The advantage of using polymer electrolyte is the higher conductivity and pore filling properties compared to other ssDSC components such as spiro-MeOTAD. In a polymer electrolyte, generally prepared by dissolving the inorganic and organic salts in a proper polymer matrix, the liquid electrolyte is trapped in a polymer cage forming a three-dimensional network, where the ions are free to move as in the liquid phase. A large number of polymer composites have been tested. Among the others, poly(ethylene oxide) (PEO) polymers have been commonly used as host materials for ssDSC, thanks to the coordinating properties of the polyether chain to the lithium or sodium cations present in the electrolyte mixture.

Shu Yin et al.[106] have obtained good results (6.1%) using the blend polymer PEO/PAA, with good structural stability compared to ssDSSC.

An electrolyte based on a blend of polyacrylic acid and polyethyleneglycol, obtained by radical polymerization of acrylic acid in presence of PEG chains, with NaI/I_2 was able to afford a remarkable 6.1% efficiency.[107] By using the same methodology and a metal-free organic sensitizer an efficiency of 6.8% has been obtained.[108]

On the other hand the problem of these systems is the coexistence of two different phases that are thermodynamically unstable, with strong tendency to phase segregate with time and especially at the high operating temperatures of the cell. However, block copolymers are organized by self assembly in stable nanometric ordered structures (for example: cubic, lamellar, hexagonal…). Furthermore the nanometric confinement can prevent crystallization of PEO. De Paoli and co-workers have pioneered the use of PEO-based copolymers with a poly(epichlorohydrin-co-ethylene)oxide polymer filled with NaI/I_2 as an electrolyte, the authors report conversion efficiencies of 10-4%, which were later improved to 1.6% by using N719 as the sensitizer.[109]

Therefore, the advantage of using block-copolymers, obtained by RAFT polymerization, over conventional polymers such as PEO (polyethyleneoxide), random copolymers, or polymer blends, is the possibility to control the morphology of the polymer gel by varying the ratio between PEO and the hydrophobic blocks. Furthermore a large variety of monomers can be used, providing gels characterized by different physico-chemical and mechanical properties, as an example Tg can be finely tuned. On the basis of this complex and rich morphological variety, block-copolymers represent a versatile class of templates for nanoarchitecture construction.

5.2. Synthesis and characterization of triblock copolymers

The copolymer PS-b-PEO-b-PS was synthesized in two steps. First, esterification was carried out between commercial available polyethyleneoxides and RAFT agent, S-1-Dodecyl-S'-(α,α′-dimethyl-α′′-acetic acid) trithiocarbonate, then the macrotransfer agent was used in the polymerization of styrene. The procedure used is reported in Scheme 11. The variation of the polymerization time leads to copolymers with different length of the second block.

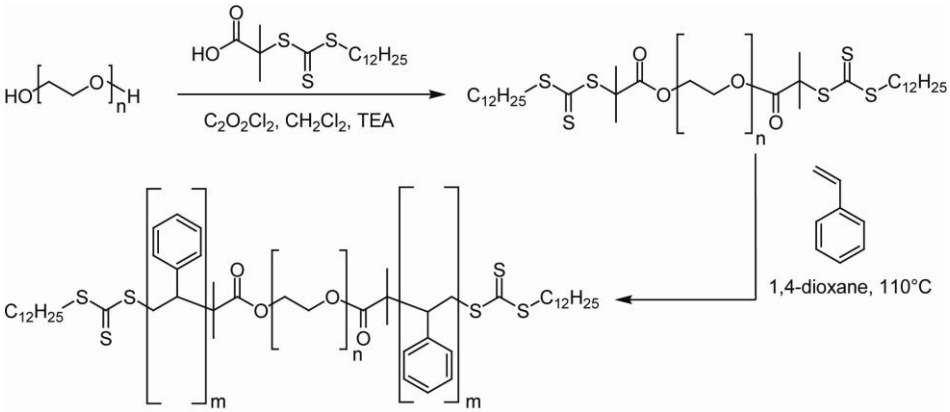

Scheme 11. Synthesis of triblock PS-PEO-PS.

5.2.1. Synthesis DDAT-PEO-DDAT

In a 50 ml Schlenk tube with a magnetic stirring bar, oxalyl chloride (0.291 g, 2.3 mmol) and DDAT (0.759 g, 2.1 mmol) were dissolved in dry CH_2Cl_2 (20 mL) and stirred at room temperature until gas evolution ends. After 5 h, the solvent was removed under vacuum. The residue was dissolved in 20 ml anhydrous CH_2Cl_2 and added via cannula under nitrogen to freshly distilled PEO

(5.00 g, 0.83 mol). Freshly distilled triethylamine (0.25 mL) in dry CH_2Cl_2 (10 mL) was added to the stirred solution. The reaction mixture was stirred under nitrogen atmosphere for 18 h. The formation of a precipitate was observed. The solid was filtered and cold Et_2O was added to organic solution until a precipitate was formed. The solid was collected and the solution was precipitated three times and dried under vacuum overnight. The product was obtained as a pale yellow solid (5.1 g, yield: 89%). ^{1}H NMR (500 MHz, CDCl3) δ (ppm): 0.85 (t, 6H, -$CH_2C\mathbf{H_3}$ of the $C_{12}H_{25}$ chain moiety), 1.23 (m, 32H, -$CH_2(C\mathbf{H_2})_9CH_3$ of the $C_{12}H_{25}$ chain moiety), 1.35 (t, 4H -$C\mathbf{H_2}(CH_2)_9$), 1.67 (s, 12H, -$C(C\mathbf{H_3})_2$-SC(S)S-), 3.24 (t, 4H, -SC(S)$\mathbf{CH_2}CH_2$- of the $C_{12}H_{25}$ chain moiety), 3.62 (m, 4Hn -($C\mathbf{H_2}C\mathbf{H_2}$O)n of the PEO moiety), 4.23-4.40 (t, 8H, -$C\mathbf{H_2}C\mathbf{H_2}$-OC(O)$C(CH_3)_2$- of the PEO moiety). Mn_{GPC} = 7770 g mol_{-1}. The final degree of substitution is 99% as determined by ^{1}H-NMR.

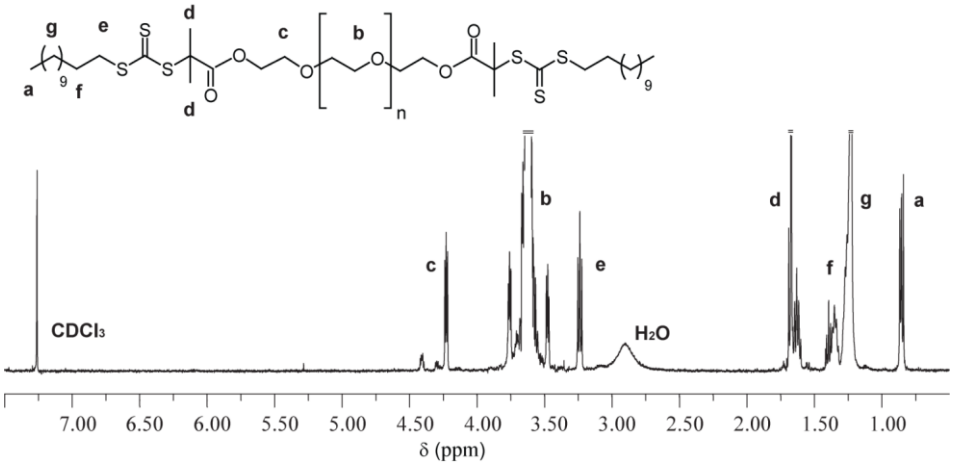

Figure 50. ^{1}H NMR of DDAT-PEO-DDAT.

The modification of PEO with the RAFT agent was made via esterification similarly to the one performed on the polylactide by M.A. Hillmyer et al.[110] The DDTA was chlorinated with oxalyl chloride in dry CH_2Cl_2. The PEO was

purified by azeotropic distillation from toluene, then the solution of DDTA-chloride was added via cannula under nitrogen to the PEO without any other solvent. After that, a solution of freshly distilled triethylamine in dry CH_2Cl_2 was added to the reaction mixture. The pure product was obtained after precipitation with ethanol. In Figure 50 was reported the ^{1}H-NMR spectra of product (1) that confirmed the formation of bond between RAFT agent and PEO, in particular the integrals of peaks at 3.24 ppm (CH_2 of the $C_{12}H_{25}$ chain moiety) and at 4.40 (CH_2 of the PEO moiety) was equal.

5.2.2. RAFT polymerization of copolymers

General procedure for PS-b-PEO-b-PS. A mixture of Styrene (5.5 mL, 48.0 mmol), DDAT-PEO-DDAT (0.7 g, 0.24 mmol), ratio M/T = 250:1, and anhydrous dioxane (5.5 mL) was degassed by three freeze-pump-thaw cycles, sealed, stirred and heated at 110°C, under nitrogen. After the prescribed time (view Table 3) the reaction mixture was dissolved in THF and precipitated in cold methanol.

Sample	**Reaction time/ h**	**conv.[a]/ %**	**Mn_{NMR}[b]**	**Mn_{GPC}[c]**	**Mw_{GPC}[c]**	**PDI_{GPC}[d]**
PEO_{136}	-	-		7500	10030	1,34
DDTA-PEO_{136}-DDTA	-	-		7770	10380	1,34
$PS_7PEO_{136}PS_7$	18	2	9460	9390	11430	1,22
$PS_{81}PEO_{136}PS_{81}$	32	42	40320	13900	21290	1,53
$PS_{191}PEO_{136}PS_{191}$	48	71	86140	20230	32220	1,59

Table 3. Synthesis and characteristics of Triblock Copolymers by GPC and ^{1}H-NMR Measurement. [a] Monomer conversion was determined by gravimetry, [b] Number-average molecular weight derived from ^{1}H NMR data, [c] Number-average molecular weight measured by GPC, [d] Molecular weight distribution measured by GPC.

The solid was filtered and dried under vacuum overnight. ^{1}H-NMR spectra confirmed the coexistence of the PS chain and the PEO chain in the macromolecular structure.

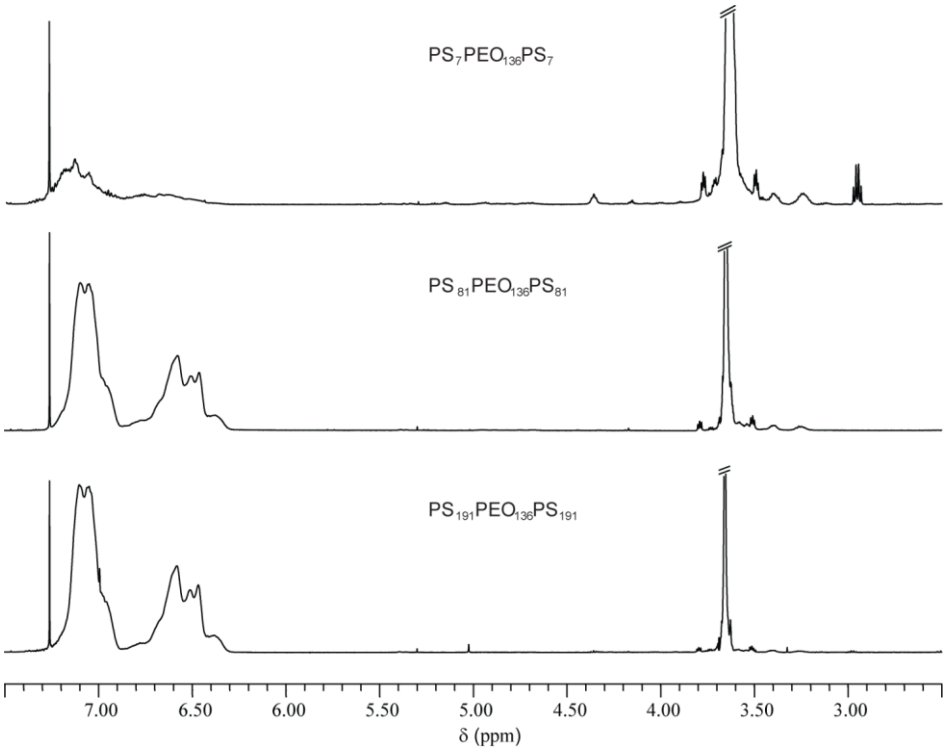

Figure 51. ^{1}H NMR($CDCl_3$) spectrum macro-CTA DDAT-PEO-DDAT.

The synthesis of different molecular weight PS-b-PEO-b-PS was done in anhydrous and degassed dioxane starting from DDAT-PEO-DDAT and styrene at 110 °C. The polymers were obtained pure after precipitation in methanol in a good yield. The different molecular weights were achieved tuning the reaction time as shown in Table 3. The proofs from ^{1}H-NMR spectra and GPC elucidated that the obtained products were PS-b-PEO-b-PS triblock copolymers. The typical ^{1}H-NMR spectrum of PS-b-PEO_{136}-b-PS triblock copolymers is reported in Figure 50. The signal at 3.46 –3.78 ppm is attributed to the methylene group of

PEO, the peaks at 6.64 –7.05 ppm are attributed to protons of the aromatic groups in PS. ^{1}H-NMR spectra confirmed the coexistence of the PS chain and the PEO chain in the macromolecular structure. The molecular weights were calculated from the ratio between the integrals of the repeating unit of the different samples, considering the molecular weight of PEO equal to 6000 g mol^{-1}. The value of PS was divided by two considering the polymer grown from both terminals of the PEO, and the structure of the block copolymers was obtained as $PS_7PEO_{136}PS_7$, $PS_{81}PEO_{136}PS_{81}$, $PS_{191}PEO_{136}PS_{191}$.

The presence of single peak in the GPC curves of the products, as shown in Figure 52, strongly supports the actual formation of the triblock, in fact in the presence of a blend of PS and PEO homopolymers, the GPC curves should present two separated peaks, one for the PS and the other for the PEO.

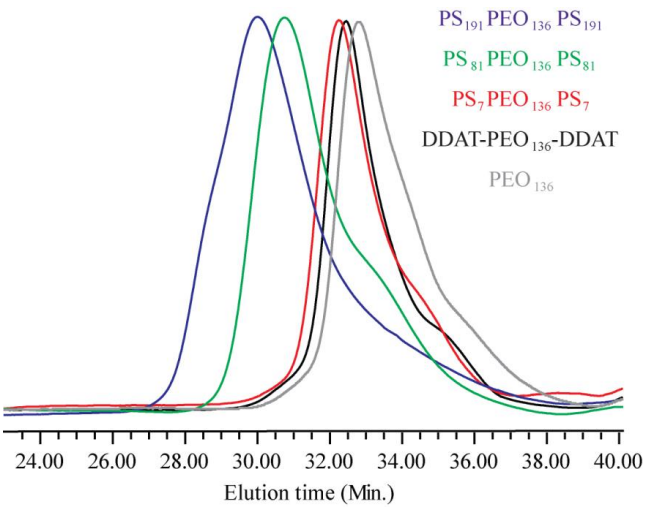

Figure 52. GPC curves of PS-b-PEO136-b-PS

Molecular weight calculated from GPC are in good agreement with the values derived from ^{1}H NMR. However, some discrepancies between the molecular weight measured by GPC and that from ^{1}H NMR were observed, which might be attributed to the sharp difference in hydrodynamic volume

between triblock copolymer PS-b-PEO-b-PS and PS standards in THF. A similar behavior is well known and coherent with data reported in literature.[111]

DSC thermogramms, Figure 53, show a decrease of the crystallization peak of polyethylene oxide with the increase of the PS fraction in the copolymer. The presence of RAFT agents as terminal groups of produces a decrease in the crystallization of about 30%. (Table 4). With the growth of the polystyrene block a drastic decreases in crystrallinity is evidebt, until its complete disappearance. This behavior is related to the different self assembly of the copolymer compared to PEO homopolymer.

Sample	**Tm_1 (°C)**	**ΔHm_1 (J/g)**	**Tc (°C)**	**ΔHc (J/g)**	**Tm_2 (°C)**	**ΔHm_2 (J/g)**
PEO_{136}	64.46	186.01	25.85	149.49	60.02	164.22
DDAT-PEO_{136}-DDAT	55.11	136.56	32.23	113.64	52.58	119.48
$PS_7PEO_{136}PS_7$	53.47	58.88	14.00	105.52	50.11	86.76
$PS_{81}PEO_{136}PS_{81}$	-	-	-	-	-	-
$PS_{191}PEO_{136}PS_{191}$	-	-	-	-	-	-

Table 4. The peak melt and crystallization temperature and enthalpy of PEO_{136}, DDAT-PEO_{136}-DDAT and PS-b-PEO-b-PS copolymer.

Absorption and desorption isotherms of acetonitrile were measured for block copolymers, measurements of since acetonitrile is the typical solvent for the electrolytic system, in order to verify the stability of this system within the cells. A film of 200 mg of copolymer was casted from toluene, the film was dried in vacuum for one night, afterwards100 μl of acetonitrile were added. Through a calibrated analytical balance (E50-Gibertini s) the weight loss was measured in an open vial and at room temperature.

The samples adsorb about 40 - 50 % of their mass and the desorption is 80 times slower than the pure solvent. In addition you notice any permanent swelling of the film when the sample is sealed.

In Figure 54 shown the polymeric film casted from toluene before and after acetonitrile adsorption is depicted .

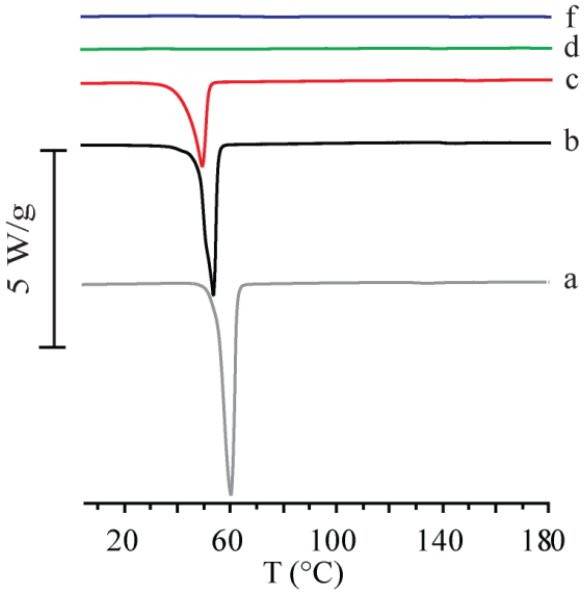

Figure 53. DSC thermogram (a) DDAT-PEO_{136}; (b) DDAT-PEO_{136}-DDAT; (c) PS_7-b-PEO_{136}-b-PS_7, (d) PS_{81}-b-PEO_{136}-b-PS_{81}, (e) PS_{191}-b-PEO_{136}-b-PS_{191}

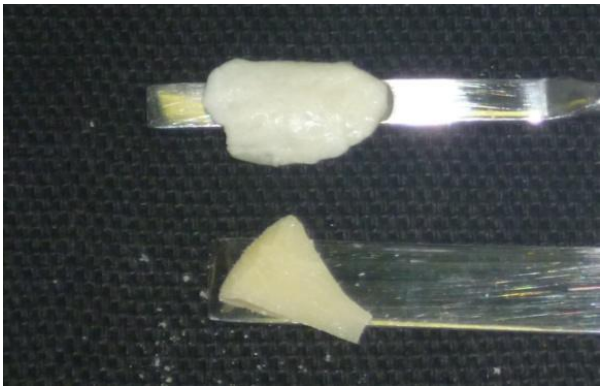

Figure 54. Polymeric film casted by toluene before (below) and after (above) acetonitrile adsorption.

5.3. Preparation and fabrication of DSSCs

DSSCs were prepared adapting a procedure reported in the literature[112]. In order to exclude metal contamination all of containers were in glass or Teflon and were treated with EtOH and 10% HCl prior to use. Plastic spatulas and tweezers were used throughout the procedure. FTO glass plates (Solaronix TCO 22-7, 2.2 mm thickness, 7 Ω/square) were cleaned in a detergent solution for 30 min using an ultrasonic bath, rinsed with pure water and absolute ethanol. FTO plates were treated with a freshly prepared 40 mM aqueous solution of $TiCl_4$ for 30 min at 70 °C and the rinsed with water and EtOH. An active monolayer of 10 µm was screen-printed using a 400 nm nanoparticle paste (Dyesol 18NR-AO). The coated films were dried at 125 °C for 6 min and then thermally treated under an air flow at 325 °C for 10 min, 450 °C for 15 min, and 500 °C for 15 min. The heating ramp rate was 5 - 10 °C/min.

The sintered layer was treated again with 40 mM aqueous $TiCl_4$ (70°C for 30 min), rinsed with ethanol and heated at 500 °C for 30 min. After cooling down to 80 °C the TiO_2 coated plate was immersed for 20 h in a 0.5 mM EtOH solution of the dye. The thickness of the layers was measured by means of a VEECO Dektak 8 Stylus Profiler.

Counter electrodes were prepared according to the following procedure. In the case of DSSC containing liquid electrolyte, a 1 mm hole was made in a FTO plate using diamond drill bits.

All the electrodes were cleaned with a detergent solution for 15 min using an ultrasonic bath, 10% HCl, and finally acetone for 15 min using an ultrasonic bath. After treatment in the UV-O_3 system for 18 min, a drop of a 5 x 10^{-3} M solution of H_2PtCl_6 in ethanol was added and heated at 500 °C for 30 min. In the liquid DSSC, the dye adsorbed TiO_2 electrode and Pt-counter electrode were assembled into a sealed sandwich-type cell by heating with a hot-melt ionomer-class resin (Surlyn 25 µm thickness) as a spacer between the electrodes. A drop

of the electrolyte solution was added to the hole and introduced inside the cell by vacuum backfilling and, finally, the hole was sealed with a sheet of Surlyn.

For the devices using block-copolymer electrolytes (Figure 55), 20 µL of a 3 x 10^{-4} M solution of $PSnPEO_{136}PSn$ in toluene was deposited on platinized counter electrode using a doctor-blade method and the solvent was allowed to evaporate. A drop of electrolyte was added on the polymeric film and the counter electrode was kept overnight in a cabinet, saturated with ethanol, until the polymer swells the electrolyte. The dye adsorbed TiO_2 electrode and Pt-counter electrode were assembled into a sandwich-type and sealed by using a commercial available cyanoacrylic glue (Loctite Super Attack Pocket Gel). A reflective foil at the back side of the counter electrode was taped to reflect unabsorbed light back to the photoanode.

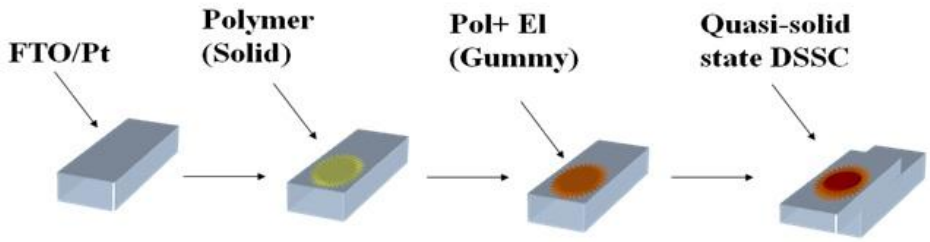

Figure 55. Scheme of preparation of DSSC.

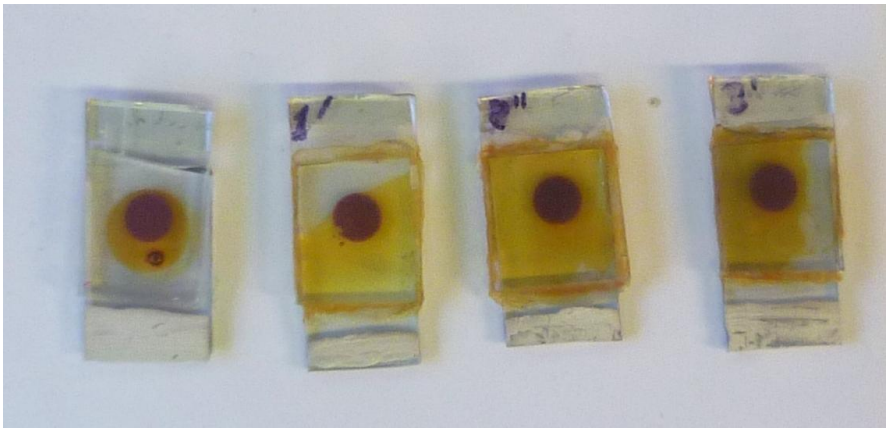

Figure 56. Images of devices. From lift: standard DSSC (containing liquid electrolyte), cell with block copolymer $PS_7PEO_{136}PS_7$, $PS_{81}PEO_{136}PS_{81}$ and $PS_{191}PEO_{136}PS_{191}$ respectively.

5.4. Photovoltaic performance measurements

Photovoltaic measurements of DSSCs were carried out using a 500 W Xenon light source (ABET Technologies Sun 2000 class ABA Solar Simulator). The power of the simulated light was calibrated to AM 1.5 (100 mW cm^{-2}) using a reference Si cell photodiode equipped with an IR-cutoff filter (KG-5, Schott) to reduce the mismatch in the region of 350-750 nm between the simulated light and the AM 1.5 spectrum. Values were recorded after 24 and 48 h, 7, 13 and 15 days of ageing in the dark. I–V curves were obtained by applying an external bias to the cell and measuring the generated photocurrent with a Keithley model 2400 digital source meter. Incident photon-to-current conversion efficiencies (IPCE) were recorded as a function of excitation wavelength by using a monochromator (Omni 300 LOT ORIEL) with single grating in Czerny-Turner optical design, in AC mode with a chopping frequency of 1 Hz and a bias of while light (0.3 sun). EIS spectra were obtained using an Eg&G PARSTAT 2263 galvanostat potentiostat at the open circuit voltage and under 250 W m-2 (0.25 sun) illumination. The measurements have been performed in the frequency range from 100 kHz to 0.1 Hz under ac stimulus with 10 mV of amplitude and no applied voltage bias. The obtained Nyquist plots have been fitted via a non-linear least square procedure using a simple equivalent circuit model.

Sample	**J_{sc} (mA cm^{-2})**	**V_{oc} (mV)**	**FF**	**PCE (%)**	**R_{el} [b] (Ω)**
$PS_7PEO_{136}PS_7$ +A6141 [a]	15.5	659	0.66	6.7	14.1
$PS_{81}PEO_{136}PS_{81}$ +A6141	15.4	656	0.66	6.7	12.6
$PS_{191}PEO_{136}PS_{191}$ +A6141	12.8	639	0.59	4.5	11.6
A6141	15.3	689	0.65	6.9	43.8

Table 5. Electochemical and photovoltaic characterization. [a] A6141 = 0.6 M BMII, 0.03 M I2, 0.1 M GSCN, 0.5 M TBP in ACN/VN=85/15. [b] obtained plotting the data taken by electrochemical impedance spectroscopy.

The best measured photovoltaic performances are listed in Table 5, in comparison with those measured with the standard liquid electrolyte A614128 (0.6 M N-butyl-N-methyl imidazolium iodide, 0.03 M I2, 0.10 M guanidinium thiocyanate, and 0.5 M 4-t-butylpyridine in acetonitrile/valeronitrile 85:15) under the same experimental conditions. The overall conversion efficiencies PCE were derived from the equation:

$$PCE = J_{sc} * V_{oc} * FF$$

where J_{sc} is the short circuit current density, V_{oc} the open circuit voltage, and FF the fill factor. Figure 57 shows the photocurrent-voltage curves of DSSCs based on block-copolymer electrolytes.

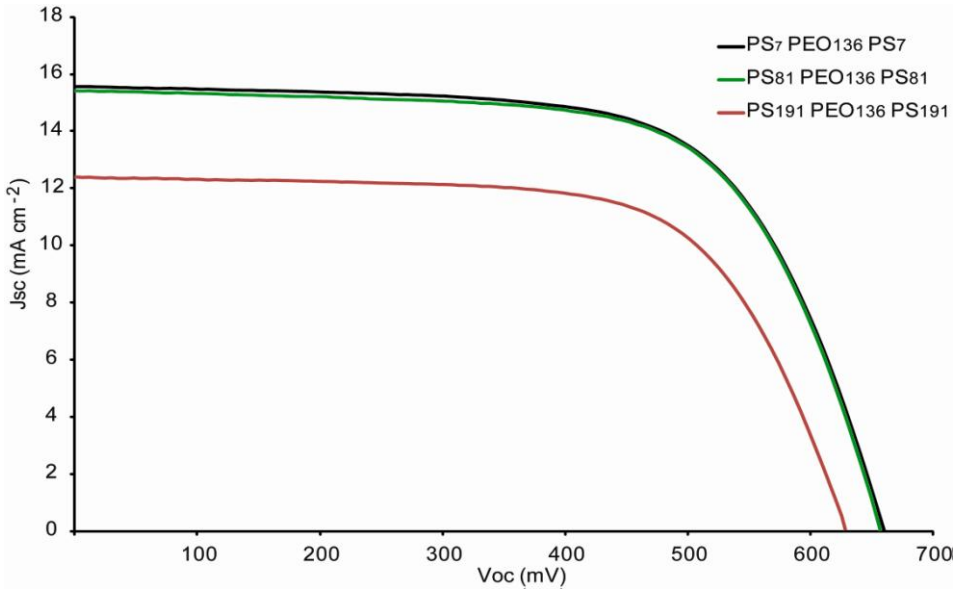

Figure 57. Current–voltage characteristics of DSSCs using block-copolymer electrolytes.

The properties of electrolyte conductivity were investigated by means of electrochemical impedance spectroscopy (EIS) and the resistivities of the polymeric layers are listened in Table 5, in comparison with the conventional liquid electrolyte. In this experiment, a small sinusoidal voltage stimulus of fixed frequency is applied to an electrochemical cell and its current response is measured. The ac behavior of an electrochemical system can be investigated by sweeping the frequency over several orders of magnitude (generally from a few mHz to several MHz). The analysis of impedance spectra is usually performed in terms of Nyquist plots where the imaginary part of the impedance is plotted as a function of the real part over the range of frequencies. Equivalent circuits built in series or parallel combinations of simple elements like resistance, capacitance, and inductance are often used to qualitatively describe the electrode material, while the determination of their numeric values by fitting procedures yields quantitative data. In a DSSC the nano-porous photo-electrode, the electrolyte and the platinized counter-electrode show different time constants, i.e. characteristic frequencies, and thus can be seen as separated impedance arcs in the Nyquist plot.[113]

As a consequence, the impedance of a DSSC can be described by an equivalent circuit model,[114,115,116] in which the different cell components and their interfaces are treated as discrete electrical elements. The remarkable result revealed by EIS is that the copolymers seem to help the ionic conductivity, decreasing the resistance of the electrolyte, which is even higher in the liquid one.

Furthermore, the devices built with copolymers, both those stored in the dark and ones left under weathering, have shown a good stability as can be seen in the Figure 58 and in Table 6 and Table 7.

Days	Sample	J_{sc} (mA cm^{-2})	V_{oc} (mV)	FF (%)	PCE (%)
1	$PS_7PEO_{136}PS_7$ +A6141	14.1	660	0.65	6.1
	$PS_{81}PEO_{136}PS_{81}$ +A6141	13.4	664	0.68	6.0
	$PS_{191}PEO_{136}PS_{191}$ +A6141	11.5	650	0.61	4.6
	A6141	15.6	701	0.67	7.3
3	$PS_7PEO_{136}PS_7$ +A6141	15.5	659	0.66	6.7
	$PS_{81}PEO_{136}PS_{81}$ +A6141	15.4	656	0.66	6.7
	$PS_{191}PEO_{136}PS_{191}$ +A6141	12.8	639	0.59	4.5
	A6141	15.3	689	0.65	6.9
7	$PS_7PEO_{136}PS_7$ +A6141	15.8	641	0.64	6.5
	$PS_{81}PEO_{136}PS_{81}$ +A6141	16.1	635	0.64	6.6
	$PS_{191}PEO_{136}PS_{191}$ +A6141	13.0	619	0.52	4.2
	A6141	/	/	/	/
12	$PS_7PEO_{136}PS_7$ +A6141	16.2	638	0.64	6.6
	$PS_{81}PEO_{136}PS_{81}$ +A6141	16.5	630	0.63	6.6
	$PS_{191}PEO_{136}PS_{191}$ +A6141	13.2	618	0.49	4.0
	A6141	/	/	/	/
15	$PS_7PEO_{136}PS_7$ +A6141	15.7	631	0.64	6.4
	$PS_{81}PEO_{136}PS_{81}$ +A6141	15.5	623	0.63	6.1
	$PS_{191}PEO_{136}PS_{191}$ +A6141	12.4	597	0.46	3.4
	A6141	13.5	693	0.65	6.1

Table 6. Photovoltaic parameters of DSSCs stored in the dark.

Days	sample	Jsc (mA cm-2)	Voc (mV)	FF (%)	PCE (%)
3	$PS_7PEO_{136}PS_7$ +A6141	16.7	617	0.65	6.7
	$PS_{81}PEO_{136}PS_{81}$ +A6141	13.2	635	0.67	5.6
	$PS_{191}PEO_{136}PS_{191}$ +A6141	12.4	628	0.67	5.2
15	$PS_7PEO_{136}PS_7$ +A6141	6.1	623	0.62	2.3
	$PS_{81}PEO_{136}PS_{81}$ +A6141	15.2	614	0.61	5.7
	$PS_{191}PEO_{136}PS_{191}$ +A6141	13.4	595	0.57	4.5

Table 7. Photovoltaic parameters of DSSCs stored under weathering.

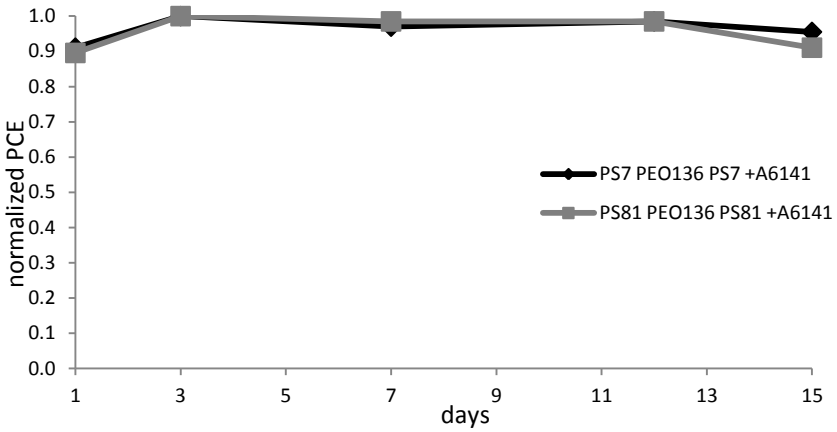

Figure 58. Normalized efficiency of the devices containing copolymers $PS_7PEO_{136}PS_7$ and $PS_{81}PEO_{136}PS_{81}$.

5.5. Conclusion

In order to fabricate a "quasi-solid" polymeric scaffold for the free diffusion of electrolytes in the DSSC, a set of amphiphilic triblock copolymers PS-b-PEO-b-PS has been synthesized. Since acetonitrile, the solvent typically used in DSSC, is a selective solvent for the PEO block, the phase separated block copolymer will be only partially swollen with the PS block hardly modified. In

such a way the PS areas provide dimensional stability and mechanical strength to the film, meanwhile PEO areas are solubilized by acetonitrile generating liquid-like pathways for the o the electrolytic system. Three samples, with different length of the polystyrene block were synthesized with RAFT technique, a technique able to control the polydispersity of the molecular weights without the need of metal catalysts. The copolymers showed a decrease of crystallinity of the polyethylene oxide with the increase of the styrenic block.

DSSC cells have been prepared with the copolymer as polymer matrix for the electrolytic solution. Measurements of electrical conductivity show efficiencies of about 6.7 % comparable to that of standard electrolyte DSSC (6.9 %). Moreover the cells are stable with time: a device kept for 15 days under outdoor conditions with sunlight and climate stress has shown unvaried power conversion efficiency.

Therefore this new polymeric host electrolytes could be of interest for a new generation of quasi solid-state DSSC, especially for their high tunability of physic-chemical and mechanical properties.

Chapter 6. Rutile–PS composite with high dielectric constant

In this chapter I will present the synthesis of polystyrene grafted on the surface of TiO_2 nanocrystals (rutile polymorph). The obtained core-shell particles are used for the fabrication of a polymeric nanocomposite endowed with high dielectric constant.

A brief literature review on the fabrication and characterization of nanocomposites with potential application as dielectric materials is reported. Methods based on RAFT polymerization will be discussed with special attention to the CTAs and reaction conditions used. The morphology of the PS@ TiO_2 core shell particles, as dispersed in the polymeric matrix at various concentrations, will be investigated. Finally the electrical properties of the devices will be discussed.

In particular, we have verified that the polymer molecules attached to the surfaces of TiO_2 nanoparticles exist in a "brush" regime. By increasing the filler concentration, the composites show a high dielectric constant, which is ascribed to the self-assembly of rutile nanoparticles in chestnut-burr aggregates, where a number of rutile crystals share the lateral faces and form capacitive microstructures. Moreover, the crystals are separated by a polymer thin layer and allow a high percolative threshold of 41% v/v filler content, before the formation of a continuous network responsible for the sudden change of the dielectric characteristics.

6.1. Introduction

High dielectric constant (ε_r) materials received large interest from a variety of technological applications such as gate dielectrics,[117] electroactive devices[118] and charge-storage capacitors.[119] Moreover the same materials were investigated as a base for storage energy devices in electric powered vehicles and pulse power applications.[120] In these contexts, polymeric materials offer a new approach towards low cost and flexible large area electronic devices,[121] although they require the dielectric properties to be enhanced preserving flexibility.[122] In fact high dielectric constant materials, like titanium dioxide (ε_r = 31, anatase; ε_r = 114, rutile),[123] strontium titanate (ε_r = 150)[124] or $Ba_{0.6}Sr_{0.4}TiO_3$ (ε_r = 4000),[125] display suitable electrical properties but they are not easily processable,[126] instead easily processable systems such as polymers, poly(methyl methacrylate) (ε_r = 3.12)[127] or polystyrene (ε_r = 2.6)[128] typically exhibit low dielectric constants.

In principle, polymer–inorganic composites offer the possibility of combining the desired electrical properties with flexibility and printability. Recent studies showed a moderate increase in the dielectric permittivity by incorporating high ε_r nanofillers such as titania,[129] zirconia,[130] alumina,[131] and barium titanate[132] into a polymeric matrix. Badheka et al. reported that the incorporation of nanometric particles of barium titanate (40 vol%) into PS increases the dielectric constant significantly from 2.6 to 20, but it is still much lower than the value ε_r = 1700 of the ceramic phases.[133]

The dielectric properties of a composite material depend on the composition (matrix and filler), and particularly on the loading, size, shape and orientation of the particles.[134] Many models described the effective dielectric properties of materials incorporating particles into a continuous matrix. When the filler volume within the matrix increases, the formation of a microcapacitor network occurs.[135] These microcapacitors are formed by close conductive filler particles and thin layers of dielectric in between, contributing to a very large

capacitance. Some of the conductive filler particles within the capacitive microstructures are connected in parallel and some others in series. The connection in parallel is able to increase the material capacitance.[136] The large capacitance contributed by these microcapacitors induces a significant increase in the intensity of the local electric field and promotes the accumulation of charge carriers at the filler–matrix interface. This polarization, known as the Maxwell–Wagner effect, is responsible for the enhancement of the dielectric constant.

When the density of the microcapacitors becomes very relevant, a conductive network takes place and a percolation phenomenon appears as a discharge between the electrodes.[137] Based on this model the trend of electrical properties with the filler concentration shows three regions. The first region is defined for the low filler amount and is characterized by the gradual rise of the dielectric constant with concentration. The particles are randomly dispersed and their contribution to the ε_r is well predictable by the classical mixing formulae. In the second region further increase of the filler concentration causes the formation of microaggregates acting as microcapacitive structures. The consequent enhancement of the dielectric constant can be described according to eq. 10:[138,139,140]

$$\varepsilon_r = cA^{-q} \qquad (10)$$

where ε_r is the relative dielectric constant, c is a constant prefactor, $A = (v_c - v)/v_c$ is the reduced volume fraction, v is the volume fraction of the particles, v_c is the percolation threshold and q has the critical value about 1. In order to fit the experimental data, some authors use the dielectric constant of the matrix as c prefactor; we will use q, v_c and c as adjustable parameters. In the third region, at high filler concentrations, the microaggregates connect, causing the formation of the conductive network and the consequent decrease of ε_r. Between the second and the third region lies the percolation threshold namely the critical filler

volume fraction where the connectivity between the particles extends throughout the system. Furthermore the dielectric loss (tanδ), defined as the ratio between the lossy response to the electric field and the lossless one, arises.[141] Tanδ is a representative of the material energy dissipation, thus a suitable material should have high ε_r and low tanδ.

At the microscopic level the amount and the distribution of a specific filler into the matrix are the main parameters to control for achieving high ε_r and low tanδ. The beneficial properties derived from the dispersion of high dielectric inorganic particles into a polymer matrix are maximized when the particles are homogeneously distributed at the nanometric level.[142] Unfortunately polymer matrices are not generally polar and compatible with the surface of the inorganic particles. Thus, one of the main issues in the fabrication of nanocomposites is the surface modification of the filler nanoparticles to make them compatible with the polymer.

6.2. RAFT polymerization of the PS@TiO_2 nanoparticles

The preparation of core–shell particles was performed in two steps (Scheme 12 and Scheme 13): surface modification of TiO_2 nanoparticles with the RAFT agent (CTA@TiO_2) and RAFT polymerization of styrene (PS@TiO_2).

As mentioned in Chapter 2 of the RAFT polymerization allows the synthesis of polymers from the surface of nanoparticles (grafting from) and depends on how the RAFT agent binds to it. The RAFT agent can be anchored on the surface by either Z or R group. On rutile surface two RAFT agents were used, DDAT and BSPA respectively. Both molecules present a terminal carboxyl moiety, DDAT on R, BSPA on Z. Carboxyl groups can coordinate the Ti(IV) atoms present on the titania surface, through three possible coordination modes, monodentate, chelating or bridging bidentate (according to Rotzinger et al.)[143,144]

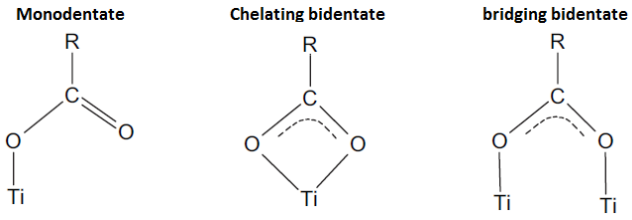

Scheme 59. Coordination modes of $RCOO^-$ with titania surface.

Once obtained the surface modified with the CTAs, the parameters of RAFT polymerization (namely reaction time and ratio between monomer and RAFT agents) were varied. The systems were optimized to obtain a high degree of coating of nanoparticles and a high chain length of polystyrene.

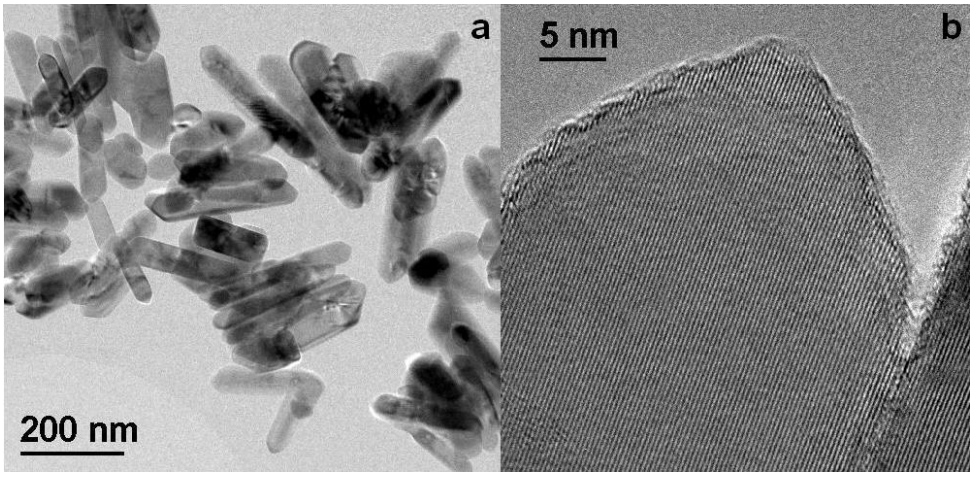

Figure 60. TEM (a) and HRTEM (b) images of hydrothermally obtained rutile nanocrystals.

Nanocrystalline TiO_2 rutile was obtained by hydrothermal synthesis, and kindly provided by another group, according to reported procedure.[145] Aqueous solutions of $TiOCl_2$ and NH_3 (>25 wt%) was reacted in a Teflon lined autoclave

(Parr, model 4768Q) at 220°C. TEM and HRTEM images of the employed TiO_2 rutile nanocrystals are reported in Figure 60. The hydrothermal procedure adopted allowed the production of particles, which are single nanocrystals with pronounced faceting and with highly reproducible morphology. No internal pores or amorphous surface layers were detectable. The nanocrystals have elongated prismatic shape (rod-like) with a length of 160–200 nm and a width of 25–30 nm. They grow in the [001] direction and have the tendency to form aggregates by sharing the {110} faces.

6.2.1. Synthesis of CTA@ TiO_2

5 g of TiO_2 were suspended in 50 ml of anhydrous methanol under nitrogen atmosphere. A large excess of DDAT (0.5 g) was then added and the suspension was kept for 96 hours in the dark under stirring at room temperature in an inert atmosphere. The particles were recovered by centrifugation (30 min at 6000 RPM). In order to remove the unreacted CTA and the residual traces of methanol, the powder was washed for 20 minutes under ultrasound conditions with ethyl acetate (3 times, 50 ml each) and CH_2Cl_2 (3 times, 50 ml each). The final wet powder was dried in air at room temperature and the residual solvent evaporated under vacuum overnight.

The same procedure was followed for BSPA. The products synthesized were called DDAT@TiO_2 and BSPA@TiO_2 respectively.

The surface density of RAFT agents on the TiO_2 nanoparticles was determined by TGA. As reference, TGA of pristine rutile was also performed. The curve of pristine is then subtracted to the core-shell particles thermogram, in this way the weight losses associated to surface reconstruction of rutile are neglected and the thermogram measures only the degradation of organic material bound to nanoparticles (weight losses were measured between 150 ° C and 600 °C). From the measured weight loss of 1.01%, the amount of grafted RAFT in

the DDAT@TiO_2 agent was evaluated to be 0.28 mmol g^{-1}. Assuming that the molecules are equally distributed on the surface and the surface area of pristine rutile is 36 m^2g^{-1} (measured by BET), the number of molecules per nm^2 (**Σ**) is 0.5 CTA per nm^2. Thus the average distance ($D = \sqrt{4/\pi\Sigma}$) between the molecules anchored to the surface is 1.6 nm. The sample TiO_2-BSPA (0.6 per nm^2) has a greater surface coverage presumably due to less steric hindrance of the molecule.

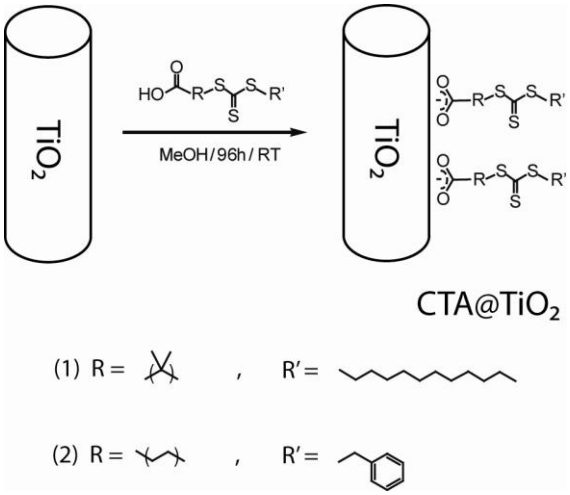

Scheme 12. Reaction scheme of RAFT agents (DDAT) and (BSPA) to the surface of the nanoparticles.

Sample	Loss %	PM (g/mol)	mmol[d]	SSB (m^2/g)[a]	D (nm)[b]	Σ (nm^2)[c]
DDAT@TiO_2	1.01	364	0.280	36	1.6	0.5
BSPA@TiO_2	1.09	272	0.356	36	1.5	0.6

Table 8. Density of coating of the RAFT agents on TiO_2. [a] to the surface area (SSB) by BET measurements carried out on the particles of rutile pristine. [b] the average distance ($D = \sqrt{4/\pi\Sigma}$) between the molecules anchored to the surface of the transfer members. [c] the number of molecules per nm^2 (Σ), or surface density of molecules. [d] millimoles per gram of TiO_2 in analogy to measure BET.

By ATR-IR measurements, it was determined the coordination of the carboxylic group of the CTA on the surface of TiO_2. In the spectrum of the samples DDAT@TiO_2 and BSPA@TiO_2 there are no bands of the carboxyl group, namely the stretching of the bond C = O at 1705 cm^{-1}, the deformation of the bond C-O-H to 1415 cm^{-1} and the stretching of C-O in 1240 cm^{-1}. This is confirmed by the presence of modes of stretching of the carboxylate in the range 1300-1600 cm-1 compared to the spectrum of the pristine rutile. Furthermore, the presence of modes of stretching of the CH bonds of the chain $C_{12}H_{25}$ between 2750 cm^{-1} and 3000 cm^{-1} and the band at 1450 cm^{-1}, ensure the formation of the bond between RAFT agent and nanoparticle, despite the particles have been applied to repeated washing cycles.

6.2.2. RAFT polymerization of styrene on TiO_2 nanoparticles.

The polymerization was performed in pure styrene under argon (Scheme 13). To study the degree of polymerization of polystyrene chains grown on the surface of the nanoparticles, the reaction time and ratio of concentrations of styrene [M] and RAFT agent [T] were varied. The syntheses were performed changing parameters polymerization time and [M]/[T] as shown in table 2.

0.2 g of functionalized particles (DDAT@TiO_2), with a resulting transfer agent net content of 1.18 10^{-5} mol, were kept at reduced pressure (102 Torr) for 2 hours before the addition of suitable quantity of styrene. The mixture was homogeneously dispersed by ultrasound treatment, four freeze–pump–thaw cycles were performed to remove the oxygen. The polymerization reaction was conducted at 110 °C for 96 h under a nitrogen atmosphere and was interrupted by quenching the mixture in liquid N_2.

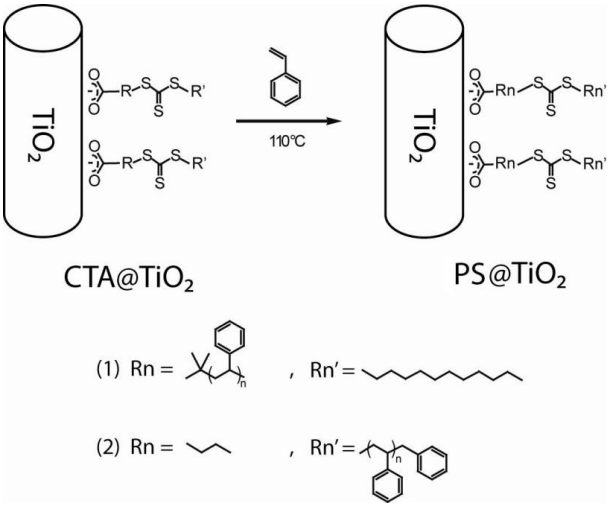

Scheme 13. Scheme of RAFT polymerization of styrene on CTA@TiO_2.

The crude reaction product appears as a white glossy solid because, in addition to polymerization on the surface of the particles via RAFT, free polystyrene is formed. To separate PS@ TiO_2 from the ungrafted polystyrene, the solid was dissolved in CH_2Cl_2 (100 ml) and the particles were separated by centrifugation (6000 RPM for 30 min). The recovered particles were washed three times with CH_2Cl_2 under ultrasound conditions, separated by centrifugation and finally dried in a vacuum overnight. The free polymer was precipitated in methanol.

Kinetics of polymerization and the degree of polymerization as function of [M]/[T] ratio were calculated using TGA analysis. By assuming that each grafted transfer agent molecule enables the growth of a single chain, and that the RAFT technique ensures a very low polydispersity, the chain length, *i.e.* the number of monomer units (N.u.m), was estimated according to equation 11:

$$N.u.m = \frac{\%_{loss} * MW_{CTA@TiO_2}}{MW_{Sty}} \qquad (11)$$

Where $\%_{loss}$ is the loss weight percentage of the organic part, $MW_{CTA@TiO2}$ is the molecular weight of the transfer agent on the surface, and MW_{sty} is the molecular weight of the styrene

Sample	CTA	$t_{reaction}$ (h)	[M]/[T]*1000	loss %	N u.m.[a]
PS1@ TiO_2	DDAT	6	7.2	3.77	10
PS2@ TiO_2	DDAT	10	7.2	4.02	11
PS3@ TiO_2	DDAT	15	7.2	5.85	18
PS4@ TiO_2	DDAT	24	7.2	6.15	19
PS5@ TiO_2	DDAT	48	7.2	10.50	34
PS6@ TiO_2	DDAT	96	7.2	13.48	46
PS7@ TiO_2	DDAT	172	7.2	12.86	43
PS8@ TiO_2	BSPA	10	7.2	2.40	4
PS9@ TiO_2	BSPA	48	7.2	2.81	5
PS10@ TiO_2	BSPA	96	7.2	3.96	9
PS11@ TiO_2	BSPA	172	7.2	3.79	8
PS12@ TiO_2	DDAT	96	1.3	2.53	5
PS13@ TiO_2	DDAT	96	2.5	3.66	9
PS14@ TiO_2	DDAT	96	3.8	5.63	15
PS15@ TiO_2	DDAT	96	7.2	13.48	46
PS16@ TiO_2	DDAT	96	10.8	7.48	22
PS17@ TiO_2	DDAT	96	14.4	4.63	12
PS18@ TiO_2	DDAT	96	28.8	4.03	10

Table 9. Synthesis parameters and TGA analysis of the RAFT polymerization of polystyrene on TiO_2. [a] N u.m. is the number of monomer units constituting the chain.

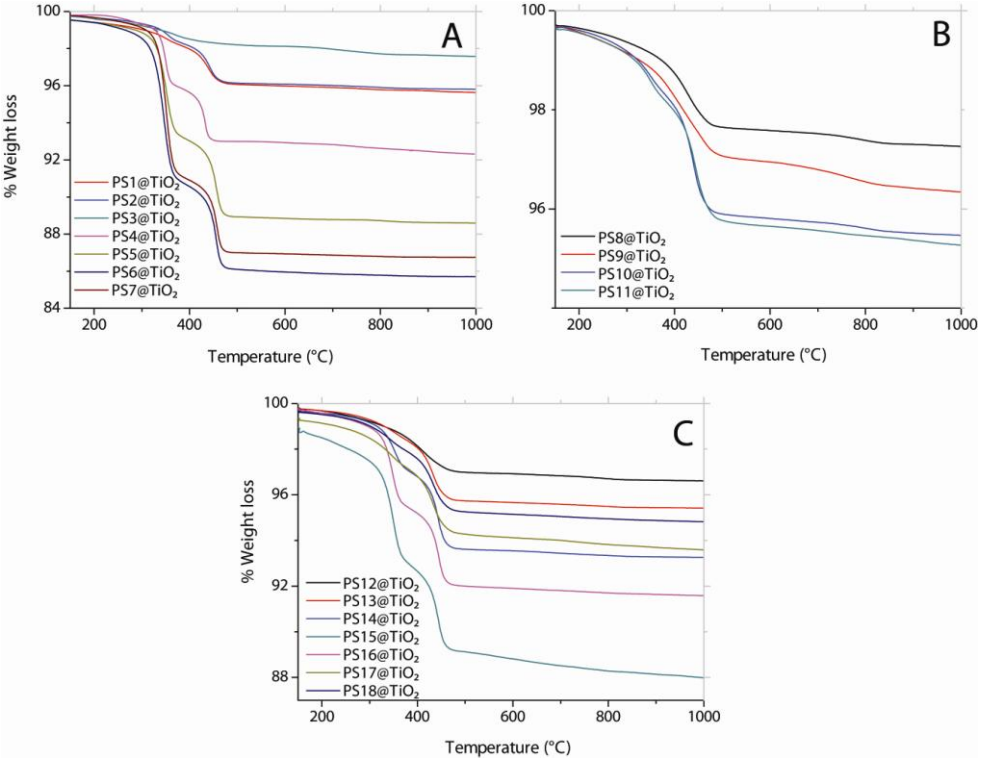

Figure 61. Comparison between TGA measurements of grafting form RAFT polymerization on functionalized nanoparticles, changing reaction time A) with DDAT@TiO_2, B) with TiO_2-BSPA. changing reaction time, C) with DDAT@TiO_2 changing [M]/[T].

In Figure 61 a and b the increase of weight loss associated with longer reaction times (respectively for reactions carried out with the RAFT agents DDAT and BSPA) is shown.

Comparing the kinetics for the functionalized particles, at fixed [M]/[T] ratios, we can observe that DDAT transfer agent is more efficient in the growth of the polymer chains. This result can be attributed to the different modes of operation respect to BSPA. Highlighting that in both cases the carboxylic functionality binds to the surface, it is possible to make the following considerations. In the case of DDAT@TiO_2 the carboxyl group is located on the

R residue, thus during the polymerization, the monomer inserts between the trithiocarbonyl group and the most substituted carbon, causing a shift of the trithiocarbonyl group to the exterior of the nanoparticle surface, thus at each polymerization step the trithiocarbonyl group becomes more available for the forthcoming monomer. Instead, BSPA transfer agent is bound to the surface by the Z group, so during the growth of the polymer chain the trithiocarbonyl group remains close to the surface and is buried by the polymer chain itself, limiting the access of the monomer to the reactive site.

After having verified that DDAT generates polymer chains with higher molecular weights, an optimal reaction time of 96 h was found. The effect of variation of [M]/[T] ratio on the MW of the obtained polymer chains was studied (see Figure 62).

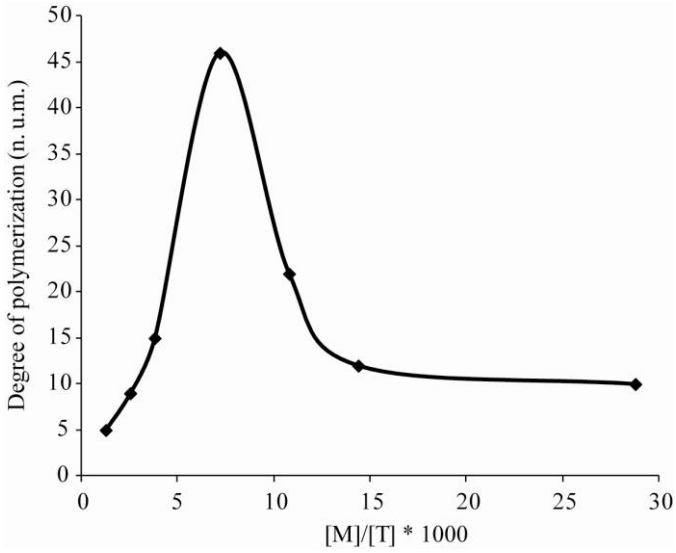

Figure 62. Trend of [M]/[T] ratio on the MW in RAFT polymerization on DDAT@TiO_2.

This result can be explained quantitatively because the local RAFT reaction yield depends both on the different variables and the average distance of

the particles. The use of ultrasound before the reaction and magnetic agitation during the same provides, in principle, an optimum dispersion of the nanoparticles in styrene. The effectiveness of the polymerization is affected by the distance of the sites of polymerization and by the mobility of radicals. At high monomer concentration, since the polymerization is thermally activated, the number of growing polymer chains of free polystyrene increases, causing a raise of the viscosity and leading finally to well-known "cage effect," the nanoparticles cannot be reached by the monomer anymore: the degree of polymerization, remains constant after a certain [M]/[T] ratio.

Through GPC (Table 10) analysis we can investigate the nature of the polymerization process involving free polystyrene. The polymer is dusty and does not have the typical pale yellow color which characterizes a PS grew up with RAFT technique (given by the function trithiocarbonyl). High polydispersity were obtained especially in the samples with shorter chains and where the process of polymerization was slowed down (use BSPA@TiO_2 and high reaction times).

In order to fabricate the nanocomposite, the conditions that lead to sample with more extended polystyrene chains, TiO_2-PS15, are used to produce a large amount of surface modified titania. 4.5 g of DDAT@TiO_2 were synthesized and used for the RAFT polymerization of 104 ml styrene ([M] / [T] = 7200) at 110 °C during 96 hours. After purification, the sample was characterized (PS@ TiO_2).

In Figure 63, the comparison of the TGA thermograms of synthesized samples is shown. In PS@ TiO_2 nanoparticles, the weight loss attributed to the polymer grafted on the TiO_2 resulted to be 12.2 ± 0.2%. Holding to the same assumptions as above, the chain length was estimated in 42 styrene repeat units.

Sample	Mn (g/mol)*1000	Mw (g/mol)*1000	Polydispersity
PS1@ TiO_2	31.1	65.0	2.09
PS2@ TiO_2	43.7	87.8	2.01
PS3@ TiO_2	43.7	63.6	1.46
PS4@ TiO_2	46.7	89.6	1.92
PS5@ TiO_2	68.6	121.1	1.77
PS6@ TiO_2	72.1	144.2	2.00
PS7@ TiO_2	73.9	146.9	1.99
PS8@ TiO_2	130.2	323.2	2.48
PS9@ TiO_2	190.6	436.2	2.29
PS10@ TiO_2	200.1	502.4	2.51
PS11@ TiO_2	221.1	512.0	2.31
PS12@ TiO_2	2.1	4.6	2.22
PS13@ TiO_2	62.6	88.6	1.41
PS14@ TiO_2	100.3	143.8	1.43
PS15@ TiO_2	181.0	306.3	1.69
PS16@ TiO_2	189.7	327.0	1.72
PS17@ TiO_2	235.4	427.9	1.82
PS18@ TiO_2	333.2	542.1	1.62

Table 10. GPC analysis of free PS relative to grafting from RAFT polymerization.

The FT-IR ATR spectrum (Figure 63) of DDAT@TiO_2 showed the stretching modes of methyl and methylene groups at 2956, 2924 and 2855 cm^{-1}. This assessed the integrity of the grafted CTA aliphatic chain. The CTA interaction with TiO_2 is demonstrated by the absence of C=O vibration mode at 1703 cm^{-1}, characteristic of the free aliphatic acids, and by the presence of both asymmetric and symmetric stretching bands of the deprotonated carboxyl moiety

(COO^-), respectively at 1504 and 1434 cm^{-1}. The spectrum of TiO_2-PS clearly showed the presence of PS, since the notable peaks are very evident, being in the range of 3000–3100 cm^{-1} the C–H stretching modes and in the range of 1450–1650 cm^{-1} the C–C stretching mode due to phenyl rings.

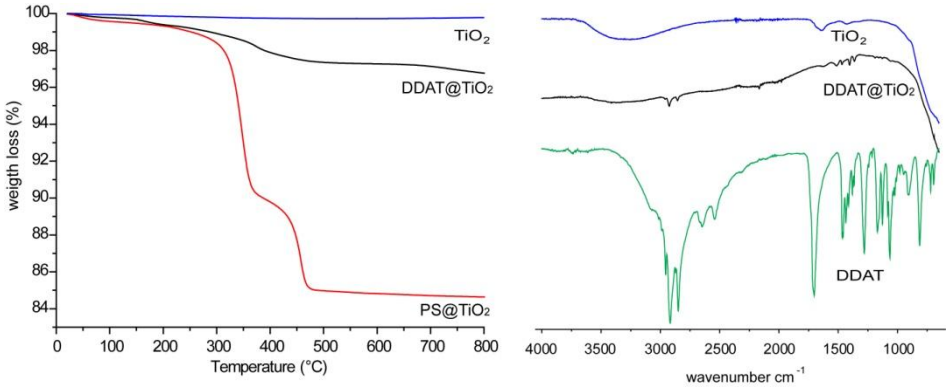

Figure 63. At left, TGA curves of bare rutile nanoparticles, DDAT grafted rutile nanoparticles (TiO_2-DDAT) and PS grafted rutile nanoparticles (PS@TiO_2). At right FT-IR spectra of bare rutile nanoparticles, DDAT grafted rutile nanoparticles (DDAT@TiO_2) and PS grafted rutile nanoparticles (PS@TiO_2).

More detailed evidence of the polymerization on the TiO_2 surface is provided by the ^1H NMR investigation of the $CDCl_3$ colloidal dispersion of core–shell PS@TiO_2 nanoparticles (Figure 64). The signals of PS (aromatic protons δ = 6.5–7.2 ppm, CH_2 and CH protons δ = 1.3–2 ppm) with the line width characteristic of long macromolecular chains and two signals of the RAFT agent (CH_3 and CH_2 of the dodecyl residue) with reduced line width distinctive of terminal groups were detected.

In order to measure the polymerization degree of the PS chains grafted on TiO_2–PS by GPC, the polymer was cleaved from the core–shell particles according to the following procedure. About 110 mg of TiO_2–PS were dissolved in a solution of 50 ml of THF and 2 ml of HCl (2 M). The solution was stirred at 80°C under reflux for 24 hours. After the precipitation of white powders, the

solid was removed by centrifugation (6000 RPM for 15 min). The supernatant was reduced in volume and the polymer was recovered and purified through precipitation in methanol. The obtained polystyrene was dried under vacuum for 24 hours (10^{-2} Torr). GPC analysis of the cleaved polystyrene (Figure 64) from the nanoparticles gave molecular weight Mn = 4800 g mol^{-1} (polydispersity = 1.11) which, subtracting the Mw of the RAFT transfer residuals (364.62 g mol^{-1}) and considering the Mw of styrene (104 g mol^{-1}), corresponds to an average chain length of 42.6 in agreement with the evaluation by TGA.

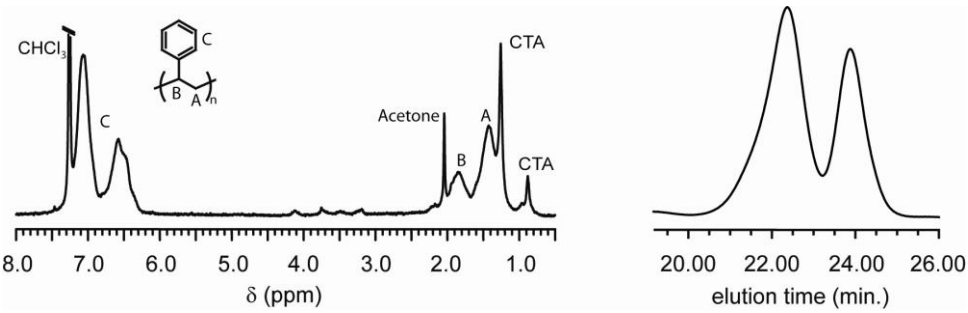

Figure 64. At lift ^{1}H NMR spectrum of PS chains grafted on rutile nanoparticles. At right GPC analysis of PScleaved.

Knowing the molecular weight of the polymer grown on the titania surface, the size of its random coil can be evaluated. The radius of gyration, Rg, for polystyrene in a good solvent can be calculated using the equation 12:

$$R_g = \frac{b}{\sqrt{6}} * \left(\frac{M_w}{M_c}\right)^{0.6} \qquad (12)$$

where b is the length of the Kuhn segment (1.8 nm for polystyrene), M_w is the average molecular weight, and M_c is the molar mass of the Kuhn segment (720 g mol^{-1} for polystyrene).[146] Considering a M_w of 5300 g mol^{-1}, a Rg of 2.44 nm was estimated. Taking into account that the distance between the anchored polymer

chains, estimated by TGA and BET measurements, was 1.6 nm, the polymer molecules grafted on the large flat faces of titania nanocrystals are stretched away from the surface and exist in a ‘‘brush’’ regime.

The presence of a brush-like behavior of the polymer chains can explain the relatively low molecular weight of the grafted chains obtained by the RAFT polymerization, although a monomer/transfer agent ratio of 7200 and the very long reaction time would lead to a higher molecular weight.

Considering the high concentration of RAFT agents on the flat surface of rutile nanoparticles, the polymerization stops when the growing polymer chain reaches a limiting molecular weight determined by the maximum deformation possible for the random coil in the polymerization medium.

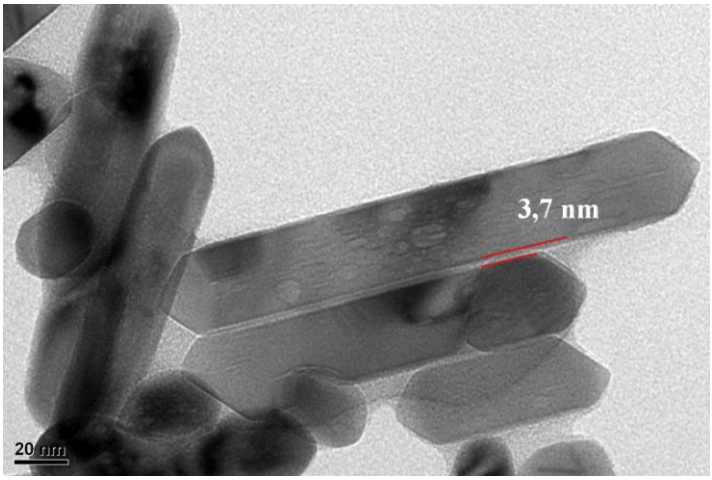

Figure 65. TEM micrograph of rutile rods coated with the polystyrene shell (PS@TiO_2).

Despite the low molecular weight of the polymers and thanks to the low polydispersity index (1.11) we can gather that the shell covering particles have a high surface molecular density of homogeneous chains, which ensures the compatibilization of the inorganic filler with the matrix. The thickness of the polymeric film surrounding TiO_2 nanoparticles was estimated to be about 1.8 nm

from half the thickness of the layer intercalating the rutile rods (Figure 65). This ensures a very thin layer of dielectric around the conductive filler particles.

6.3. Fabrication of the device

The polymeric nanocomposite was carried out using $PS@TiO_2$ as filler. After device preparation, its electrical behavior was measured.

6.3.1. Thin films deposition

Different amounts of $PS@TiO_2$ powder and commercial polystyrene Mi14 (Mn = 73850; Mw = 167330; PDI = 2.26) were dispersed in 1 ml of chloroform and dichlorobenzene 1:1 v/v solution and the relative concentration (Table 11), reported as $PS@TiO_2$ volume fraction, was calculated using 1.04 g cm^{-3} and 4.17 g cm^{-3} as PS and rutile density, respectively. In order to guarantee an appropriate dispersion during the deposition process, the suspensions underwent ultrasound treatment for 60 min.

Sample	$PS@TiO_2$ (mg)	PS-Mi14 (mg)	TiO_2 % Vol	Total PS % Vol
1	230	0	64.1	35.9
2	180	18	49.5	50.5
3	135	34	36.9	63.1
4	95	48	28.9	71.1
5	65	59	19.7	80.3
6	35	70	11.1	88.9

Table 11. Amounts of $PS@TiO_2$ and commercial PS used to prepare composites at different concentration. The relative volume fractions are calculated using 1.04 g cm^{-3} and 4.17 g cm^{-3} as PS and TiO2 density, respectively.

A micrometric film was obtained through blade coating deposition on a Cu substrate that constitutes the lower contact. The solvent was evaporated for 72 hours at RT and the upper contact was realized via Au sputtering deposition using two circular masks of 15.46 ± 0.05 mm and 4.95 ± 0.05 mm in diameter. The choice of the copper substrate and a gold contact were dictated by the need to obtain a homogeneous distribution of the charges to the surface of the dielectric at the time of measurement. The resulting device, modelled as a parallel and flat plate capacitor (Figure 66), was annealed at 140°C under nitrogen for 4 hours before dielectric characterization.

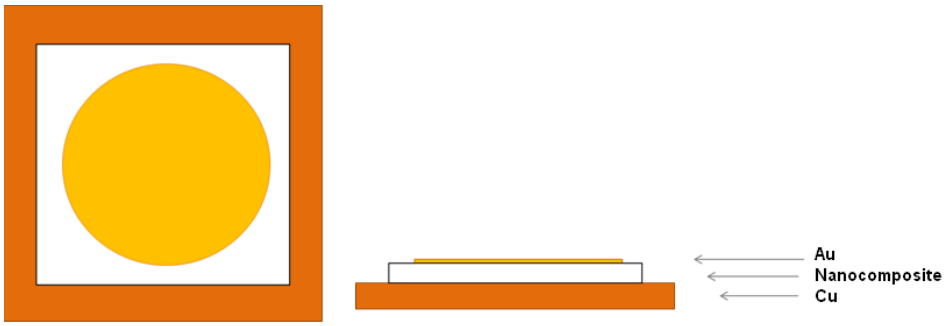

Figure 66. Representation of device, the copper substrate and the gold layer deposited by sputtering represent the contacts of the dielectric film.

6.3.2. Microscopic analysis

Because of the importance of the geometry in the electric measurements, care was taken in measuring the film thickness. For this purpose each film was cut close to the gold spot, used as electrode, and the cross-section was measured by SEM.

Figure 67 shows the SEM images of samples with greater area, because those with smaller area are constructed around from the same film in that

determined composition. Table 12 reports the film thicknesses for samples with masks of 15.46 ± 0.05 mm and 4.95 ± 0.05 mm in diameter, therefore having area 188 ± 1 mm^2 and 19.2 ± 0.4 mm^2 respectively.

In all the films a compact section is observed and a good thickness uniformity, particularly when the fraction of contained nanoparticles is low. An estimate of the thickness was made through the SEM image, Figure 68. The thickness measured graphically is affected by an error estimated at around 5%, which has a significant impact on the final value of the permittivity.

Sample	**1**	**2**	**3**	**4**	**5**	**6**
Thickness for 188 mm^2 disk (μm)	65	64	51	48	30	32
Thickness for 19.2 mm^2 disk (μm)	73	41	54	48	30	32

Table 12. Film thicknesses of the samples with area 188 mm^2 and 19.2 mm^2.

The morphological features of the composite material at different filler loading were investigated by TEM microscopy and are reported in Figure 69. At low filler concentrations (19.7% v/v) the rutile nanoparticles are well dispersed into the polystyrene matrix (Figure 69A). By increasing the rutile concentration (Figure 69B and C) the images reveal the formation of some chestnut-burr aggregates well detectable in Figure 69D and typical of rutile nanorods.[147] On close examination of the rod aggregation (Figure 65) it is evident that a thin polymeric shell (3.7 nm) intercalates with the lateral shared faces of the rutile crystals, which form the aggregates. At the highest filler loading, 64.1% v/v, the aggregates have the tendency to further assemble in large agglomerates.

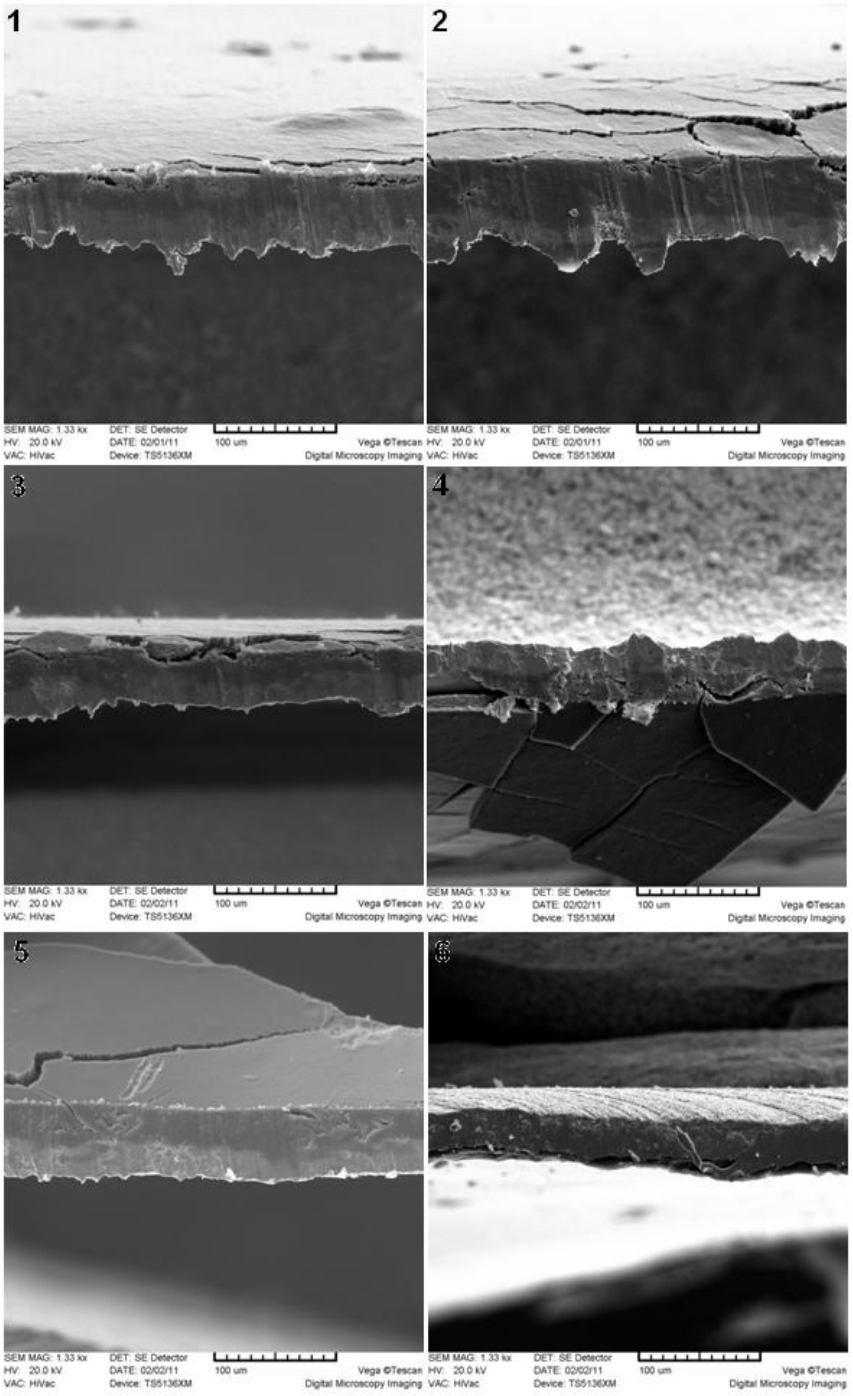

Figure 67. SEM cross section of all sample with mask area 188 ± 1 mm^2.

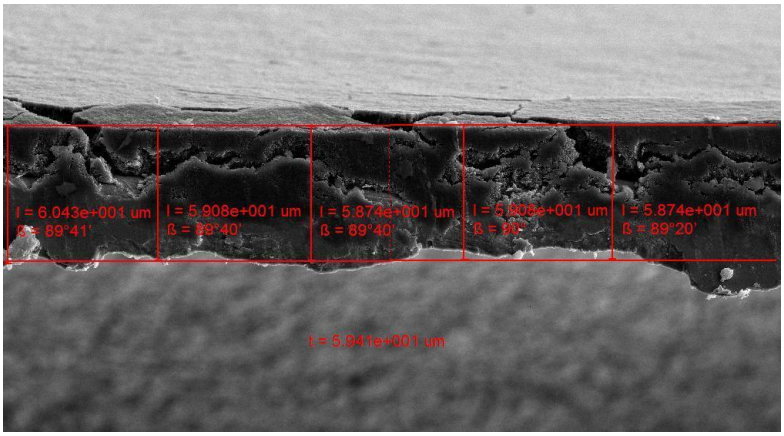

Figure 68. SEM cross section of the PS@TiO_2 composite film (36.9 % TiO_2, sample 3) used for electric mesurements.

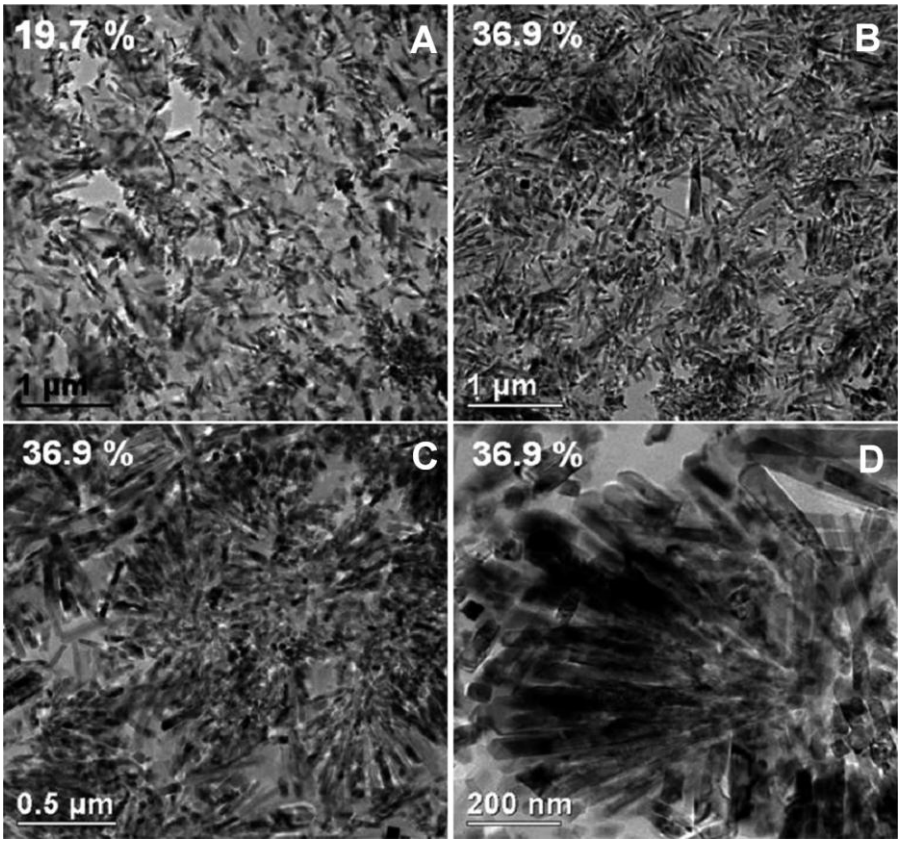

Figure 69. TEM micrographs of the PS@TiO_2 composites at different TiO_2 contents (19.7%, 36.9% and magnifications).

6.4. Dielectric characterization

The effective dielectric constants of PS@TiO_2 film were obtained from the measurements of capacitances C using the equation 13:

$$\varepsilon_r = \frac{Cd}{\varepsilon_0 A} \qquad (13)$$

where d is the film thickness, A is the area of the gold spot and ε_0 = 8.854 * 10^{-12} F m^{-1}. The impedance measurements were performed using a HP 4282A Precision LCR Meter in configuration Cp-G. The maximum tension was 1 V while the frequency varied between 20 Hz and 1 MHz.

In Figure 70, the trend of ε_r and $tg\delta$, with the frequency for each of the six films at different concentrations, were reported. The measures are average of the values obtained at each frequency for the two samples with different area. A film consisting only of polystyrene with the same procedures of preparation of the samples was made and characterized. The value of permittivity obtained ($\varepsilon_r = 2.87$) was unchanged over the entire range of frequencies, but differs significantly from the theoretical[148] average value at 1 kHz: $\varepsilon_r = 2.49/2.55$.

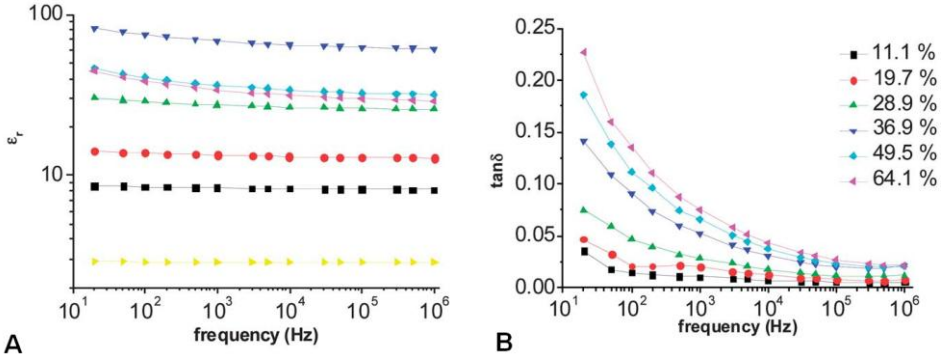

Figure 70. Spectral impedance characteristics of the PS@TiO_2 composites with different TiO_2 loading. a) the relative dielectric constant, b) the dissipation factor were plotted vs. the frequency. The yellow curve in (a) was the measured ε_r of the commercial PS.

This difference and the errors introduced by the experimental procedures (measurement of thickness and areas) give a total error on the final values of permittivity of about 10%.

By the values of conductance G is also possible to obtain the trend of the conductivity varying the frequency. Bilogarithmic scale have been growing linearly with the frequency, which has a maximum at a concentration of 36.9% by volume of TiO_2 (Figure 71).

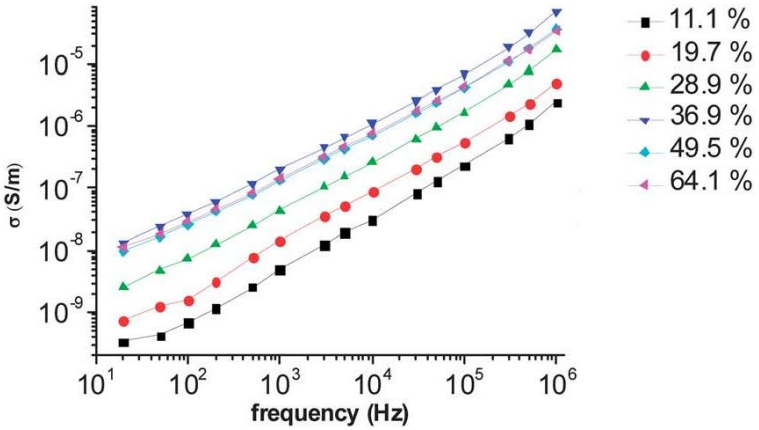

Figure 71. Spectral impedance characteristics of the PS@TiO_2 composites with different TiO_2 loading, the conductivity were plotted vs. the frequency.

In Figure 72 the values of the dielectric constant ε_r, measured at 104 Hz for the different filler concentrations, are reported. The relative dielectric constant rises with the TiO_2 content. In order to extrapolate the percolation threshold and the q exponent, the experimental data were fitted according to eq 10 (plot in Figure 72). The obtained values were: q = 1.09 ± 0.04 and v_c = 41 ± 1% v/v of TiO_2 for the percolation threshold. The percolation threshold is indicated with a dashed line in Figure 72. This value is 17% higher than those reported in the literature[25,149] for similar systems and close to 40% reported by Bhadra et al.[150] It can be observed that when the matrix is a polymer and behaves as a continuous

host embedding the filler, the percolation threshold depends mainly on the filler shape and dimensions.[151,152] In our case none of the morphologies reported in the literature allow appropriate comparison, as the electrical properties of our composite are related to the special chestnut burr morphology which favors at the same time both aggregation and separation of rutile particles.

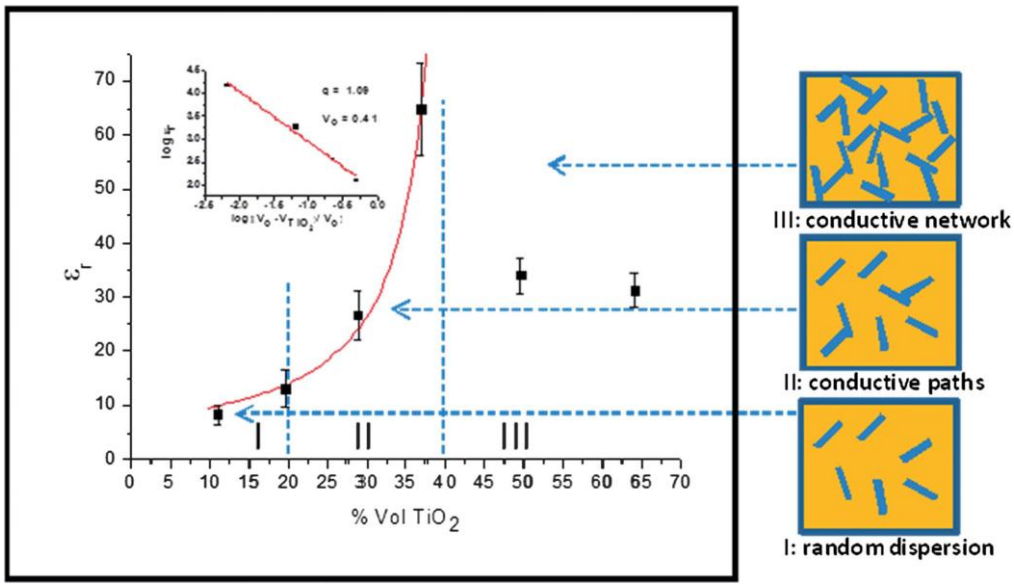

Figure 72. Variation of the dielectric constant of the PS@TiO_2 composite vs. the volume fraction of TiO_2 at 10^4 Hz. The inset shows the fitting of the 3r to eq 10 using q, v_c and c as adjustable parameters. The schemes on the right represent the composite microstructures by increasing the TiO_2 concentration.

Following the conductivity a potential law analogous to eq 10, the percolation threshold and the q value can be calculated by plotting the conductivity of the composite vs. the filler loading (see Figure 73). The obtained values for the exponent and percolation threshold were: q = 1.17 ± 0.06 and v_c = 39 ± 2% v/v. The values are in reasonable agreement with the corresponding values obtained by plotting the dielectric constant.

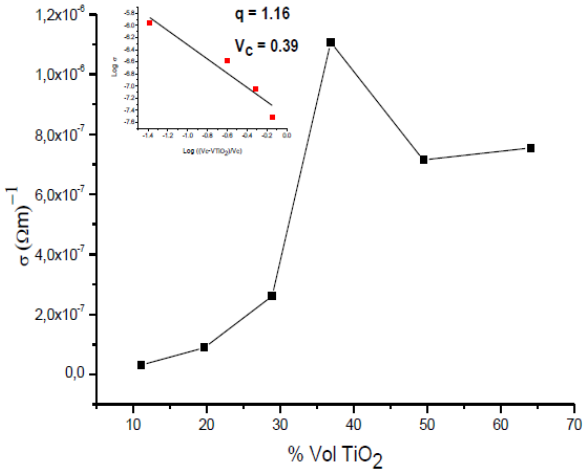

Figure 73. Variation of the conductivity of PS@TiO_2 composite vs. the volume fraction of TiO_2 at 10^4 Hz. The inset shows the fitting of the σ to the Eq.10 using q, v_c and c as adjustable parameters.

According to the percolation theory, as the TiO_2 content approaches the percolation threshold ($v \rightarrow v_c$), the conductivity and the dielectric constant depend on the frequency according to:

$$\sigma \sim \omega^u \qquad (14)$$

$$\varepsilon = \omega^{u-1} \qquad (15)$$

where ω is the frequency and u is a critical exponent with a value close to 1.[153]

Following eq. 15 the conductivity increases with the frequency while it becomes independent when the u value approaches 1. The plot in Figure 70a reports the ε_r values at different filler concentrations vs. the frequency. It appears that ε_r is quite independent from the frequency up to a filler concentration of 36.9% v/v, which is the maximum concentration below the percolation threshold. After the percolation threshold the slope of the curves, especially at lower frequencies, slightly increases. The u values are 0.99 ± 0.04 and 0.98 ± 0.04 for TiO_2 concentrations of 11.1 % and 36.9 % respectively.

The plots in Figure 70b report the conductivity values, for the different filler concentrations, against the frequency. The u values calculated by fitting the curves between 10^3 and 10^6 Hz, avoiding the distortion in the low frequencies range, are 0.88 ± 0.08 and 0.84 ± 0.08 for 11.1 % and 36.9 % concentrations, respectively. The obtained values calculated by dielectric and conductivity measurements have a good matching considering the standard deviations. The good fits of the impedance experimental data confirm the validity of the application of the percolative model to this PS@ TiO_2 composite material.

In Figure 71 the plots of tanδ at different filler concentrations against the frequency are reported. The trend of tanδ shows the typical increase approaching the percolation threshold (e.g. from a titania content of 28.9 % to 36.9 %). Nevertheless, the values of tanδ below the percolation threshold are always lower than 0.10, also at the lowest frequencies. The low tanδ values can be explained by the dense and homogeneous (see Figure 69) brush-like polymer film, which totally covers the TiO_2 particles. In fact, this polymeric shell creates a dense insulating layer able to lower the mobility of the charge through the material by increasing its resistance. Consequently, below the percolation threshold, this results in a low resistive current which assures low dielectric loss and low energy dissipation.

The percolative behavior of the electrical properties in the composites can be rationalized in connection with the morphology of the composite material as the TiO_2 amount increases.

At the low concentration of TiO_2, the slight enhancement of the dielectric constant is caused by the increase of the filler content (region I in Figure 72) in accordance with the classical mixing formulae.[154] In Figure 74 we report the plot of the three mostly used mixing formulae which predicts the electrical properties of the composites upto a concentration of 19.6% v/v. The formation of these aggregates corresponds to a sudden increase of the dielectric constant (region II in Figure 72). Thus, applying the dielectric percolation theory,[36] we can ascribe

to these aggregates the origin of the microcapacitive structures responsible for the increase of the dielectric properties. The intrinsic rutile tendency to aggregate suggests that the shape of rutile crystals is well suitable to stabilize the microcapacitive structures formed by the rods and by the intercalation of a thin polymer layer between the crystals (Figure 65). Under an electric field the carrier displacement takes place and the induced polarization of the microstructures causes the large dielectric constant. This tendency of rutile to self-assemble in non-interconnected chestnut-like aggregates explains the high value of the percolation threshold. After the percolation threshold (filler concentration > 41%) the number of chestnut-like aggregates increase. The aggregates now become interconnected with each other and form the percolative network, which causes the sudden change of the dielectric characteristics (region III in Figure 72).

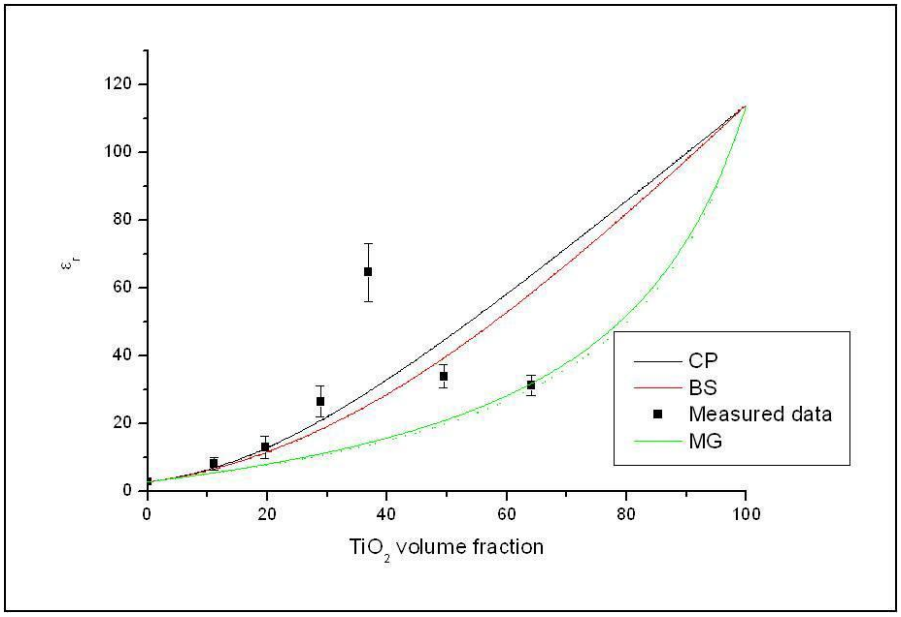

Figure 74. Experimental values of the dielectric constant of PS@TiO_2 composites at different filler loading. Curves represent the best fit according the mixing formulae in reference 18 (CP = coherent potential, BS = Bruggeman symmetric, MG = Maxwell Garnett).

6.5. Conclusion

A new polymeric–inorganic nanocomposite material was prepared, which exhibits very high dielectric constant and high percolation threshold. For this purpose, a shell of polystyrene on TiO_2 has been grown via RAFT technique employing the "grafting from" approach. The best conditions for growth have occurred with S-1-Dodecyl-S'-(α,α'-dimethyl-α''-acetic acid) trithiocarbonate, in bulk at 110 ° C for 96 h with [M]/[T] = 7200. Capacitors were realized with six different concentrations of filler and tested for electrical properties.

The origin of the high dielectric constant can be ascribed to the assembling of rutile nanoparticles in chestnut-like aggregates, where a number of core–shell rutile crystals share their faces and form capacitive microstructures. These aggregates separated by a thin layer of polymer allow the high increase of the filler amount up to 41% v/v avoiding the formation of the continuous network responsible for the sudden change of electrical characteristics. The self-assembling properties of the rod-shape rutile are reproducible and this favors the reproducibility of the electrical properties.

Despite the high content of inorganic fillers, the dissipation factor remains low, even approaching the lower frequencies. The low tanδ values in a large range of frequencies allow us to candidate the material for radio frequency (RF) applications where very low dissipation factor is desired to avoid signal losses.

Chapter 7. Functionalization of SiO_2 with PI for application in tyres

In this chapter I will present the functionalization of commercial SiO_2 nanoparticles with diene polymers with the aim to increase their compatibility with the polymer phase of tyres. The synthesis procedure is the same as the one carried out on TiO_2 (grafting from polymerization RAFT), but I changed the transfer agents and the polymers anchored to the surface. After studying the functionalization with three different RAFT agents (DDAT, BTmePT, BTetPT), the polymerizations of styrene and isoprene were performed. Since a good polyisoprene coating was obtained, scaling-up of the process was developed and the product was tested in polymeric compounds. All the work was carried out with particular care to the possible application in tyres.

7.1. Introduction

Tyres must satisfy a wide range of performance requirements. They must carry the load of the vehicle, have sufficient grip on the road, transmit steering forces to guide the vehicle, provide dampening between the road and the vehicle, have durability that enables their use at high speeds and over long time periods, and be fuel-efficient (related to rolling resistance). Tyres are complex composites made of mixtures of rubber with metal and textile reinforcements.[155] The rubber mixtures or compounds are mainly composed of polymers, reinforcing fillers, oils, and numerous chemicals used to crosslink or "vulcanize" the compounds. Different rubber compounds exist for the various parts of a tyre, each with a specific combination of materials to provide the performance attributes for that

part. The first polymer used was natural rubber, 1,4-cis-polyisoprene, but due to the need to adjust the performance of the tyres, synthetic rubbers such as BR (Butadiene Rubber), SBR (Styrene Butadiene Rubber), and different copolymers were introduced. To control the stiffness of the blend and add greater workability, softeners such as resins and hydrocarbon oils are introduced in small quantities. In addition, chemicals such as para-phenylenediamine (PPD) are used to protect the tyres against heat, oxygen and ozone. A very important component is represented by materials that allow the process of vulcanization or cross-link, enabling the polymer chains to bind via chemical bridges that increase the elastic properties of the system: the most common are sulfur and sulfenamides. Activators and accelerators of vulcanization are introduced to adjust the process, as stearic acid and Zinc oxide. Finally, there are reinforcing fillers such as carbon black, silica, clay and titanium dioxide.

The reinforcing fillers used in tyre compounding are critical to achieving the performances required. This is especially true for the tread compound with its large number of requirements and emphasis on wear resistance. The fillers provide a large degree of strengthening of the rubber network, resulting in a substantial increase in stiffness, tensile strength, and resistance to abrasion[156]. The reinforcing fillers achieve this via a high level of chemical links with the polymer network. The primary result of this strength improvement is the longevity of the tyres, in terms of overall load bearing, durability, and tread wear performance[157]. A tyre manufactured without the use of reinforcing fillers would not be strong enough to carry the load or handle the forces required by the vehicles of today. Without reinforcing fillers, tyres would need to be replaced considerably more often, resulting in an increased burden on end-of-life-tyre (ELT) management and an increase in tyre manufacturing energy requirements and greenhouse gas emissions per vehicle kilometer driven.

The primary reinforcing fillers used for the production of rubber articles are precipitated amorphous silica and carbon black. This work is focused on

silica. Amorphous precipitated silica, defined by a specific CAS number, is used in many applications in addition to its use in the rubber and tyre industry, including cosmetics, paper and many other applications related to nutrition and health[158]. The world production of amorphous precipitated silica is 1.3 million tons of which one-third is used in tyre production. Silica has been used in the treads of tyres for more than twenty years in order to reduce the fuel consumption of vehicles, thus contributing to a reduction in vehicle emissions of greenhouse gases[159].

Amorphous precipitated silica is produced from vitreous silicate. The vitreous silicate is dissolved in water and transferred to a reactor in which, through acidification and under agitation, amorphous silica is precipitated out. During this precipitation there is an instantaneous formation of primary nanoscale particles (from approximately 2 to 40 nm) of a very short lifespan. However, these particles immediately cluster to form non-dissociable aggregates (from approximately 100 to 500 nm in size) based on covalent bonds. Because of the nature of these bonds, these aggregates cannot disaggregate under standard conditions. The aggregates subsequently electrostatically bind together to form agglomerates from 1 to 40 μm. Electrostatic bonds, while weaker than covalent bonds, cannot be broken from normal use: breaking these bonds requires the use of a dispersant. Because of these aggregates and agglomerates, precipitated amorphous silica is a nanostructured material, even if each agglomerate does not meet the definition of nanoparticle. At the end of the precipitation process, after drying and washing, the precipitated amorphous silica is mechanically processed into micro pearls or granules (dimension of 1/10 mm to a few mm) to ease shipping, handling and use. It is this form that is used by the tyre industry. The formation of these micro pearls and granules reduces the dustiness of the precipitated silica, and therefore reduces the potential for worker exposure to particles of amorphous silica during handling. During rubber compounding, due to the high energy involved, the granules or micropearls of the precipitated silica

are broken down, transforming back to the aforementioned agglomerates with dimensions between 1 and 40 microns. Because of the strong mechanical energy applied to the rubber, agglomerates may be broken down and transformed into aggregates, some of which are of nanometric size (their dimension ranges between 100 to 500 nanometers).

However, it is crucial to understand that these aggregates are chemically bound to the rubber matrix by strong chemical links that result from the manufacturing process. Furthermore, the physical mixing process itself does not create enough energy to break down the strong covalent forces that exist between the individual particles that form these aggregates[160]. Agglomeration is also driven by incompatibility between inorganic silica surface and the organic matrix. Consequently, to obtain well dispersed silica inside the tyres using the precipitated silica already existing on the market, you have to modify the surface to prevent agglomeration. A possible way to do this is to functionalize the surface. As mentioned in the introduction, the ways for this task are of different chemical and physical nature, the method taken into consideration in this work is to create a shell of polyisoprene (same polymer matrix) to make sure that the surface of the nano particles are energetically discouraged to agglomerate.

7.2. Synthesis of SiO_2 with different RAFT agents

Commercial SiO_2 (Ultrasil 7000 GR, Evonik) with a particle size of about 25 nm and a specific surface area of 170 $m^2\ g^{-1}$ (measured by BET) was chosen as solid support.

Following the results obtained with nanoparticles of TiO_2 (Chapter 6) silica was functionalized with DDAT, which is seen to have a good polymerization efficiency. SiO_2 with two RAFT agents with silanic functionality that form covalent bonds with the surface of the nano particles, BTmePT and

BTetPT, were then tested. The former, which is stable and simple to produce, was mainly used to study the coating surface density at varying transfer agent/silica ratio. Since the reaction with the methoxy silane produces methanol, considered undesired at an industrial level, RAFT agent with ethoxy silane was tested.

7.2.1. Synthesis of DDAT@SiO_2

To a 250 mL two-necked flask 5 g of SiO_2 and 40 ml of toluene were added and the water was removed by azeotropic distillation. The nanoparticles were dried with mechanical vacuum. Via cannule, a solution of 50 ml of methanol and 2.5 g (6.87 mmol) of DDAT trithiocarbonate was added. The suspension was kept for 96 hours in the dark under stirring at room temperature under argon. The particles were recovered by centrifugation (30 min at 6000 RPM). In order to remove the unreacted CTA and the residual traces of methanol, the powder was washed for 20 minutes under ultrasound conditions with ethyl acetate (3 times with 50 ml) and CH_2Cl_2 (3 times with 50 ml). The final wet powder was dried in air at room temperature and the residual solvent evaporated under vacuum overnight.

The surface density of coating of the RAFT agent on the SiO_2 was determined by TGA (Figure 76) and sulfur elementary analysis. As in the case of the TiO_2 the bond formed between the carboxylic acid moiety and the surface can be considered as intermediate between a dative covalent bond and an ionic bond.

Following a procedure similar to Chapter 6, a blank measurement was carried out on a sample of silica, to be able to subtract the curve obtained from the subsequent measurements on functionalized nanoparticles. Therefore the weight losses were measured between 150 ° C and 600 ° C. From the measured weight loss of 1.18%, the amount of grafted RAFT in the -DDAT@SiO_2 agent was evaluated to be 0.035 mmol g^{-1}. Assuming that the molecules were evenly

distributed on the surface and referring to the surface area of SiO_2 170 m^2 g^{-1} (measured by BET), the number of molecules per nm^2 resulted to be 0.5 DDAT per nm^2. The average distance between the molecules anchored to the surface is 3.2 nm. The sulfur elementary analysis revealed that the RAFT agent loading was 0.95 %, which is comparable to the results estimated by TGA.

Therefore the overall coating level of silica surface, maintaining the same reaction conditions, results to be lower than in the case of the nano particles of TiO_2. One possible explanation for this phenomenon is due to the different chemical and morphological nature of the surface of SiO_2.

7.2.2. Synthesis of BTmePT@SiO_2 and BTetPT@SiO_2

The functionalization of the silica with the two RAFT agents with siloxane functionality was performed with similar procedure of Perrier et al.[161] (see Figure 75). In a 500 mL three-necked flask with septum, 8.0 g of silica and 200 mL of toluene were mixed with magnetic stirring and ultrasound at room temperature for 30 min. Water was removed by azeotropic distillation. A solution of RAFT agent (see Table 13) and 50 mL of dry toluene was added into the flask under argon. The reaction mixtures were heated to reflux overnight (about 16 hours) in argon atmosphere. After cooling, the suspension was recovered by centrifugation (60 min at 6000 RPM) and was washed for 20 minutes under ultrasound conditions with CH_2Cl_2 (5 times with 100 ml). After drying at 60 °C under vacuum overnight, grafted silica particles (BTmePT@SiO_2 or BTetPT@SiO_2) were obtained as deep yellow solid products. The residual was recycled and used further for the synthesis.

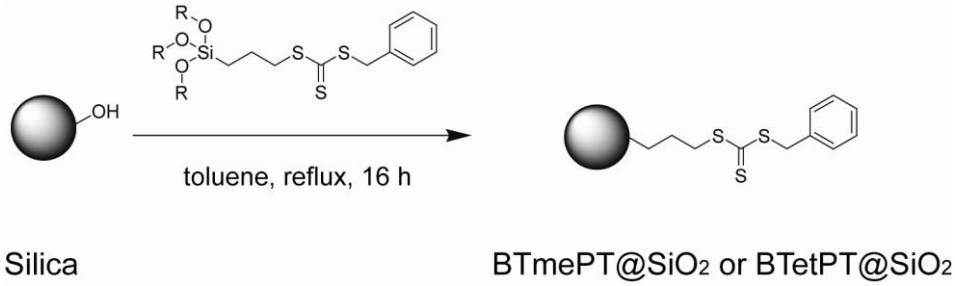

Figure 75. Scheme of reaction of SiO_2 with RAFT agents BTmePT and BTetPT, where R = CH_3 and CH_2CH_3 respectively.

Sample	RAFT agent	Ratio g_{agent}/g_{SiO2}	% (TGA)	% ($S_{elementary}$)	molecules/nm^2
DDAT@SiO_2	DDAT	0.5	1.18	0.95	0.12
BTmePT_1@SiO_2	BTmePT	1.00	6.48	7.41	1.02
BTmePT_2@SiO_2	BTmePT	0.30	5.83	6.21	0.91
BTmePT_3@SiO_2	BTmePT	0.15	5.29	5.72	0.82
BTmePT_4@SiO_2	BTmePT	0.10	4.83	5.49	0.75
BTmePT_5@SiO_2	BTmePT	0.05	2.64	3.38	0.40
BTetPT@SiO_2	BTetPT	0.40	4.28	4.13	0.66

Table 13. Reaction conditions and density of the coating surface of SiO_2 with RAFT agents.

The purpose of this analysis was to determine the least amount of reagent needed to obtain a good coating surface to be used for the polymerization. In order to understand what was the maximum coating, under these reaction conditions, in the first sample (BTmePT_1@SiO_2) a large excess of reagent was used.

Varying the amount of RAFT agent with respect to the silica a non-linear variation of the coating surface of the nanoparticles is found. As can be seen from Table 13 a large excess of RAFT agent does not lead to a higher silica

loading. Therefore it can be established that the sample where the ratio of RAFT agent/SiO_2 (BTmePT_2@SiO_2) was 0.30, was the best compromise to obtain a good surface covering and a moderate consumption of reagents.

The functionalization with BTetPT shows a different result compared to BTmePT, this phenomenon can be explained by two reasons. The molecule has a greater steric hindrance, that blocks anchoring sites.

7.3. Raft polymerization mediated by CTAs@SiO_2

Before studying the functionalization of the silica with isoprene, the behavior of the polymerization of styrene in conditions similar to those used with TiO_2 (Chapter 6) was evaluated.

7.3.1. Styrene polymerization

In a 100 ml schlenk tube with septum 200 mg of SiO_2-DDAT were kept at reduced pressure for 4 hours before the addition 2.77 ml of styrene (23.9 mmol, [M]/[T] = 3500) over argon. The suspension was homogeneously dispersed by ultrasound treatment and four freeze–pump–thaw cycles were performed to remove the oxygen dissolved in styrene. The RAFT polymerization was carried out at 110 °C for 96 h under an argon atmosphere with magnetic stirring. The polymerization was interrupted by quenching in liquid nitrogen. To separate SiO_2–PS from the ungrafted polystyrene, the solid was dissolved in CH_2Cl_2 (80 ml) and the particles were separated by centrifugation (6000 RPM for 30 min). The recovered particles were washed three times with CH_2Cl_2 under ultrasound conditions, separated by centrifugation and finally dried in a vacuum overnight at 40 °C (PS1@SiO_2). With the same procedure, PS2@SiO_2 and PS3@SiO_2

samples were synthesized with a monomer/CTA ratio equal to 7000 and 14000 respectively (see Table 14).

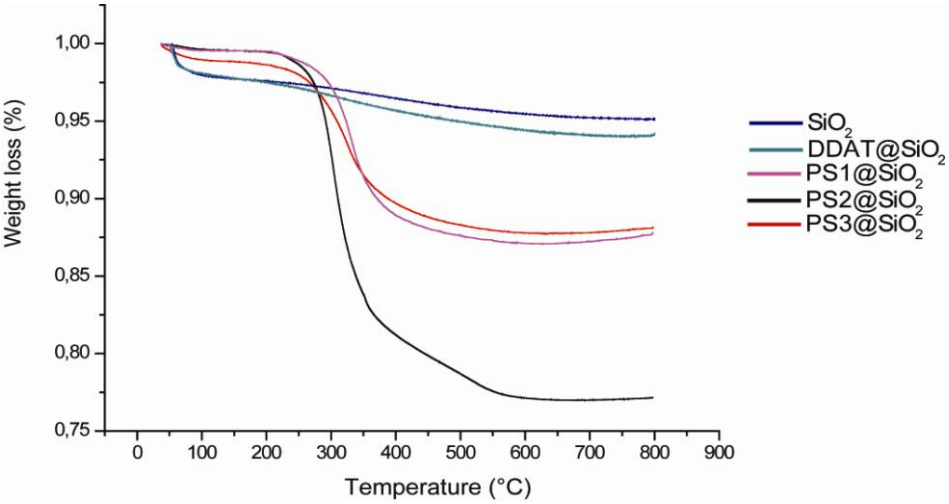

Figure 76. TGA measurements of grafting form RAFT polymerization on SiO_2-DDAT.

Sample	[M]/[T]*1000	weigth loss %	N.u.m.[a]
PS1@SiO_2	3.5	11.10	35
PS2@SiO_2	7.0	21.36	76
PS3@SiO_2	14.0	9.87	31

Table 14. Synthesis parameters and TGA analysis of the RAFT polymerization of polystyrene on SiO_2. [a] N.u.m. is the number of monomer units constituting the chain.

The dependence of the degree of polymerization from [M]/[T] ratio were calculated using TGA analysis (Figure 76). The chain length, *i.e.* the number of monomer units (n.u.m), was estimated in according to the procedure of chapter 6.

As is shown from Table 14 the degree of polymerization of polystyrene is very high compared to the samples of TiO_2. The sample PS2@SiO_2has a number

of repeat unit equal to 76 and then an estimated molecular weight of about 7900 g mol^{-1}. This is due to the fact that the loading surface of RAFT agent of the silica particle is of an order of magnitude lower than that of the titania. Then, during growth the polymer has a lower steric hindrance and an increase in the probability of the free radical to recombine with the growing chain.

Although three points are insufficient to delineate a trend, a behavior similar to PS@TiO_2 is noticed, concerning the relationship between the degree of polymerization and the [M]/[T] parameter. Therefore, there is a point where the monomer is in excess and the formation of free polymer lowers the probability of recombination of radicals of the polymers in growth, slowing down the process of polymerization.

7.3.2. Isoprene polymerization

All polymerizations with isoprene were conducted in solvent and with AIBN as a radical initiator (I) as reported in the literature. In fact styrene, thanks to its high reactivity, is the only monomer used in bulk and without radical initiator.

In a 100 ml schlenk tube with septum 200 mg of DDAT@ SiO_2 were kept at reduced pressure for 4 hours. 15 ml of 1-4,dioxane were added over argon and the suspension was homogeneously dispersed by ultrasound treatment. After adding of 0.345 ml (3.5 moml, [M]/[T] = 500) of isoprene and a solution of 1-4,dioxane and AIBN ([T]/[I] = 2) via cannule four freeze–pump–thaw cycles were performed. The reaction was carried out at 110 °C for 22 h under an argon atmosphere with magnetic stirring. The reaction was interrupted by quenching in liquid nitrogen and the recovered particles were cleansed with the same procedure previously carried out. The sample called PI1@SiO_2 was analyzed with TGA registering a weight loss equal to 3.04 % and therefore a 13 monomer unit for chain.

Given the positive results of the sample PI1@SiO_2, polymerization of isoprene was carried out on BTmePT_2@SiO_2.

Maintaining the solvent (dioxane) and the reaction temperature (110 ° C), the ratio monomer RAFT agent on the surface ([M]/[T]), the ratio RAFT agent-initiator ([T]/[I]) and the reaction temperature were varied. Furthermore a RAFT agent not bonded to the surface (BPTT) was introduced in solution (CTA free).

Sample	**[M]/[T]**	**$t_{reaction}$ (h)**	**[T]/[CTA Free]**	**[T]/[I]**	**loss %**	**N u.m.[a]**
PI2@SiO_2	500	22	-	2	6,01	3
PI3@SiO_2	500	48	-	2	6,58	4
PI4@SiO_2	1000	48	-	2	6,90	4
PI5@SiO_2	500	22	0,5	2	5,55	3
PI6@SiO_2	1000	22	0,5	2	8,65	5
PI7@SiO_2	1000	22	-	2	4,87	3
PI8@SiO_2	1000	72	-	2	4,05	6
PI9@SiO_2	500	48	-	2	2,21	3
PI10@SiO_2	500	48	-	2	4,10	6
PI12@SiO_2	3000	48	-	2	6,72	4
PI13@SiO_2	1000	72	-	2	5,52	3
PI14@SiO_2	1000	48	-	5	7,86	4
PI15@SiO_2	500	48	-	5	9,87	6
PI16@SiO_2	500	48	-	5	10,10	6

Table 15. Synthesis parameters and TGA analysis of the RAFT polymerization of isoprene on BTmePT_2@SiO_2. [a] N.u.m. is the number of monomer units constituting the chain.

In a typical run, in a schlenk tube with septum 200 mg BTmePT_2@SiO_2 (288 μmol) were dried in mechanical vacuum for 2 hours. 0.47 ml of a solution

0.6 M of AIBN and 0.2 ml of a solution 1.3 M of BPTT both in 1-4,dioxane were added under argon. After stirring 2.88 ml (28.7 mmol, [M]/[T] = 500) of isoprene and 1-4,dioxane were introduced. After adding a magnetic stirring bar and ultrasonic treatment, the tube was subjected to three freeze-pump-thaw cycles to remove oxygen. The tube was placed into an oil bath preheated to 60 °C for 18 h and then the polymerization was quenched by putting the tube into a liquid nitrogen bath. The recovered particles were cleansed with the same procedure previously carried out and were analyzed by TGA. All other samples were synthesized by the same procedure by varying the parameters as indicated in Table 15.

The RAFT polymerization via grafting of isoprene on BTmePT_2@SiO_2 did not produce a high degree of polymerization with variation of these parameters. The number average of unit monomer varies from 3 to 6, therefore the polymeric chains can be considered oligomers. However, the coating of the nanoparticles is high because the silica used has a high density of functionalization. The sample PI15@SiO_2 has a quantity of polyisoprene bonded to the surface equal to 10.1%.

The parameters of polymerization to obtain a polymer with higher molecular weight were found to be the ratio [M] and [T] equal to 500, with five times the amount of CTA compared to radical initiator for 48 h. The free CTA, unexpectedly, does not seem to influence the process as supported by Perrier et al. Probably, the dense surface coating of BTmePT causes a too high steric hindrance during polymerization. Another explanation could be both the type and the quantity of solvent used.

7.4. Nanocomposite

To obtain a compound comparable to those of standard tyres, 75 g of RAFT agent-functionalized SiO_2 were synthesized and functionalized with

isoprene under the same condition of the sample PI15@SiO_2. It was therefore necessary an up-scaling of the polymerization process. Approximately 80 g of BTmePT_2@SiO_2 were synthesized starting from 81 g of precipitated silica. After checking through TGA and elemental sulfur analysis, 15 g of silica functionalized and proportional quantities of reagents (isoprene, AIBN) were placed in a 1000 ml schlenk tube. It was possible to reduce the reaction solvent (1-4,dioxane), for the good dispersion of the nanoparticles within the monomer. The reaction was carried out in an isolated system with a highly efficient reflux under argon. This prevents that, during heating, not yet reacted isoprene went into boiling. Once the system was quenched as usual, the particles were washed with the procedure previously used and analyzed to ensure the successful reaction. The reaction was carried out five times to obtain the necessary amount to formulate the compound. The sample was called PI@SiO_2.

	low density (phr)			high density (phr)		
	raf-1	raf-2	raft	raf-1	raf-2	raft
NR	100.00	100.00	100.00	100.00	100.00	100.00
Silica ULTRASIL 7000	11.00			32.00		
PI@SiO_2		11.00	11.88		32.00	34.56
TESPD		0.88			2.56	

Table 16. Compounds with low and high density with corresponding references, ref-1 represents the sample with only silica, ref-2 also with compatibilizer.

Two series of compounds were mixed with about 11 and 32 phr (parts per hundred of rubber) of functionalized silica, low and high density respectively. For each series were performed two different references: the first containing only silica and the second containing silica and silane (TESPD-266), in an amount

proportional to the silica, and close to the organic matter of the sample PI@SiO_2 (10.1 %). As reference was used Silica ULTRASIL 7000.

In a typical run, 162 g of natural rubber (NR-STR 20 P 93) and 19.12 g of PI@SiO_2 were added in a closed mixing chamber (thermo Haake rheomix lab station). After 7 minutes of mixing and reaching 140 °C, the resulting "first phase compound" was discharged and cooled. After 24 h, the "first phase compound" was mixed in the same equipment with 3.12 g of stearic acid, 3.9 g of N-(1,3-Dimethylbutyl)-N´-phenyl-1,4-phenylenediamine (6PPD) and 5.46 g of zinc oxide (RHENOGRAN ZnO 80% active) for 4 minutes. The product was cooled and mixed with 4.56 g of N-Cyclohexyl-2-benzothiazole sulfenamide (CBS) and 1.52 g of sulfur for 2 minutes in an open two-roll mill. The other compounds were obtained with similar procedure varying only the type of silica and the presence of silane (see Table 16) in the first step. The sample with 32 phr were mixed in first stage for 6 minutes because the compound produces more heat, In addition was visible a better homogeneity of the product.

Conclusions

In this thesis I exploited RAFT polymerization technique to develop different macromolecular architectures. The topics addressed have been the synthesis of block copolymers and the surface modification of nanoparticles of metal oxides.

Several PS-b-PDMA copolymers were synthesized for controlled self-assembly in aqueous solution, introducing a new non-invasive method for determining the viscosity of micro-nano structures. In particular, I have analyzed two polymers with different block lengths. PS_{105}-b-$PDMA_{817}$ presents a micellar morphology with a hard core of polystyrene and a solvated shell of PDMA. Instead, PS_{62}-b-$PDMA_{10}$ exhibits a complex morphology whose determination required more effort. From the data obtained, a granular morphology with nanoparticles agglomerated in a superstructure of 200-300 nm is hypothesized.

PS-b-PEO-b-PS copolymers were synthesized and used as polymer gel for the manufacture of Quasi Solid-State Dye-Sensitized Solar Cells. The polymers were placed in standard cells as a support for the liquid electrolyte, producing a gel matrix. Measurements of electrical conductivity show a efficiencies of 6.7% which are comparable to that of the standard electrolyte DSSC (6.9 %). Moreover, improved stability was observed: a device kept for 15 days under outdoor conditions with sunlight and climate stress has shown unvaried power conversion efficiency. Therefore this new polymeric host electrolytes could be of interest for a new generation of quasi solid-state DSSC, especially for the good mechanical properties and high tunability of physico-chemical characteristics.

Nanoparticles of TiO_2 have been functionalized with polystyrene to produce core-shell particles. New polymeric nanocomposite with potential application as high dielectric material can be prepared staring from the core-shell

particles. As an example, nanocomposites were fabricated varying the amount of PS@TiO_2 core shell particles in a matrix of commercially available polystyrene. They exhibit very high dielectric constant and high percolation threshold. The origin of the high dielectric constant can be ascribed to the assembling of rutile nanoparticles in chestnut-like aggregates, where a number of core–shell rutile crystals share their faces and form capacitive microstructures. These aggregates, separated by a thin layer of polymer, allow the high increase of the filler amount up to 41% v/v avoiding the formation of the continuous network responsible for the sudden change of electrical characteristics. Despite the high content of inorganic fillers, the dissipation factor remains low, even approaching the lower frequencies. The low tanδ values in a large range of frequencies allow us to candidate the material for radio frequency (RF) applications where very low dissipation factor is desired to avoid signal losses.

RAFT was also used to prepare core-shell particles based on precipitated silica. Silica is currently used in the so-called green tires, since it reduces the rolling resistance and increases the wet traction. In order to make silica compatible with rubbers, typically polybutadiene and polyisoprene (PI), the surface of the particles is treated with silanes bearing sulphur groups, these groups participate at the vulcanization process. RAFT, instead, allows to grow directly on the silica surface polymer chains, so PI@SiO_2 core-shell particles were prepared and used to prepare rubber compounds.

Supporting information

Materials

1-Dodecanethiol (99.8 %), aliquot 336 (tricaprylylmethylammonium chloride), 1-mercaptopropionic acid (99 %), sodiun carbonate (Na_2CO_3, 99.9 %), magnesium sulfate ($MgSO_4$, 99.5 %), 3-(mercaptopropyl) trimethoxysilane (95 %), 3-(mercaptopropyl) triethoxysilane (95%), propyl mercaptan (99 %), carbon disulfide (CS_2, 99 %), and benzyl bromide (98%), lauryl peroxide (99 %), silica gel (60 Å) were purchased from Aldrich and used without further purification. Distilled and Milli-Q water (18.2 MΩ·cm at 25 °C) on site with the appropriate equipment were produced. Sodium methoxide (25 % wt. in methanol) freshly prepared. Triethylamine was dried over calcium hydride and distilled under nitrogen. PEO (Fluka Mn = 6000) was precipitated from diethyl ether two times.

Isoprene (Ip, 99 %), styrene (Sty, 99 %), N,N-Dimethylacetamide (DMA, 99 %), methymeta acrylate (MMA, 99 %), n-butyl acrylate (nB, 99 %), were obtained from Sigma-Aldrich and was stirred over calcium hydride for 2 days, distilled under reduced pressure and stored under nitrogen.

Dimethylacetamide (DMAc, 99.8 %), dimethylacrylate (DMA, 99%), methylene chloride (CH_2Cl_2, 99 %), acetone (99.9 %), chloroform (99 %), 2-propanol (99 %), hexane (99 %), diethyl ether (99 %), 1,4-dioxane anhydrous (99%), Tetrahydrofuran THF (inhibitor free, HPLC grade), methanol (HPLC grade,), chloroform-d (CD_3Cl, 99.8 %), deuterium oxide (D_2O, 99.8 %) were used as received. Azoisobutyronitrile (AIBN, Sigma-Aldrich) was recrystallized from methanol and stored in a freezer prior to use. Nitrogen (5.5) and argon (Ar, 5.5) were ultra-high purity grade gasses with zeolites 3 Å. All other materials were used as received from Sigma-Aldrich Company.

Dialysis tube, with MWCO of 3.5k and 15k Da, of series Spectra/Por 7 were used without purification.

Characterization

ATR-FTIR analysis was performed using a Perkin Elmer Spectrum 100 instrument scanning from 650 to 4000 cm^{-1} with a resolution of 4 cm^{-1} for 64 scans.

Transition temperatures were determined by differential scanning calorimetry (DSC) using a Mettler Toledo DSC 821 instrument with a heating and cooling rate of 20°C/min under nitrogen. Quantitative determination of the amount of organic molecules which functionalize the oxide (TiO_2 and SiO_2) was performed by Thermo Gravimetric Analysis (TGA) and DSC measurements on a Mettler Toledo TGA/DSC1 STARe System, at a constant gas flow (50 cm^3 min^{-1}). The thermal profile was the following: 40°C 5 min (N_2); 40–150°C 10°C min^{-1} (N_2); 150°C 5 min (N_2); 150–1000°C 10°C min^{-1} (air).

Molecular weights and molecular weight distributions were determined by Gel Permeation Chromatography (GPC) using a WATERS 1515 isocratic equipped with a HPLC Pump, WATERS 2414 refractive index detector, four Styragel columns (HR2, HR3, HR4 and HR5 in the effective molecular weight range of 500-20000, 500-30000, 50000-600000 and 50000-4000000 respectively) with THF as the eluent at a flow rate of 1.0 ml min^{-1}. The GPC system was calibrated with standard polystyrene from Sigma-Aldrich.

Elemental Analyses. C, H, were determined by combustion followed by chromatographic separation and thermal conductivity detection using a Carlo Erba 1108 elemental analyzer. Sulfur analyses were conducted using the Schoniger oxygen flask combustion method followed by the relevant titration.

NMR spectra were recorded on a Bruker AMX-500 instrument operating at 500.13 (^{1}H) and 125.77 (^{13}C) MHz. J-MOD. Coupling constants are given in Hz, using toluene-d, $CDCl_3$ and D_2O as the solvents.

The specific surface area (SSA), by the BET method, was measured by nitrogen physisorption with a Quantachrome Autosorb-1 apparatus. Powder samples were evacuated at 200°C for 16 h before the analysis.

Scanning electron microscopy (SEM) measurements were performed by a LEO 1450VP instrument. Transmission Electron Microscopy (TEM) analysis was carried out using a Jeol JEM-3010 instrument equipped with an Energy Dispersive Spectroscopy (EDS) system ISIS Series 300, manufactured by Oxford Instruments.

The impedance measurements were performed using a HP 4282A Precision LCR Meter in configuration Cp-G. The maximum tension was 1 V while the frequency varied between 20 Hz and 1 MHz. The final electrical characteristics of the material for each concentration of the filler were obtained averaging the data collected for the two different dimensions of the top contact.

Dynamic Light Scattering (DSC) experiments were performed at 25°C on a 90Plus Particle Size Analizer (Brookhaven Instruments Corporation) with scattering angles of 15° and 90°, equipped with a 35 mW solid state laser and a Brookhaven's TuboCorr correlator with 510 channels.

AFM imaging and force spectroscopy were carried out with a JPK NanoWizard (JPK Instruments, Berlin, Germany, with closed loop scanner) equipped with JPK controller and software, using the silicon cantilevers with a resonance frequency of 70 kHz and a nominal spring constant of 2 N m^{-1} (OMCL-AC240TS, Olympus, Tokyo, Japan).

The inner structure of particles was observed using a gallium Focused Ion Beam (FIB Dual Beam, FEI Helios). The particles as a liquid-drop state were located and dried on a Si wafer. The mounted particles on the Si wafer were deposited by Pt–Pd materials with the thickness of about 100 nm to prevent the

sample damage by Ga ion and then went to the FIB chamber, in which a big stair-step FIB trench was cut on one side of the particle until the inner structure was observed by scanning electron microscopy (SEM) which is mounted in FIB chamber with the tilting angle of 52° from a ion beam.

For the production of compounds was used a mixing chamber closed Thermo Haake Rheomix lab station with mixing chamber 250 ml and fill factor 0.7.

Acknowledgments

This work was supported by Pirelli Tyre and by Fondazione Cariplo at the University of Milano Bicocca.

I would like to thank Dr. Roberto Simonutti for his guidance, support and discussion during these last three years. I have to thank Dr. Raffaella Donetti, Dr. Luca Giannini and Dr. Marco Nahmias for willingness in Pirelli.

A dear thank goes to Michele Mauri, Gaetano Distefano, Tommaso Crisenza, Annalisa Colombo, Lucio Mauri, Luca De Trizio and all graduating students who have worked with me and for me in the group Posylife.

I am also very thankful to Prof. Dr. Hans-Jürgen Butt, Dr. Kaloian Koynov and Dr. Michael Kappl for hosting me at the Max Plank Institute for Polymer Research as part of the European Doctorate program. I definitely have to thank as well all the people in MPI-P in Mainz for the enjoyable period that I spent there.

A sincere thank you goes to all the people who have worked in my thesis: Dr. Luca Beverina, Dr. Gianfranco Vaccaro, Dr. Angelo Monguzzi and the group of Prof. Morazzoni, in particular Maurizio Crippa and Massimiliano D'Arienzo.

I would like also to acknowledge all the people I collaborated with, and who helped me in the realization of the work presented in this dissertation.

To last but not least, I thank my mom, my brother and my girlfriend Margherita for supporting me and drove to the outside of my work.

References

[1] R. T. A. Mayadunne, E. Rizzardo, J. Chiefari, Y. K. Chong, G. Moad, S. H. Thang, *Macromolecules*, **1999**, 32, 6977.

[2] J. S. Wang, K. Matyjaszewski, *J. Am. Chem. Soc.*, **1995**, 117, 5614.

[3] K. Matyjaszewski, J. Xia, *Chem. Rev.*, **2001**, 101, 2921.

[4] C. J. Hawker, *Angew. Chem. Int. Ed.*, **1995**, 34, 1456.

[5] C. J. Hawker, A. W. Bosman, E. Harth, *Chem. Rev.*, **2001**, 101, 3661.

[6] L. Barner, T. P. Davis, M. H. Stenzel, C. Barner-Kowollik, *Macromol. Rapid Commun.*, **2007**, 28, 539–559.

[7] F. S. Bates, G. H. Fredrickson, *Physics Today*, February **1999**.

[8] O. Prucker, J. Ruhe, *Macromolecules*, **1998**, *31*, 592-601.

[9] N. Tsubokawa, S. Machida, S. Yoshikawa, *J. Polym. Sci., Polym. Chem.*, **2002**, *36*, 3165-3172.

[10] C. Barner-Kowollik, T. P. Davis, M. Whittaker, *Journal of polymer Science*, **2003**, 41, 365-375.

[11] G. Moad, E. Rizzardo, S. H. Thang, *Polymer* **2008,** *49* (5), 1079-1131.

[12] S. N. Lewis, J.J. Miller, S. Winstein, *J Org Chem*, **1972**, 37 ,1478-1485.

[13] D. Barton, S. W. McCombie, *J. Chem. Soc.*, **1975**, 1, 1574-1585.

[14] G.F. Meijs, E. Rizzardo, D. Makromol, *Chem Rapid Commun*, **1988**, 9, 547-551.

[15] G.F. Meijs, E. Rizzardo, S.H. Thang, *Macromolecules*, **1988**, 21, 3122-3124.

[16] J. Chiefari, Y. K. Chong, F. Ercole, J. Krstina, J. Jeffery, P.T. Le Tam, A. Mayadunne, G. F. Meijs, C. L. Moad, G. Moad, E. Rizzardo, S. H. Thang, *Macromolecules*, **1998**, 31, 5559–5562.

[17] G. Moad, D.H. Solomon, *The chemistry of radical polymerization*, 2nd ed. Oxford, Elsevier, **2006**, 451-585.

[18] A. Ishii, J. Nakayama, *Top. Curr. Chem.*, **2005**, 251, 181-225.

[19] S. Z. Zard, *Angew. Chem.,* **1997**, 36, 672-685.

[20] G. Moad, *Aust J Chem*, **2006**, 59, 661-662.

[21] T. P. Le, G. Moad, E. Rizzardo, S. H. Thang, *Int. Patent Appl.*, **1998**, WO 9801478, USA.

[22] Web of science, Decembers, **2012**.

[23] E. Rizzardo, D. Harrison, R.L. Laslett, G.F. Meijs, T.C. Morton, S.H. Thang, *Prog. Pacific. Polym. Sci.*, **1991**, 2, 77-88.

[24] G. David, C. Boyer, J. Tonnar, B. Ameduri, P. Lacroix-Desmazes, B. Boutevin, *Chem. Rev.*, **2006,** 106, 3936-3962.

[25] S. Yamago, *J. Polym. Sci. Part. A Polym. Chem.*, **2006**, 44, 1-12.

[26] J. Krstina, C.L. Moad, G. Moad, E. Rizzardo, C.T. Berge, M. Fryd, *Macro. mol. Symp.*, **1996**, 111, 13-23.

[27] T. Otsu, M. Yoshida, *Macromol. Chem. Rapid. Commun*., **1982**, 3, 127-132.

[28] E. Rizzardo, G. Moad, S.H. Thang, *Handbook of RAFT polymerization*, **2007**, Weinheim, Germanym Wiley-VCH.

[29] S. Perrier, P. Takolpuckdee, *J. Polym. Sci. Part. A Polym. Chem.*, **2005**, 43, 5347-5393.

[30] A. Favier, M.T. Charreyre, *Macromol. Rapid. Commun.*, **2006**, 27, 653-692.

[31] C. Barner-Kowollik, T. P. Davis, J. P. A. Heuts, M. H. Stenzel, P. Vana, M. Whittaker, *J. Polym. Sci. Part. A Polym. Chem.*, **2003**, 41, 3653-75.

[32] M. J. Monteiro, *J. Polym. Sci. Part. A Polym. Chem.*, **2005**, 43, 3189-3204.

[33] A.B. Lowe, C.L. McCormick, *Prog. Polym. Sci.*, **2007**, 32, 283-351.

[34] G. Moad, Y.K. Chong, E. Rizzardo, A. Postma, S.H. Thang, *Polymer*, **2005**, 46, 8458-8468.

[35] L. Barner, T.P. Davis, M.H. Stenzel, C. Barner-Kowollik, *Macromol. Rapid. Commun.*, **2007**, 28, 539-559.

[36] M.H. Stenzel, C. Barner-Kowollik, T.P. Davis, *J. Polym. Sci. Part. A Polym. Chem.*, **2006**, 44, 2363-2375.

[37] B.Y.K. Chong, T.P.T. Le, G. Moad, E. Rizzardo, S.H. Thang, *Macromolecules*, **1999**, 32, 2071-2074.

[38] G. Moad, J. Chiefari, C.L. Moad, A. Postma, R.T.A. Mayadunne, E. Rizzardo, *Macromol. Symp.*, **2002**, 182, 65-80.

[39] Y.K. Chong, J. Krstina, T.P.T. Le, G. Moad, A. Postma, E. Rizzardo, *Macromolecules*, **2003,** 36, 2256-2272.

[40] M.L. Coote, E.I. Izgorodina, E.H. Krenske, M. Busch, C. Barner-Kowollik, *Macromol. Rapid. Commun.*, **2006**, 27, 1015-1122.

[41] K. Kubo, A. Goto, K. Sato, Y. Kwak, T. Fukuda, *Polymer*, **2005**, 46, 9762-9768.

[42] A. Alberti, M. Guerra, P. Hapiot, T. Lequeux, D. Macciantelli, S. Masson, *Phys. Chem. Chem. Phys.*, **2005**, 7, 250-257.

[43]M. L. Coote, D.J. Henry, *Macromolecules*, **2005**, 38, 5774-5779.

[44] A. Feldermann, M. L. Coote, M. H. Stenzel, T. P. Davis, C. Barner-Kowollik, *J. Am. Chem. Soc.*, **2004**, 126, 15915-15923.

[45] J. Chiefari, R. T. A. Mayadunne, C.L. Moad, G. Moad, E. Rizzardo, A. Postma, *Macromolecules*, **2003**, 36, 2273-2283.

[46] D. Charmot, P. Corpart, H. Adam, S.Z. Zard, T. Biadatti, G. Bouhadir, *Macromol. Symp.*, **2000**, 150, 23-32.

[47] M. H. Stenzel, *Macromol. Rapid. Commun.*, **2009**, 30, 1603–1624.

[48] M. A. White, A. Maliakal, N. J. Turro, J. Koberstein, *Macromol. Rapid. Commun.*, **2008**, 29, 1544–1548.

[49] Y. Tsujii, M. Ejaz, K. Sato, A. Goto, T. Fukuda, *Macromolecules*, **2001**, 34, 8872.

[50] C. Li, B. C. Benicewicz, *Macromolecules*, **2005**, 38, 5929.

[51] C. Li, J. Han, C. Y. Ryu, B. C. Benicewicz, *Macromolecules*, **2006**, 39, 3175.

[52] Y. Yang, Z. Yang, Q. Zhao, X. Cheng, S. C. Tjong, R. K. Y. Li, X. Wang, X. Xie, *J. Polym. Sci. Part A: Polym. Chem.*, **2009**, 47, 467.

[53] J. Raula, J. Shan, M. Nuopponen, A. Niskanen, H. Jiang,E. I. Kauppinen, H. Tenhu, *Langmuir*, **2003**, 19, 3499.

[54] H. Skaff, T. Emrick, *Angew. Chem.*, **2004**, 43, 5383.

[55] Y. Zhao, S. Perrier, *Macromolecules*, **2006**, 39, 8603.

[56] D. H. Nguyen, P. Vana, *Polym. Adv. Technol.*, **2006**, 17, 625.

[57] S. Perrier, P. Takolpuckdee, C. A. Mars, *Macromolecules*, **2005**, 38, 6770.

[58] J. Lai, T., D. Filla, R. Shea, *Macromolecules*, **2002**, 35, 6754.

[59] J. Skey, R. K. O'Reilly, *Chem. Commun.*, **2008**, 4183–4185.

[60] M. H. Stenzel, T. P. Davis., *J. Polym. Sci. Part. A Polym. Chem.*, **2002**, 40, 4498–4512.

[61] M. Hernandez-Guerrero, C. Barner-Kowollik, T.P. Davis, M.H. Stenzel, *Eur. Polym J.* **2005**, 41, 2264-2277.

[62] V. Mellon, D. Rinaldi, E. Bourgeat-Lami, F. D'Agosto, *Macromolecules*, **2005**, *38*, 1591-1598.

[63] R. Rotzoll, D. H. Nguyen, P. Vana, *Macromol. Symp*., **2009**, 275–276.

[64] Y. Zhao, S. Perrier, *Macromolecules***, 2007**, *40*, 9116-9124.

[65] Y. Zhao, S. Perrier, *Macromolecules*, **2006**, 39, 8603-8608.

[66] M. R. Wood, D. J. Duncalf, S. P. Rannard, S. Perrier, *Org. Lett.*, **2006**, 8(4), 553-556

[67] K. Wong, T. P. Davis, C. Barner-Kowollik, M. H. Stenzel, *Polymer*, **2007**, 48, 4950-4965.

[68] J. Skey, R. K. O'Reilly, *Chem. Commun.*, **2008,** 4183–4185.

[69] J. Rzayev, M. A. Hillmyer, *J. Am. Chem. Soc*., **2005**, 127, 13373-13379.

[70]E. B. Zhulina, O. V. Borisov, *Macromolecules*, **2012**, *45*, 4429-4440.

[71] H. Huang, B. Chung, J. Jung, H. W. Park, T. Chang, *Angew. Chem. Int. Ed.*, **2009**, *48*, 4594-4597.

[72] T. Azzam, A. Eisenberg, *Langmuir*, **2010**, *26*, 10513-10523.

[73] K. T. Kim, J. Cornelissen, R. J. M. Nolte, J. C. M. van Hest, *Adv. Mater*., **2009**, *21*, 2787.

[74] C. J. Lai, W. B. Russel, R. A. Register, *Macromolecules*, **2002**, *35*, 841-849.

[75] J. M. Virgili, A. Hexemer, J. A. Pople, N. P. Balsara, R. A. Segalman, *Macromolecules*, **2009**, *42*, 4604-4613.

[76] Y. Yamamoto, K. Yasugi, A. Harada, Y. Nagasaki, K. Kataoka, *J. Controlled Release*, **2002**, 82, 359-371.

[77] J. S. Hrkach, M. T. Peracchia, A. Domb, N. Lotan, R. Langer, *Biomaterials*, **1997**, 18, 27-30.

[78] C. R. Heald, S. Stolnik, K.S. Kujawinski, C. De Matteis, M.C. Garnett, L. Illum, S. S. Davis, S. C. Purkiss, R. J. Barlow, P. R. Gellert, *Langmuir*, **2002**, 18, 3669-3675.

[79] G. M. Wilmes, D. J. Arnold, K. S. Kawchak, J. Polym. Res. 2011, 18, 1787-1797; d) K. Vijayakrishna, D. Mecerreyes, Y. Gnanou, D. Taton, *Macromolecules*, **2009**, 42, 5167-5174.

[80] M. Wilhelm, C. L. Zhao, Y. C. Wang, R. L. Xu, M. A. Winnik, J. L. Mura, G. Riess, M. D. Croucher, *Macromolecules*, **1991**, *24*, 1033-1040.

[81] R. Rutkaite, L. Swanson, Y. Li, S. P. Armes, *Polymer*, **2008**, *49*, 1800-1811.

[82] S. C. Lee, Y. K. Chang, J. S. Yoon, C. H. Kim, I. C. Kwon, Y. H. Kim, S. Y. Jeong, *Macromolecules*, **1999**, 32, 1847-1852.

[83] K. Prochazka, D. Kiserow, C. Ramireddy, Z. Tuzar, P. Munk, S. E. Webber, *Macromolecules*, **1992**, *25*, 454-460.

[84] D. Kiserow, K. Prochazka, C. Ramireddy, Z. Tuzar, P. Munk, S. E. Webber, *Macromolecules*, **1992**, *25*, 461-469.

[85] D. Kiserow, J. Chan, C. Ramireddy, P. Munk, S. E. Webber, *Macromolecules*, **1992**, *25*, 5338-5344.

[86] Y. Teng, M. E. Morrison, P. Munk, S. E. Webber, K. Prochazka, Macromolecules, **1998**, 31, 3578-3587.

[87] P. Bosch, F. Catalina, T. Corrales, C. Peinado, *Chem. Eur. J.*, **2005**, *11*, 4314-4325.

[88] R. D. Priestley, C. J. Ellison, L. J. Broadbelt, J. M. Torkelson, *Science*, **2005**, *309*, 456-459.

[89] Y. Shiraishi, T. Inoue, T. Hirai, *Langmuir*, **2010**, *26*, 17505-17512.

[90] K. Y. Law, *Chem. Phys. Lett.*, **1980**, *75*, 545-549.

[91] K. Viajayakrsishna, D. Mecerreyes, Y. Gnanou, D. Taton, *Macromolecules*, **2009**, *42*, 5167-5174.

[92] J. L. Hutter, J. Bechhoefer, *Rev. Sci. Instrum.*, **1993**, *64*, 1868.

[93] A. Abbotto, R. Simonutti, N. Manfredi, A. Bianchi, *PCT Int. Appl.*, **2012,** WO2012153300 (A1), 15 November 2012.

[94] B. O'Regan, M. Gratzel, *Nature*, **1991**, 353, 737-740.

[95] M. Grätzel, *Acc. Chem. Res.*, **2009**, 42, 1788-1798

[96] A. J. Nozik, J. Miller, *Chem. Rev.*, **2010**, 110, 6443-6445.

[97] N. Armaroli, V. Balzani, *Angew. Chem. Int. Ed.*, **2007**, 46, 52-66.

[98] M. K. Nazeeruddin, F. De Angelis, S. Fantacci, A. Selloni, G. Viscardi, P. Liska, S. Ito, B. Takeru, M. Grätzel, *Journal of the American Chemical Society*, **2005**, 127, 16835-16847.

[99] S. Yanagida, Y. Yu and K. Manseki, *Acc. Chem. Res.*, **2009**, 42, 1827-1838.

[100] B. Li, L. Wang, B. Kang, P. Wang, Y. Qiu, *Sol. Energy Mater. Sol. Cells*, **2006**, 90, 549-573.

[101] H. J. Snaith, L. Schmidt-Mende, *Adv. Mater.*, **2007**, 19, 3187-3200.

[102] S. M. Zakeeruddin, M. Grätzel, *Adv. Funct. Mater.*, **2009**, 19, 2187-2202.

[103] N. Cai, S.-J. Moon, L. Cevey-Ha, T. Moehl, R. Humphry-Baker, P. Wang, S. M. Zakeeruddin, M. Grätzel, *Nano Lett.*, **2011**, 11, 1452-1456.

[104] J.E. Benedettia, A.D. Gonc¸ A.L.B. Formiga, M.-A. De Paolia, X. Li, J.R. Durrant, A.F. Nogueira, *Journal of Power Sources*, **2003**,119–121, 448–453.

[105] J. Nei de Freitas, A. F. Nogueira, M.-A. De Paoli, *Journal of Materials Chemistry*, **2009**, 19, 5279-5294.

[106] Y. Gao, H. Liu, *Journal of Applied Polymer Science*, **2007**, 106, 2718–2723.

[107] J. H. Wu, Z. Lan, J. M. Lin, M. L. Huang, S. C. Hao, T. Sato, S. Yin, *Adv. Mater.*, **2007**, 19, 4006-4011.

[108] J. Shi, S. Peng, J. Pei, Y. Liang, F. Cheng, J. Chen, *ACS Applied Materials & Interfaces*, **2009**, 1, 944-950.

[109] A. F. Nogueira, J. R. Durrant, M. A. De Paoli, *Adv. Mater.*, **2001**, 13, 826-830.

[110] A. Hillmyer, *J. Am. Chem. Soc.*, **2005**, 127, 13373-13379

[111] M. Sahnoun, M.-T. Charreyre, L. Veron, T. Delair, F. D'Agosto, *Journal of Polymer Science Part A: Polymer Chemistry*, **2005**, 43, 3551-3565.

[112] S. Ito, T. N. Murakami, P. Comte, P. Liska, C. Grätzel, M.K. Nazeeruddin, M. Grätzel, *Thin Solid Films*, **2008**, 516, 4613–4619.

[113] . Halme, P. Vahermaa, K. Miettunen, P. Lund, *Adv. Mater.*, **2010**, 22, E210-E234.

[114] Q. Wang, J.-E. Moser, M. Grätzel, *The Journal of Physical Chemistry B*, **2005**, 109, 14945-14953.

[115] F. Fabregat-Santiago, J. Bisquert, E. Palomares, L. Otero, D. Kuang, S. M. Zakeeruddin, M. Grätzel, *The Journal of Physical Chemistry C*, **2007**, 111, 6550-6560.

[116] F. Fabregat-Santiago, J. Bisquert, G. Garcia-Belmonte, G. Boschloo, A. Hagfeldt, *Sol. Energy Mater. Sol. Cells*, **2005**, 87, 117-131.

[117] A. Facchetti, M. H. Yoon and T. J. Marks, *Adv. Mater.*, **2005**, 17, 1705.

[118] Q. M. Zhang, H. F. Li, M. Poh, F. Xia, Z. Y. Cheng, H. S. Xu, *Nature*, **2002**, 419, 284.

[119] . Bai, Z. Y. Cheng, V. Bharti, H. S. Xu and Q. M. Zhang, *Appl. Phys. Lett.*, **2000**, 76, 3804.

[120] A. Burke. Electrochim, *Acta*, **2007**, 53, 1083.

[121] S. R. Forrest, *Nature*, **2004**, 428, 911.

[122] C. Dimitrakopoulos, P. Malenfant, *Adv. Mater.*, **2002**, 14, 99.

[123] S. Roberts, *Phys. Rev.*, **1949**, 76, 1215.

[124] S. Campbell, H. Kim, D. Gilmer, B. He, T. Ma, W. Gladfelter, *IBM J. Res. Dev.*, **1999**, 43, 383.

[125] A. K. Tagantsev, V. O. Sherman, K. F. Astafiev, J. Venkatesh, N. Setter, *J. Electroceram.*, **2003**, 11, 5.

[126] G. Goh, S. Donthu, P. Pallathadka, *Chem. Mater.*, **2004**, 16, 2857.

[127] W. Wunderlich, *Polymer Handbook*, ed. J. Brandrupp and E. Immergut, John Wiley & Sons, New York, 3rd edn, **1989**, p. V77.

[128] J. Rudd, *Polymer Handbook*, ed. J. Brandrupp and E. Immergut, John Wiley & Sons, New York, 3rd edn, **1989**, p. V81.

[129] B. Balasubramanian, K. L. Kraemer, N. A. Reding, R. Skomski, S. Ducharme and D. J. Sellmyer, *ACS Nano*, **2010**, 4(4), 1893.

[130] B. Chu, M. Lin, B. Neese and Q. Zhang, *J. Appl. Phys.*, **2009**, 105, 14103.

[131] J. Xu and C. P. Wong, *Composites Part A*, **2006**, 38, 13.

[132] P. Badheka, V. Magadala, N. G. Devaradju, B. I. Lee, E. S. Kee, *J. Appl. Polym. Sci.*, **2005**, 99, 2815.

[133] P. Barber, S. Balasubramanian, Y. Anguchamy, S. Gong, A. Wibowo, H. Gao, H. J. Ploehn and H. C. zur Loye, *Materials*, **2009**, 2, 1697.

[134] L. Jylha, A. Sihvola, *J. Phys. D: Appl. Phys.*, **2007**, 40, 4966.

[135] C. Pecharroman, J. S. Moya, *Adv. Mater.*, **2000**, 12, 294.

[136] Z. M. Dang, L.-Z. Fan, Y. Shen, C.-W. Nan, *Chem. Phys. Lett.*, **2003**, 369, 95

[137] L. Qi, B. I. Lee, S. Chen, W. D. Samuels, G. J. Exarhos, *Adv. Mater.*, **2005**, 17, 1777.

[138] Z. M. Dang, J. P. Wu, H. P. Xu, S. H. Yao, M. J. Jiang, *Appl. Phys. Lett.*, **2007**, 91, 072912.

[139] D. M. Grannan, J. C. Garland, D. T. Tanner, *Phys. Rev. Lett.*, **1981**, 46, 375.

[140] Z. M. Dang, Y. H. Lin, C. W. Nan, *Adv. Mater.*, **2003**, 15, 1625.

[141] G. Wang, *Appl. Mater. Interfaces*, **2010**, 2, 1290.

[142] H. Althues, J. Henle, S. Kaskel, *Chem. Soc. Rev*., **2007**, 36, 1454.

[143] B. Hojjati, R. Sui, P. A. Charpentier, *Polymer*, **2007**, 48, 5850-5858.

[144] F. P. Rotzinger, J. M. Kesselman-Truttmann, S. J. Hug, V. Shklover, M. Gratzel, *J. Phys. Chem.*, **2004**, 108, 5004-5017.

[145] A. Testino, I. R. Bellobono, V. Buscaglia, C. Canevali, M. D'Arienzo, S. Polizzi, R. Scotti, F. Morazzoni, *J. Am. Chem. Soc.* **2007**, 129, 3564.

[146] A. Maliakal, H. Katz, P. M. Cotts, S. Subramoney, P. Mirau, *J. Am. Chem. Soc.*, **2005**, 127, 14655.

[147] R. Scotti, M. D'Arienzo, F. Morazzoni, I. R. Bellobono, *Appl. Catal. B*, **2009**, 88, 323.

[148] J. Brandrup, E. H. Immergut, E. A. Grulke, *"Polymer Handbook",* 4th edition John Wiley, New York, NY, USA, **1999**.

[149] H. Althues, J. Henle, S. Kaskel, *Chem. Soc. Rev.* **2007**, 36, 1454.

[150] D. Bhadra, A. Biswas, S. Sarkar, B. K. Chaudhuri, K. F. Tseng, H. D. Yang. *J. Appl. Phys.*, **2010**, 107, 124115.

[151] C. Chiteme, D. S. Mclachlan, *Physica B.*, **2000**, 279, 69.

[152] C. W. Nan, Y. Shen, J. Ma, *Annu. Rev. Mater. Res.*, **2010**, 40, 131.

[153] Z. M. Dang, J. P. Wu, H. P. Xu, S. H. Yao and M. J. Jiang, *Appl. Phys. Lett.*, **2007**, 91, 072912.

[154] L. Jylha, A. Sihvola, *J. Phys. D: Appl. Phys.* **2007**, 40, 4966.

[155] J. Mark, T. Erman, B. Eirich, Science and Technology of Rubber, Editors. **1994**, Academic Press: San Diego.

[156]A. Brinke, Silica Reinforced Tyre Rubbers: Mechanistic Aspects of the Role of Coupling Agents. **2002**, University of Twente: Enschede.

[157] M. Wischhusen, , Balancing Rolling Resistance with Other Performance Characteristics. Tyre Review, **2010**.

[158] D.W Schaefer, *J. Appl. Crys.*, **2000**, 33, 587-591.

[159] National Research Council of the National Academies of Science, Tires and Passenger Vehicle FuelEconomy, Editor, **2006**, Washington, D.C.

[160] W. Hofmann, "Rubber Technology Handbook", **1996**, Hanser/Gardner, Munich.

[161] Y. Zhao, S. Perrier, *Macromolecules*, **2007,** *40*, 9116-9124.